Interdiffusion within model TiN/Cu and TiTaN/Cu systems synthesized by combinatorial thin film deposition

Dipl.-Ing. Marlene Mühlbacher

Being a thesis in partial fulfilment of the requirements for the degree of a
Doktor der montanistischen Wissenschaften (Dr. mont.)
at the Montanuniversität Leoben

Chair of Functional Materials and Materials Systems
Department of Physical Metallurgy and Materials Testing
Montanuniversität Leoben, A-8700 Leoben, Austria
Leoben, 2015

Interdiffusion within model TiN/Cu and TiTaN/Cu systems synthesized by combinatorial thin film deposition

Marlene Mühlbacher, 2015

Affidavit

I declare in lieu of oath that I wrote this thesis and performed the associated research myself, using only literature cited in this volume.

Leoben, November 2015

ACKNOWLEDGMENTS

I am deeply grateful to my supervisors Christian Mitterer and Lars Hultman for supporting me through highs and lows and for giving me the chance to work in two wonderful groups where I could not only expand my knowledge about thin film physics but also got the opportunity to broaden my horizon by interacting with amazing people from all over the world.

An equally big thank you is due to my co-supervisors Nina Schalk and Jun Lu, who always took the time to listen, discuss, motivate and show the path forward.

I would like to thank all the technical and administrative staff for paving the way through challenging technical and bureaucratic matters, most of all Reinhilde Stopar, the good soul of our department, Bernhard Sartory, the “FIB wizard”, and Thomas Lingefelt, the “TEM whisperer”.

I am also grateful to all of my collaborators and co-authors of publications originated from this thesis, in particular Francisca Mendez-Martin, Jozef Keckes, Anton Bochkarev, Maxim Popov, Peter Puschnig, Jürgen Spitaler, Livia Chitu, Juraj Todt, and Jens Jensen. It was a pleasure to do research with you!

Furthermore I would like to express my sincere gratitude to Grzegorz Greczynski, Ivan Petrov, and Joe Greene for truly inspiring discussions and a fruitful collaboration.

Many thanks go to my colleagues in Leoben and Linköping for the pleasant and stimulating work environment.

My graduate study years would only have been half as splendid without the constant support of my friends: July, Tamara, Manu, Sabrina, Angie, Suse, Anke, Joe, Agne – you were great!

Last but not least, I would like to thank my parents for everything.

ABSTRACT

Continued device miniaturization in microelectronics calls for a fundamental understanding of diffusion processes and damage mechanisms in the Cu metallization/TiN barrier layer system. Thus, the starting point of the present study is a combined experimental and theoretical examination of lattice diffusion in ideal single-crystal TiN/Cu stacks grown on MgO(001) by unbalanced DC magnetron sputter deposition. After a 12 h annealing treatment at 1000 °C, a uniform Cu diffusion layer of 7-12 nm is observed by scanning transmission electron microscopy and atom probe tomography (APT). Density-functional theory calculations predict a stoichiometry-dependent atomic diffusion mechanism of Cu in bulk TiN, with Cu diffusing on the N sublattice for the experimental N/Ti ratio of 0.92.

These findings are extended to a comparison of grain boundary diffusion of Cu in dense polycrystalline TiN sputter-deposited on Si at 700 °C and underdense polycrystalline TiN grown on Si without external substrate heating. While the Cu diffusion path along dense TiN grain boundaries can be restricted to approximately 30 nm after a 1 h annealing treatment at 900 °C as visualized by 3D APT reconstructions, it already exceeds 500 nm after annealing at 700 °C in the underdense low-temperature TiN barrier. In this case, the formation of the Cu_3Si phase, which characteristically grows along the close-packed <101> directions in Si, is identified as the main damage mechanism leading to complete barrier failure.

To meet the low-temperature processing needs of semiconductor industry and at the same time exploit the improved performance of dense polycrystalline barrier layers, deposition of $Ti_{1-x}Ta_xN$ barriers on Si is demonstrated by a reactive hybrid high-power impulse/DC magnetron sputtering process, where barrier densification is achieved by pulsed irradiation of the growth surface with only a few at.% of energetic Ta ions without external substrate heating. These barrier layers delay the onset of Cu grain boundary diffusion to temperatures above 800 °C (1 h annealing time) and are therefore capable of competing with TiN barriers deposited at 700 °C.

PREFACE

This thesis summarizes my research work conducted in equal parts at the Chair of Functional Materials and Materials Systems at Montanuniversität Leoben (Austria) and at the Department of Physics, Chemistry and Biology (IFM) within the Thin Film Physics Division at Linköping University (Sweden) from September 2012 to November 2015.

The present study investigates interdiffusion within model TiN/Cu and TiTaN/Cu systems synthesized by combinatorial thin film deposition approaches. Characterization is mainly carried out by two high-resolution state-of-the-art methods, transmission electron microscopy and atom probe tomography, to reveal the diffusion mechanisms down to the atomic scale. Experimental findings are complemented by numerical simulations to provide a comprehensive description of diffusion phenomena in materials relevant for microelectronics. The main results of this study also have been or will be published as scientific articles as listed at the end of this thesis.

The foundations of this work were laid in my Licentiate thesis entitled “High-resolution characterization of TiN diffusion barrier layers” [1], available online via Linköping University Electronic Press (ISBN: 978-91-7685-994-0, DOI: 10.3384/lic.diva-120394).

Financial support by the Austrian Federal Government (in particular from Bundesministerium für Verkehr, Innovation und Technologie and Bundesministerium für Wirtschaft, Familie und Jugend) represented by Österreichische Forschungsförderungsgesellschaft mbH and the Styrian and the Tyrolean Provincial Government, represented by Steirische Wirtschaftsförderungsgesellschaft mbH and Standortagentur Tirol, within the framework of the COMET Funding Programme is gratefully acknowledged.

The Ultra Electron Microscopy Laboratory at Linköping University operated by the Thin Film Physics Division is supported by the Swedish Knut and Alice Wallenberg Foundation.

CONTENTS

CHAPTER 1

OVERVIEW OF THE SCIENTIFIC FIELD

1.1 INTRODUCTION

In the age of instant communication no other technological development has impacted everyday life like the advances in microelectronics. I remember vividly that when I was a kid, I used to carry around a portable CD-player with me that took up a large part of my rucksack. Nowadays, this CD-player has long been discarded and replaced by a multipurpose device – a "smart" phone – that fits into my back pocket and not only connects me to the rest of the civilized world, but also stores thousands of songs on its memory chip. This was made possible by the continued device miniaturization strived for amongst manufacturers of integrated circuits (ICs), while at the same time IC reliability and functionality have been further optimized. Diffusion barriers, which are employed to separate the Cu interconnects from the adjacent dielectrics and semiconductors in ICs [2], are an integral part of this development. They are often key to device performance and lifetime [3], as they prohibit the migration of atoms from the Cu metallization to the surrounding dielectrics or the Si substrate and vice versa, so that no chemical reactions potentially impairing the device functionality can occur [2]. Thus, the aim of this study is to investigate and characterize diffusion phenomena, atomic diffusion mechanisms, and manifestations of interdiffusion damage in technologically relevant thin film systems as well as to adopt suitable novel thin film deposition approaches to synthesize improved diffusion barrier layers.

TiN-based films have been chosen to serve as model diffusion barrier materials due to their favorable structural, thermal and electronic properties and their high technological importance. TiN is a state-of-the-art diffusion barrier material [4,5]. However, there is always room for improvement, especially when it comes to transferring findings of fundamental research to actual microelectronics applications. The latest (2013) edition of the biannually published *International Technology Roadmap for Semiconductors* [4] projects that the diffusion barrier thickness must be scaled down below 2 nm by 2015 and below 1 nm by 2021. A promising strategy to fulfill this demand might be to tune the microstructure of the established TiN barriers by optimizing deposition parameters to increase their efficiency [5,6]. Another approach is to utilize a completely novel thin film deposition method meeting semiconductor processing requirements to deposit ternary TiTaN barriers with a fully dense microstructure. Concurrently, metrology tools must be developed to characterize the structure and composition of these complex layered material systems, preferably in three dimensions. Thereby, the challenge lies in the need to gather local information at nanoscale dimensions on the one hand and to do this over a relatively large area like a Si wafer on the other hand. A possibility to overcome this problem is to employ numerical modelling and simulation. Still, it remains essential to determine nanoscale material properties as input parameters for metrology models [4]. Many thin film characterization methods can provide valuable information on interdiffusion processes in layered systems, but often the achievable resolution is not as high as desirable. Therefore, this study focuses on two high-resolution techniques: Transmission electron microscopy (TEM) is a well-established, versatile characterization method that provides structural, chemical and electronic information with excellent spatial resolution. It even offers the possibility to acquire lattice resolved images that can be related to the film and interface structure. Reciprocal space information can be obtained at the same spatial location and gives further insights into crystallographic orientation relationships at interfaces. Furthermore, elemental mapping and Z (atomic number)-contrast imaging allow for the visualization of interdiffusion in the investigated thin film systems [7]. Recently another technique, atom probe tomography (APT), has become popular among materials scientists as a tool providing true three-dimensional characterization at the nanoscale. APT is a complementary method to TEM, as it performs three-dimensional compositional imaging and analysis of materials with high sensitivity. Thus, together the two techniques can give information about the morphology, atomic structure, chemical composition and interdiffusion in thin film systems with sub-nanometer resolution.

In the present study, various thin film characterization methods with a particular emphasis on TEM and APT are combined in order to present a sophisticated and comprehensive analysis approach for the nanoscale investigation of interfaces and interdiffusion processes in model TiN/Cu and TiTaN/Cu systems. Chapter 3 focuses on the structural and elemental characterization of the single-crystal TiN/Cu interface and correlates experimental observations of Cu diffusion in single-crystal TiN with results of first-principles studies [8]. Chapter 4 compares the diffusion of Cu in single- and polycrystalline TiN barrier layers. This is taken as a starting point to examine possible atomic Cu diffusion mechanisms in the single-crystal TiN barrier by density-functional theory (DFT) calculations [9]. Chapter 5 presents the large-scale failure of a model TiN diffusion barrier by the formation of Cu_3Si. It shows how the local diffusion of Cu through defects and grain boundaries in the TiN layer leads to the formation of the Cu_3Si phase at the barrier/substrate interface, while the outward diffusion of Si atoms from the substrate through the TiN bulk towards the Cu top layer eventually also results in the formation of a discontinuous Cu_3Si surface layer. Chapter 6 concludes the study by demonstrating the applicability of a hybrid high-power impulse/DC magnetron sputter process to deposit dense TiTaN barriers without external substrate heating, thus meeting the low-temperature processing needs of semiconductor industry.

1.2 DIFFUSION IN SOLIDS

1.2.1 The Diffusion Equations

Diffusion is a process resulting from random motion of particles along a chemical potential gradient [10]. For practical purposes, the chemical potential gradient is often substituted by a concentration gradient for easier experimental accessibility. Under steady-state conditions, the net material flux J along a direction x is proportional and opposed to the concentration gradient $\partial C/\partial x$ via a proportionality constant called the diffusion coefficient D, as postulated by Fick [11]:

$$J = -D\frac{\partial C}{\partial x}\,. \tag{1}$$

This is *Fick's first law* [11,12]. A continuance of this equation also accounts for the time-dependency (time t) of the concentration gradient, and is referred to as *Fick's second law* [11,12].

$$\frac{\partial C(x,t)}{\partial t} = D\frac{\partial^2 C}{\partial x^2}\,. \tag{2}$$

In solids, diffusion is the exclusive mass transport mechanism [13]. As presented in more detail in my Licentiate thesis [1], the diffusion coefficient D follows an Arrhenius-type temperature dependence:

$$D = D_0 \exp\left(-\frac{Q}{kT}\right). \tag{3}$$

Here, Q is the diffusion activation energy, k the Boltzman constant, and T the temperature. The pre-exponential or frequency factor D_0 can be considered a material constant and represents the diffusion coefficient at infinite temperature [10,14]. This model describes lattice diffusion, but is also applicable to grain boundary or interface diffusion in general, if the activation energy is modified accordingly [12,14].

The thin film solution of Fick's second law assumes non-steady-state diffusion in one dimension. With the diffusing species deposited in the form of a thin film on a bulk sample surface (*instantaneous planar source* condition), the solution to the diffusion equation is then of a Gaussian form [10] and given by

$$C(x,t) = \frac{M}{\sqrt{\pi D t}} \exp\left(-\frac{x^2}{4Dt}\right), \tag{4}$$

with M as the number of diffusing particles per unit area. The diffusion length $\bar{x}$ at which the argument in the exponential function equals -1 is known as *characteristic diffusion length* and is often encountered in diffusion problems [10]:

$$\bar{x} = 2\sqrt{Dt}. \tag{5}$$

Many diffusion experiments are designed so that the characteristic diffusion length is measured after the sample is heated to a specific temperature for a given time in order to obtain $D(T)$ from equation (5). This information can then be used to find D_0 and Q by linear regression from an Arrhenius plot of equation (3).

1.2.2 Diffusion Mechanisms in Solids

The crystal lattice restricts atomic movement in solids. Depending on the prevalent atomic jump process involved in the migration of the atoms, several lattice diffusion mechanisms have been defined as illustrated in Fig. 1 [10]. Atoms of any type can move through the crystal by a series of exchanges with vacancies (Fig. 1 (a)), which are present at all temperatures. Small solute atoms like O, N, C, and H can also diffuse by jumping along neighboring interstitial sites (Fig. 1 (b)). While the vacancy and interstitial diffusion mechanisms are common, the collective mechanism (Fig. 1 (c)), where several atoms move simultaneously to exchange places, is energetically unfavorable in most solids and therefore seldom encountered [10].

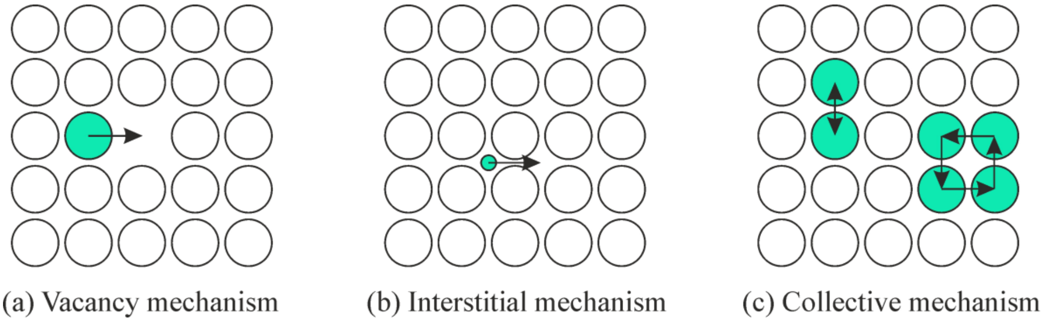

(a) Vacancy mechanism (b) Interstitial mechanism (c) Collective mechanism

Figure 1: Schematic illustration of lattice diffusion via the (a) vacancy, (b) interstitial, and (c) collective mechanism [1].

Aside from contemplations of the perfect lattice, also lattice defects have to be considered as diffusion paths. In particular, grain boundaries provide preferred pathways for diffusing particles, since the atomic packing in these transition regions between two crystals with different crystallographic orientations is less dense than in the perfect crystal [6,15]. The Arrhenius relation given in equation (3) also holds for the polycrystalline case, if all lattice diffusion terms (D, D_0, and Q) are exchanged by grain boundary diffusion terms (D_{gb}, D_{0gb}, and Q_{gb}, respectively). Due to the lower activation energy involved in grain boundary diffusion, D_{gb} is generally several orders of magnitude larger than D [10]. Depending on the interplay between lattice and grain boundary diffusion, different kinetic diffusion regimes can be distinguished in polycrystals, ranging from almost planar diffusion fronts to diffusion occurring exclusively along grain boundaries [16].

1.3 THIN FILM SYNTHESIS

1.3.1 Sputter Deposition

A. Magnetron sputter deposition

Magnetron sputtering belongs to the group of physical vapor deposition (PVD) techniques. It is based on the physical evaporation of atoms by momentum transfer from impinging energetic particles. The process itself can be divided into three steps: *(i)* the transition of the material to be deposited from the condensed phase to the vapor phase, *(ii)* the transport of the vapor from the source to the substrate, and *(iii)* condensation of the vapor at the substrate, followed by film nucleation and growth [17,18].

In a typical sputter deposition process, the sputtering system is evacuated to a base pressure in the high or ultra-high vacuum range. Subsequently, the working gas, generally an inert gas like Ar, is introduced into the vacuum chamber. A negative DC voltage is applied to the material to be sputtered, which is mounted in the deposition chamber in the form of a so-called target and thus serves as the cathode. The grounded or biased substrate holder becomes the anode. Stray electrons present in the working gas are accelerated towards the anode and collide with neutral gas atoms, thereby splitting them into positively charged ions and electrons in an impact ionization process. Additionally, positive ions impinge on the target and eject secondary electrons, resulting in a snowball effect, and a self-sustaining gas glow discharge is established. This partially ionized, quasi-neutral gas is known as plasma [14].

Material transfer from the target to the substrate takes place because the bombardment with energetic particles also leads to the ejection of target atoms, if the energy transferred in the collision is sufficient to overcome the atoms' surface binding energy. Sputtering of target atoms occurs due to a single knock-on event, or as a result of a collision cascade [14,19]. Aside from the transferred energy, the sputter yield (the ratio of incident ions to sputtered atoms) also depends on the mass of the bombarding ion and the target material. In most practical sputtering processes the sputter yield is 0.1-10 [14].

A viable strategy of increasing the deposition rate in a sputtering process is trapping of secondary electrons near the target by a magnetic field. A suitable magnet arrangement for a planar magnetron is shown in Fig. 2. The electrons restricted to a closed path above the target create a high-density plasma and a pronounced erosion zone (*"racetrack"*) becomes evident on the used target. In most technical applications a so-called unbalanced magnetron configuration is used. The magnetic field is weakened selectively to allow some secondary

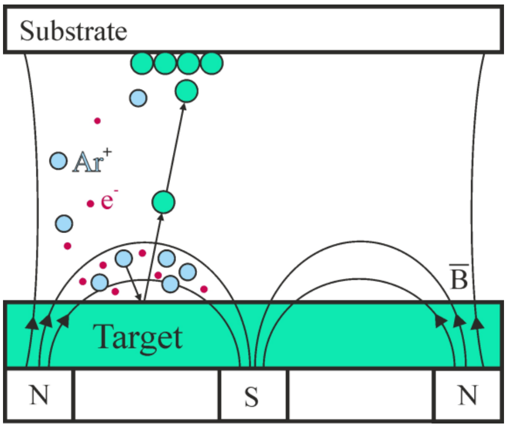

Figure 2: Illustration of the sputtering process occurring in an unbalanced magnetron configuration [1].

electrons to escape from the target region, so as not to completely confine the plasma there. Thus, some ions are still available to influence film growth at the substrate. Magnetic field lines appropriate to this setup are also plotted in Fig. 2 [14,20,21].

For the special case of compound films, deposition can either be achieved by sputtering from compound targets or sputtering in the presence of a reactive gas [22]. Additional effects such as compound formation on the target surface ("*poisoning*") have to be taken into account in reactive processes. In practice, a decreasing sputter yield is often observed once the compound has formed on the metal target, which in turn leads to a drop in deposition rate [23]. The TiN and TiTaN films discussed in the present thesis are deposited in a mixed Ar/N_2 discharge by sputtering pure Ti and Ta targets. The reactive gas partial pressure is chosen to facilitate the growth of near-stoichiometric films while maintaining reasonable deposition rates around 10-35 nm min^{-1} for the nitride coatings.

B. High-power impulse magnetron sputtering

The degree of ionization of the sputtered species in conventional magnetron sputtering is typically less than 1% [24]. In 1999, Kouznetsov *et al.* reported sputtering of Cu with a pulsed power supply, achieving peak power densities of 2800 W cm^{-2} at the planar Cu target and an ionization of 70% of the sputtered material [25]. This new technique employing high power pulses of several kW cm^{-2} with low duty cycles (< 10%) and frequencies (< 10 kHz) at the targets was termed high-power impulse magnetron sputtering (HIPIMS) [24]. The high-density plasmas generated accordingly are characterized by a high degree of ionization and an off-normal particle flux of the sputtered species with regard to the target surface. This results in the growth of dense and smooth coatings with improved thickness uniformity, also if deposited on substrates with complex shapes such as via-structures common in Cu metallization [19,24–26].

Greczynski *et al.* recently demonstrated the synthesis of dense TiTaN coatings by a hybrid high-power impulse/DC magnetron sputter process without external substrate heating [27]. In this process, the Ti target is operated in DC mode to provide a constant flux of metal atoms, thereby sustaining a high deposition rate. High power pulses are applied to the Ta target synchronously with a pulsed substrate bias voltage to achieve film densification at low substrate temperatures by heavy ion irradiation. The applicability of this deposition approach for the growth of TiTaN diffusion barriers is demonstrated in chapter 6.

1.3.2 Thin Film Nucleation and Growth

A. Nucleation and early stages of growth

Once sputtered atoms are adsorbed at the substrate, they proceed to diffuse along the surface until they reach an energetically favorable position or are desorbed again. This atomic movement is controlled by the substrate temperature and kinetic energy of the adsorbed atoms (ad-atoms). Nucleation occurs preferably at lattice defects and atomic steps. Fig. 3 (a) depicts the processes occurring in the early stages of nucleation. A stable nucleus exceeds a critical size, which is determined by the trade-off between volume free energy and surface energy. It grows by the incorporation of further ad-atoms and subcritical clusters. Thus, distinct islands are formed, which eventually coalesce with their neighbors. The sustained influx of atoms leads to the filling of channels and voids in the coalesced network until the film is continuous [14,28]. These processes account for the first few hundred Ångströms of film thickness [14].

Subsequent film growth can be classified into three different modes, schematically illustrated in Fig. 3 (b).

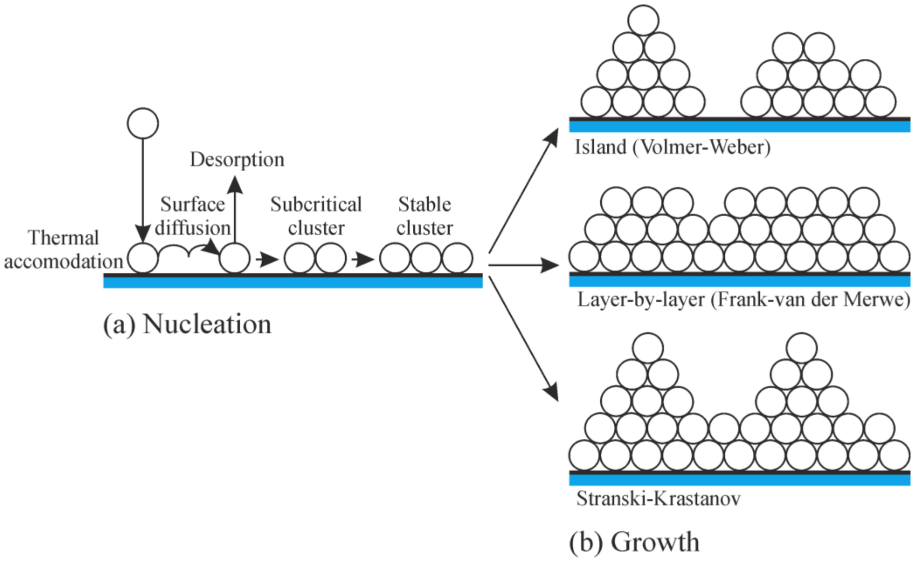

Figure 3: Schematic representation of (a) the steps leading to nucleation and (b) the three film growth modes [1].

- *Island (Volmer–Weber) growth* is a three-dimensional growth mode, which is active when the net surface free energy associated with cluster formation is positive. Deposited atoms are more strongly bound to each other than to the substrate [14,28].
- *Layer-by-layer (Frank-van der Merwe) growth* is a two-dimensional growth mode. Stable nuclei grow in a planar fashion. The layer growth mode is sustained provided there is a continuous decrease in bonding energy between the layers from the first monolayer to the bulk-crystal value [14,28].
- *Stranski-Krastanov growth* develops when layer growth becomes unfavorable after the formation of one or more monolayers and island growth proceeds. This is a fairly common growth mode and often occurs as a strain relaxation mechanism (strain-induced roughening) [14,28].

Within the present study, examples for all of these growth modes can be found. Single-crystal growth of TiN on MgO takes place in a layer-by-layer mode [29]. X-ray reflectivity investigations reporting a TiN surface roughness in the range of the MgO substrate roughness in chapter 3 are a good argument in support of this growth fashion. Literature commenting on the growth mode of Cu on single-crystal TiN is scarce, but HRTEM examinations suggest a form of Stranski-Krastanov growth, which is also plausible as a possible strain relaxation mechanism. An example for the three-dimensional island growth mode is polycrystalline TiN and TiTaN on Si [30].

B. Epitaxy and single-crystal thin films

Epitaxy generally refers to a film/substrate system with a defined crystallographic orientation relationship. It is characterized by the lattice mismatch $\bar{f}$ between the film and substrate material [14,31].

$$\bar{f} = \frac{a_0(s) - a_0(f)}{a_0(f)} \times 100\% , \tag{6}$$

where $a_0(s)$ and $a_0(f)$ are the unstrained lattice parameters of the substrate and film, respectively. As a rule of thumb, epitaxial growth requires a lattice mismatch of less than 15% [31]. Epitaxial growth can be divided into homoepitaxy, where film and substrate are of the same material, and heteroepitaxy, where film and substrate are composed of different materials [31].

Single-crystal TiN layers investigated within the present thesis have been grown epitaxially on MgO(001) substrates. Both materials crystallize in the B1 face centered cubic (fcc) rock salt structure and have a lattice mismatch of only -0.7% [32,33]. In contrast, the lattice mismatch between TiN and fcc Cu amounts to -17% [33,34], thus slightly exceeding the 15% rule. Still, epitaxial growth of Cu on TiN is a reasonable assumption, as it has also been reported for Cu films deposited on MgO, where the lattice mismatch is comparable [35,36]. Pole figure measurements and TEM investigations presented in chapter 3 corroborate the cube-on-cube epitaxial relationship found for the TiN/Cu bilayers with the substrate, i.e. {001}<010>TiN/Cu || {001}<010>MgO [8].

C. Polycrystalline thin films

Kinetic limitations control film growth in PVD, which takes place far from thermodynamic equilibrium. Thus, grain shape and orientation in polycrystalline films often develop in a competitive fashion, with surface and bulk diffusion as the determining mechanisms [28,37]. Structure zone models (SZMs) provide a guideline for microstructural design of polycrystalline PVD coatings by systematically categorizing the structural evolution as a function of deposition parameters.

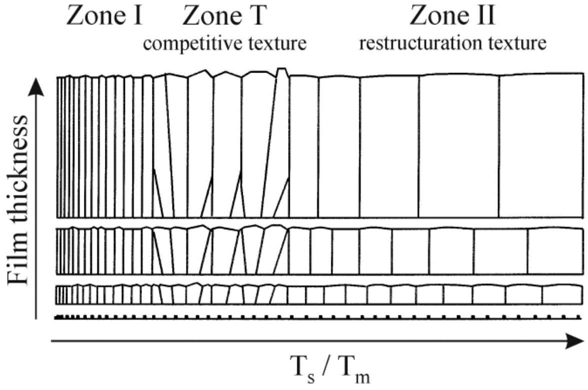

Figure 4: Basic structure zone model for elemental films adapted from Barna and Adamik [37].

The basic SZM for elemental films as depicted in Fig. 4 illustrates film evolution with increasing temperature and film thickness. The parameter plotted on the *x*-axis is the ratio of the substrate temperature T_s to the melting temperature of the film T_m (both in Kelvin), known as the homologous temperature. Depending on this temperature, the SZM comprises three regions [14,28,37]:

- *Zone I* ($0 < T_s/T_m < 0.2$): Due to the low temperatures, thermally activated ad-atom diffusion is negligible. Films grow with an underdense, randomly oriented fiber structure featuring extensive inter- and intracolumnar porosity.
- *Zone T* ($0.2 < T_s/T_m < 0.4$): In this transition zone growth regime, surface diffusion of ad-atoms is substantial. Competitive growth results in a typical film morphology with V-shaped grains close to the nucleation layer morphing into columnar grains at higher film thicknesses.
- *Zone II* ($0.4 < T_s/T_m$): In this growth regime, bulk diffusion and grain boundary migration become active. The minimization of interface and surface energy is the driving force for orientation selection during grain coalescence and coarsening. Lateral dimensions of the columns increase with increasing homologous temperature.

Several other, more specific SZMs describing the influence of, e.g., oxygen contaminations during film growth, working gas pressure, or ion irradiation, are available in literature [37–39].

In general, it can be concluded that deposition at high substrate temperatures and low deposition rates promotes the growth of large grains or even single-crystals, while low substrate temperatures and high deposition rates favor the formation of polycrystalline films with smaller grains [14].

D. Effects of substrate biasing

Providing energy to the film forming species in the form of moderate ion bombardment promotes the ad-atom surface diffusion (compare chapter 1.3.1.B). Properties that benefit from this enhanced atomic mobility during film growth include, but are not limited to, film density, grain morphology, and surface smoothness [14,28,40]. Ideally, the ion flux reaching the substrate should be high, while the ion energy should be low (< 10-20 eV) to avoid damaging the film [28]. A simple approach is biasing of the substrate to vary the ratio of incident ions to neutrals.

TiN barrier layers discussed in chapters 3 and 4 are deposited at an asymmetrically pulsed bipolar DC substrate bias of -100 V. The DC voltage is pulsed at a frequency of 250 kHz with a positive pulse duration of 496 ns at a preset amplitude of +37 V [41]. Similarly, for the deposition of the TiTaN barrier layers in chapter 6, a negative pulsed bias voltage of 60 V is applied at the substrate synchronously with the high power pulses at the Ta target to achieve film densification at low substrate temperatures by heavy ion irradiation.

1.4 TITANIUM NITRIDE THIN FILMS

1.4.1 Composition, Structure and Mechanical Properties of TiN

TiN is a refractory interstitial transition metal nitride, with a melting temperature of 2949 °C for the stoichiometric compound. It crystallizes in the fcc B1 structure [42]. Since the binary TiN phase is stable over a wide composition range [43], the intrinsic defect density can become very high. Vacancies and interstitials are found both on the Ti- and the N sublattices and strongly influence properties of TiN films [44]. Sundgren *et al.* conducted one of the earliest comprehensive investigations of sputtered TiN coatings [44–47]. They identified the ratio of reactive to sputtering gas as well as the ion current density at the substrate and the voltage applied to the target as the most influential process parameters determining the TiN film composition [46]. At a Ti/N ratio of one, polycrystalline TiN films exhibit the full bulk density of 5.39 g cm^{-1} and have a minimum electrical resistivity of 25 µΩ cm [45]. The lattice parameter reaches its maximum value of 4.242 Å at the same composition, and decreases for both over- and substoichiometric films [44,45].

The microstructure of sputtered TiN can be tuned by using different substrate materials as templates. Single-crystal TiN can be grown epitaxially on MgO substrates as shown in Fig. 5 (a). In comparison, growth of polycrystalline TiN on Si substrates or the native oxide typically proceeds from a fine grained nucleation layer close to the interface to a more or less dense array of cone-shaped columnar grains, characteristic of zone T in the SZM, as can be seen in Fig. 5 (b). Film microstructure plays a key role in determining the mechanical performance of TiN coatings. Patsalas *et al.* [48] report that with increasing bias potential and deposition temperature the film hardness and elastic modulus of polycrystalline TiN increase from 17 to 24 GPa and 210 to 320 GPa, respectively. This can be attributed to the enhanced film density and reduction of voids in films grown under ion irradiation as discussed in chapter 1.3.2.D. In case of single-crystal TiN, hardness and elastic modulus depend on the film orientation, where TiN(111) performs best, with a hardness of 21 GPa and Young’s modulus of 450 GPa [49].

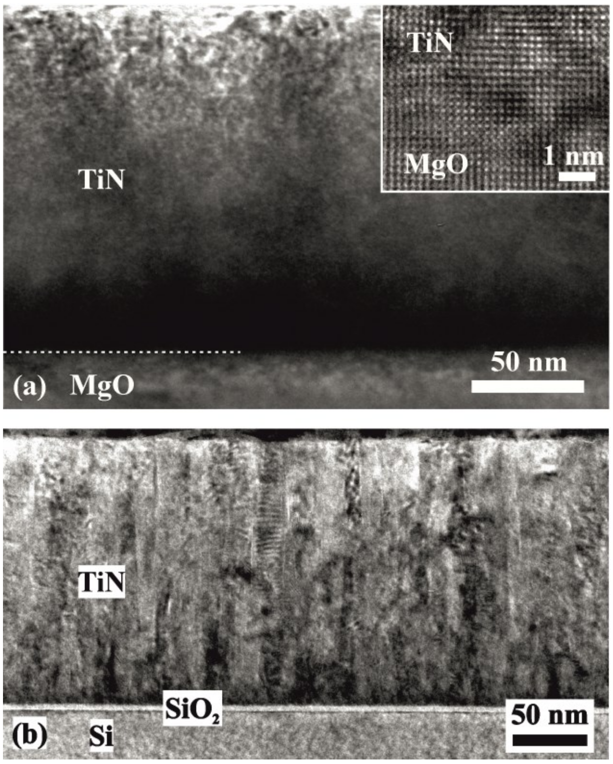

Figure 5: Cross-sectional TEM images of sputter deposited (a) featureless single-crystal TiN grown on MgO and (b) polycrystalline TiN grown on thermally oxidized Si. The inset in (a) shows a lattice resolved micrograph recorded directly at the TiN/MgO interface along the [100] zone axis, though the exact interfacial planes cannot be determined due to the close lattice match. The polycrystalline TiN depicted in (b) exhibits a typical columnar zone T microstructure [1].

1.4.2 Electronic and Optical Properties of TiN

Eight of the nine valence electrons in TiN fill bonding states, with the additional electron occupying a non-bonding state, thus making the compound metallic [50]. In single-crystal TiN the electrical resistivity at room temperature is 18 μΩ cm [51]. It increases with increasing temperature, a typical metallic behavior. Resistivities of polycrystalline films are higher, within the range of 25–1000 μΩ cm [45,52–54]. This is due to electron scattering from the grain boundaries, surfaces and interfaces, vacancies, and possibly also oxynitrides associated with the polycrystalline TiN [52,55].

Optical and electronic properties of TiN are closely related. A reflection edge in the visible region with a reflectivity minimum at about 450 nm accounts for the golden yellow color of pure, stoichiometric TiN [54,56]. The location of the reflection edge can be tuned by changing the carrier concentration by variations in composition, impurity, or defect concentration [54,57]. Overstoichiometric TiN with excess nitrogen is bronze to brown in color while substoichiometric TiN is bright yellow. Reflectivity and resistivity of sputtered TiN films are inversely correlated, with the reflectivity maximum and resistivity minimum observed for higher deposition temperatures and moderate ion energies [54].

1.4.3 Functional TiN Films as Diffusion Barriers

Their high thermal and structural stability make sputtered TiN films an obvious choice for diffusion barrier materials. But it is their low resistivity that truly sets TiN barriers apart from other transition metal nitrides. The reported value for the pure polycrystalline TiN film is 20-25 μΩ cm, in comparison to up to 200 μΩ cm for TaN and more than 1000 μΩ cm for WN, its strongest contenders [3,45,58]. This allows manufacturers to fully exploit the conductivity advantage of Cu over Al interconnects in microelectronic devices employing TiN barriers [58].

Additionally, microstructure plays a critical role in the continued search for more efficient and reliable barrier materials. Since they lack fast diffusion paths in the form of grain boundaries, single-crystal TiN barriers would suggest themselves as the ideal solution. Chapter 3 stresses the excellent suitability of single-crystal TiN diffusion barriers, which withstand annealing temperatures of 900 °C and show only limited Cu diffusion after annealing at 1000 °C [8]. However, constraints in fabrication and processing, especially thermal budget limitations, make the industrial implementation of such barrier layers not feasible as yet [3].

In comparison, polycrystalline TiN diffusion barrier layers are frequently applied in industry and widely studied in literature. Chamberlain [59] showed that interdiffusion between r.f. sputtered polycrystalline Cu and TiN layers at temperatures up to 600–700 °C is very limited. Presumably, it occurs via grain boundary or dislocation mechanisms. Eventually, the barrier does not fail due to dissociation by a chemical reaction, since Ti is bonded with N and therefore not freely available to react with Cu, but by the formation of an intermetallic compound of Cu and Si after the diffusion of Cu along grain boundaries or other defects in TiN [58]. This failure mechanism is presented in more detail in chapter 5. A promising approach to improve the TiN barrier efficiency is therefore densification of grain boundaries. In Al metallization schemes, the inherent formation of Al-oxides at grain boundaries is often exploited to stuff the boundaries [60–63]. However, this is thermodynamically not favorable in Cu metallization [63,64]. Moreover, grain boundary stuffing goes along with a resistivity increase in the TiN layer. As such, it is also responsible for the broad range of resistivity values for polycrystalline TiN available in literature [58].

Another strategy is to tune the microstructure of the TiN barrier layer by influencing the ad-atom mobility during film growth via deposition parameters such as substrate temperature and bias potential [5]. This in turn affects the overall film density, which has been identified as one of the decisive factors determining the barrier breakdown temperature [65]. Therefore, chapter 4 presents a comparative study of Cu diffusion in dense single- and dense polycrystalline TiN barrier layers sputter-deposited with the same parameters at a substrate temperature of 700 °C [9]. Thus, diffusion phenomena and mechanisms in two TiN films which differ from each other only in the presence of grain boundaries can be compared directly for the first time.

Another way of film densification without making use of external substrate heating is presented in chapter 6. There, the pulsed irradiation of a TiTaN growth surface with only a few at.% of energetic Ta ions provides the necessary mobility to ad-atoms to attain dense films, despite the lack of thermally driven ad-atom diffusion.

1.5 TRANSMISSION ELECTRON MICROSCOPY

1.5.1 Fundamentals of TEM

TEM is a uniquely versatile technique in materials science and gives information on the structure, topology, morphology, elemental composition, and chemical state of materials [66]. The measurement principle is based on the interaction of a high-energy electron beam with a sufficiently thin specimen [7]. This incident electron beam can be considered coherent, and its wavelength λ is determined by the acceleration voltage V (relativistic treatment) [67]:

$$\lambda = \frac{h}{\sqrt{2m_0 eV\left(1+\frac{eV}{2m_0c^2}\right)}}\,. \tag{7}$$

Here, h is Planck's constant, m_0 the electron rest mass, e the elementary charge, and c the velocity of light.

The achievable spatial resolution in TEM is far superior to that of any conventional visible-light microscope, since the smallest distance resolvable with a microscope is directly proportional to the wavelength of the radiation used for imaging (Rayleigh criterion). However, even in TEM the ultimate resolution is still restricted by instrumentation instabilities, lens defects and specimen thickness [67]. Other limitations of the technique include the difficult, time-consuming, and destructive preparation of electron-transparent specimens, the small sampling volume, often difficult image interpretation, and possible electron beam damage to the specimen material [67].

In this study, a FEI Tecnai G^2 TF 20 UT TEM operated at 200 kV in high vacuum conditions was used for thin film characterization. A field emission gun serves as the electron source, which produces an electron beam of higher brightness and spatial coherence than thermionic guns. Going from the gun to the screen, the TEM can be divided into two parts, the illumination and the imaging system, as schematically shown in Fig. 6. The illumination system (Fig. 6 (a)) extends from the electron gun to the sample and contains the condenser lenses one (C1) and two (C2). In conventional TEM mode, the condenser lenses and associated apertures form a (nominally) parallel beam, while in scanning TEM (STEM) configuration, the beam is convergent. In general, the illumination system controls the intensity, coherency, convergence, current, and centering of the electron beam [67].

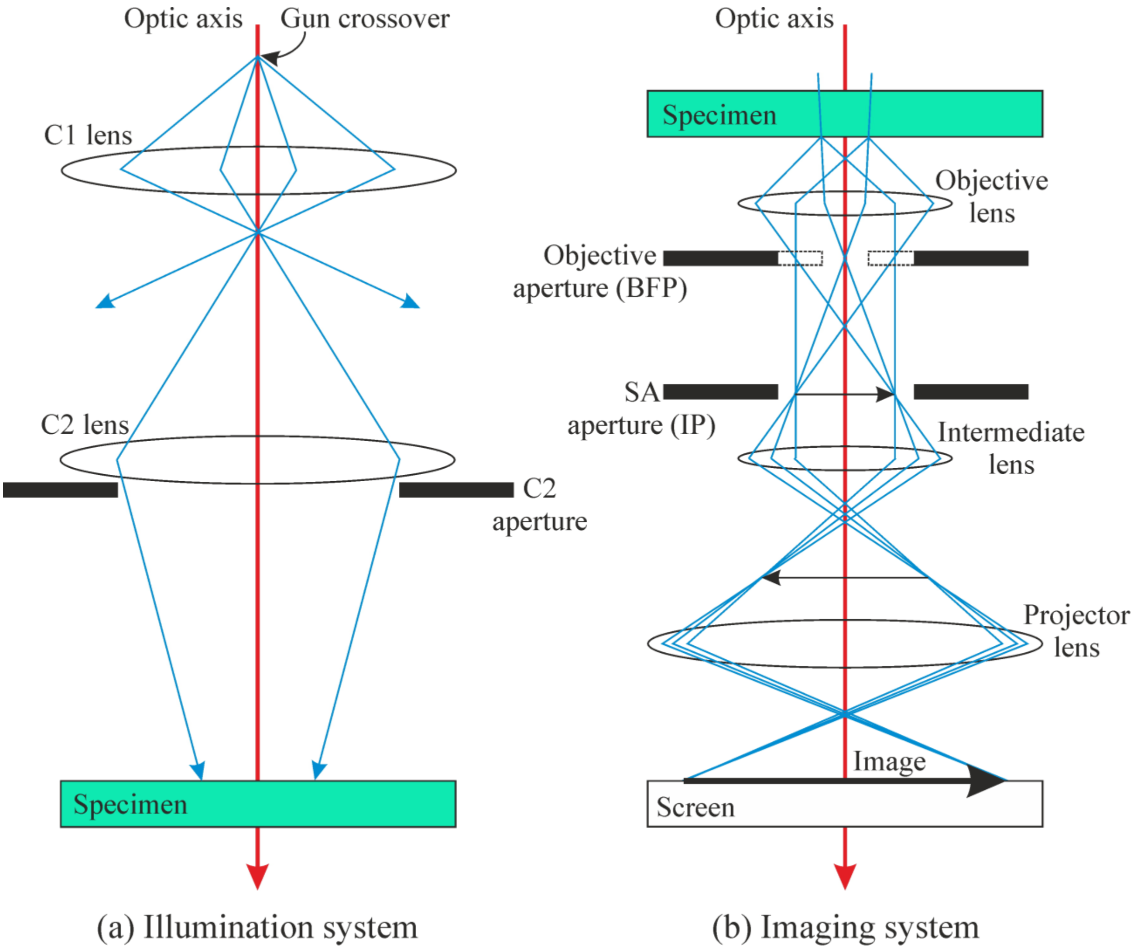

Figure 6: Simplified outline of a TEM consisting of the (a) illumination and (b) imaging system. The illumination system in (a) is depicted in conventional TEM mode, with an underfocused C2 lens forming a nominally parallel electron beam at the specimen. The imaging system in (b) is shown in imaging mode (note that the SA aperture would normally be retracted in imaging mode). A small objective aperture as indicated by the dashed rectangles can be used to block scattered electrons and thus form a bright-field image [1].

The part of the TEM column reaching from the specimen to the fluorescent viewing screen is termed imaging system (Fig. 6 (b)). It hosts the objective lens and aperture, the selected area (SA) aperture, an intermediate lens, and the projector lens. The objective lens disperses electrons emerging from the specimen to form a diffraction pattern in the back-focal plane (BFP), then recombines them to create an image in the image plane (IP). Thus, either the diffraction pattern or the image can be projected onto the viewing screen by adjusting the intermediate lens. If its object plane coincides with the BFP of the objective lens, a diffraction pattern is created, if it coincides with the IP of the objective lens, an image is visible on the screen. In imaging mode the objective aperture is used to cut off scattered electrons from image formation (indicated by the dashed rectangles in Fig. 6 (b)). In diffraction mode the SA aperture is employed to select a specific specimen area from which a selected area electron diffraction pattern (SADP) is collected. These patterns form the basis for all high-resolution TEM investigations, since they allow the specimen to be tilted to a specific zone axis [67]. Electron diffraction in a crystalline TEM specimen proceeds similar to X-ray diffraction, with the chief difference that electrons are not reflected but transmitted through the lattice planes. An electron diffraction pattern provides information about the crystallographic features (lattice parameter, symmetry, texture), grain morphology, and orientation of different phases in a material [67].

1.5.2 Contrast Formation in TEM

A. Bright-field and dark-field contrast

In conventional TEM mode, the operator can shift the objective aperture either to select the direct beam or a diffracted beam from a SADP. Bright-field images are formed by the direct electron beam. In this case, contrast formation is based on the weakening intensity of the direct beam after interaction with the specimen. On the other hand, dark-field images are generated by one or more diffracted beams. Only crystals oriented according to the chosen diffracted beams will appear in these images [67].

In STEM mode, the direct and diffracted beams are not selected by an aperture, but by an on-axis bright-field detector or an off-axis annular dark-field detector, respectively.

B. Mass-thickness contrast

Mass-thickness contrast develops due to changes in the amplitude of the electron wave as it passes through the specimen. Electrons are scattered from their direct path through the sample because of Coulomb interaction with specimen atoms. Since heavier atoms carry a higher number of charges, they are more likely to deflect an electron. The same principle applies to thicker sample regions, where the likelihood of a scattering event is increased due to the higher number of specimen atoms in the path of the electron. As a result, in a bright-field image thicker/higher-mass regions of the sample appear darker than thinner/lower-mass areas. The opposite holds true for dark-field images [66,67].

C. Diffraction (Bragg) contrast

Diffraction contrast is also based on variations in the electron wave amplitude. When periodically arranged atoms in a crystal act as scattering centers, constructive or destructive interference of the scattered electrons occurs. Thus, discrete diffracted electron beams are formed. Similar to X-ray diffraction (see chapter 1.7.1), the condition for constructive interference is given by Bragg's law,

$$n\lambda = 2d \, sin\theta_B. \quad (8)$$

Here, n is an integer, λ the electron wavelength, d the lattice spacing in the crystalline specimen, and θ_B the Bragg angle. Furthermore, the structure factor of the investigated material has to be accounted for, since it can modulate or completely cancel some reflections in the diffraction pattern [7,66,67].

D. *Z*-contrast

Atomic number (*Z*) contrast imaging is a STEM technique, where a high-angle annular dark-field (HAADF) detector gathers electrons scattered at angles larger than 50 mrad. This excludes contributions from Bragg diffracted electrons. Heavy atoms with high atomic numbers are more likely to scatter electrons to such high angles, so sample regions containing heavier atoms will appear brighter in the ensuing dark-field image [7,66,67].

Particular examples of the suitability of *Z*-contrast imaging for thin film interdiffusion assessment are presented in chapters 3 and 6, where Cu diffusion and segregation zones are identified by contrast variation in a HAADF image [8].

E. Phase contrast (HRTEM)

High-resolution TEM (HRTEM) and phase contrast imaging can be used interchangeably. The technique is based on the relative phase shift of the direct and diffracted electron waves after interaction with the atomic potentials of the sample atoms. This phase shift is determined by the strength and spacing of the periodic lattice potential. Thus, an image related directly to the structural periodicity of the crystalline specimen is formed. The image resolution increases with the number of beams contributing to the image [7,67]. Due to the sensitivity of the technique, phase contrast images can be especially difficult to interpret, but on the other hand provide an insight into the atomic structure of materials. However, it cannot be stressed often enough that the location of a fringe in the HRTEM image does not necessarily correspond to the location of a lattice plane. But since the intensity in a phase contrast image fluctuates with a periodicity directly related to the spacing of the lattice planes, HRTEM gives information about lattice spacing and orientation [67].

To make the matter more complicated, electron waves are not only phase shifted due to interaction with the lattice potential of the crystalline sample, but also by a microscope phase factor. A phase contrast transfer function (CTF) describes how aberrations and other system artifacts in a TEM influence the phase contrast image of a specimen [67,68]. A representative evolution of the CTF with the spatial frequency (reciprocal lattice spacing) q for the FEI Tecnai G^2 TF 20 UT TEM used within this study is plotted in Fig. 7 [69]. The point resolution of the microscope is defined as the inverse spatial frequency where the CTF first

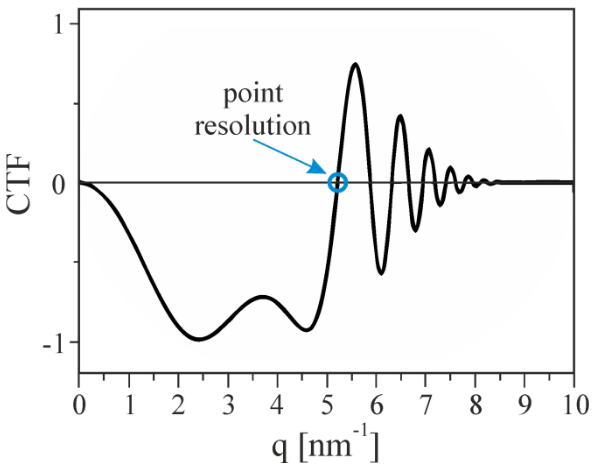

Figure 7: Representative CTF of the utilized FEI Tecnai G^2 TF 20 UT TEM adapted from [69]. The point resolution is 1.9 Å.

becomes zero. The TEM utilized within this study can reach a point resolution of 1.9 Å. A positive CTF represents negative phase contrast, and atomic columns appear bright on a dark background. Whenever the CTF crosses the abscissa, there is a contrast inversion, which makes intuitive image interpretation impossible [67]. Scherzer recognized the possibility of optimizing the CTF by balancing the detrimental effect of spherical aberration in the lens system (with the spherical aberration coefficient C_S) against a negative defocus. This is known as the Scherzer defocus Δf_{Sch}, with λ as the electron wavelength [67,70].

$$\Delta f_{Sch} = -1.2\sqrt{C_S \lambda}\,. \tag{9}$$

In this study, HRTEM is employed to investigate the atomic structure of the TiN/Cu thin film system, especially at the interfaces. To this end, cross-sectional phase contrast images of the layer stacks are presented and discussed in chapters 3 and 4.

1.5.3 Analytical TEM

Analytical TEM comprises the techniques of energy-dispersive X-ray spectroscopy (EDX), electron energy-loss spectroscopy, and energy-filtered TEM. Only the first will be discussed within this thesis. Analytical TEM is typically performed in STEM mode, where the beam is already converged to form a probe for analysis [67,71].

When interacting with the specimen, electrons generate characteristic X-rays with a well-defined, element-specific energy as well as Bremsstrahlung. The former originate from the ejection of a core or inner-shell electron leading to a cascade of electron transitions (denoted as K, L, M, etc.). The latter arises as a background signal because of the deceleration of electrons by electrostatic interaction with the atomic nuclei. Fig. 8 shows two recorded X-ray spectra

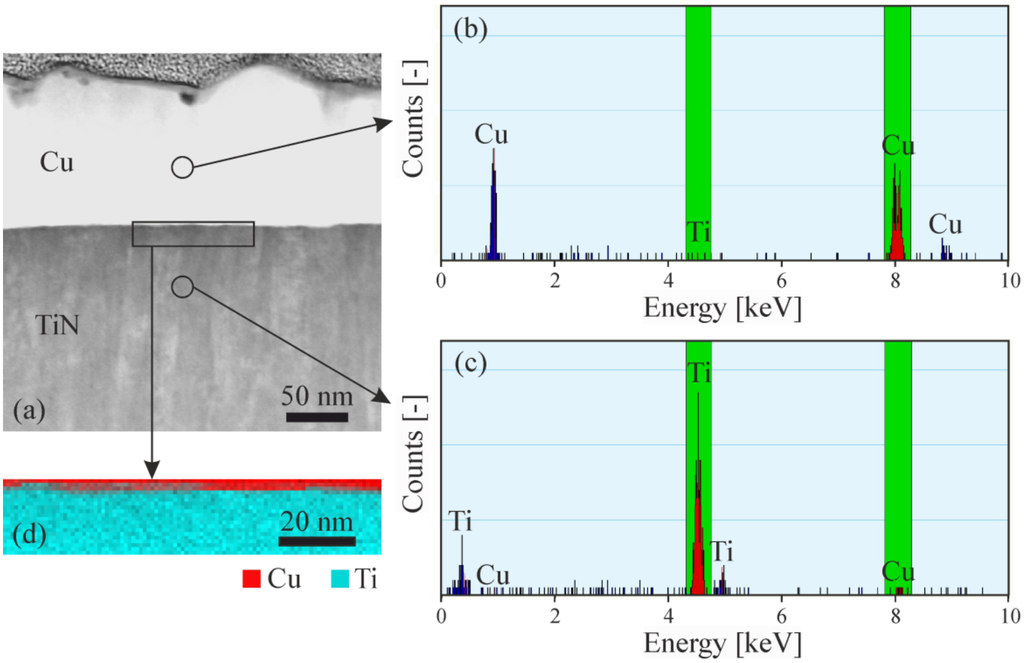

Figure 8: (a) STEM HAADF image of a Cu/polycrystalline TiN interface after annealing the sample at 600 °C for 1 h. Corresponding EDX spectra were obtained within the (b) Cu and (c) TiN layer. The Cu-K and Ti-K peaks are highlighted in both spectra due to their suitability for subsequent elemental mapping because of high counts and no peak overlap. An elemental map of the Cu-K and Ti-K edges recorded across the interface as indicated by the rectangle is shown in (d) [1].

encountered while investigating a TiN/Cu thin film interface. EDX spectra can be obtained from distinct analysis points within the sample, but also as one-dimensional elemental profiles or even two-dimensional elemental maps. Examples and their value for interdiffusion studies in bilayer thin film systems are discussed in chapters 3, 4, and 6. Fig. 8 (d) displays such an exemplary elemental map of the Cu-K and the Ti-K edges as found for a polycrystalline TiN/Cu stack after annealing at 600 °C for 1 h. No interdiffusion of the elements is observable.

1.6 ATOM PROBE TOMOGRAPHY

1.6.1 Fundamentals of APT

APT provides a three-dimensional reconstruction of a specimen with single-atom sensitivity. Thus, the technique can be used to obtain elemental concentration profiles in any direction in the specimen, to characterize interfaces and interdiffusion, and to investigate ordering, dopant interactions, cluster formation, or early stages of precipitation in a material [72–74].

The measurement principle of APT is based on the field-evaporation of atoms (or, more correctly, ions) from a specimen tip. This is facilitated by an intense electric field at the tip apex, which is generated by a high voltage V applied to the specimen. The electric field strength F at the tip apex is inversely proportional to the tip radius R.

$$F = \frac{V}{k_f R}\,. \tag{10}$$

In this equation, k_f is a constant describing the tip shape and its electrostatic environment. It is called the field factor [73].

The field-evaporated specimen ions are accelerated along the electric field lines away from the tip surface. This can be accounted for by a simple point-projection. Assuming the detector is a distance L away from the tip, the image magnification M_{proj} can be expressed as

$$M_{proj} = \frac{L}{\xi R}\,. \tag{11}$$

Here, ξ is an instrument parameter called the image compression factor, describing the deflection of the electric field lines. In the LEAP 3000X HR APT system utilized within this study it has a value of 1.65. With a sufficiently sharp specimen tip, this typically yields a magnification higher than 10^6, viz. enough to resolve the positions of individual atoms [73].

The chemical species of the field evaporated ions can be identified with the help of a position-sensitive time-of-flight (TOF) mass spectrometer. High-voltage (HV) or laser pulsing is employed to determine the exact start time for the field-evaporation event [75]. In modern local electrode atom probe (LEAP) instruments, the counter electrode is mounted in close proximity to the specimen, which significantly enhances the electric field and thereby lowers the necessary applied voltage. Advantages of this setup include higher data collection rates and

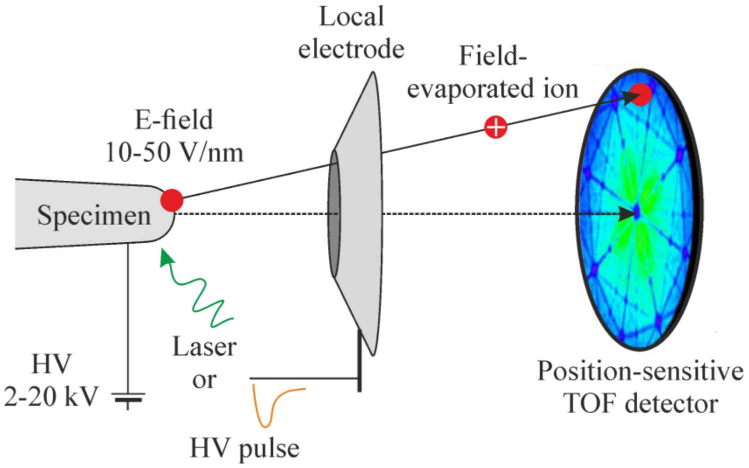

Figure 9: Schematic (not to scale!) of a LEAP setup. An ultra-high vacuum chamber hosts the cryogenically cooled specimen, the local electrode, and a position-sensitive TOF detector. Field-evaporation of ions is induced either by high-voltage or laser pulsing [1].

better mass resolution, as well as an increased field-of-view [72]. A schematic of such a LEAP system is shown in Fig. 9.

In general, an APT comprises an ultra-high vacuum chamber with a base pressure in the order of 10^{-11} mbar. The specimen is mounted on a stage that can be moved in x-, y-, and z-direction and aligned with the local electrode aperture. The distance between specimen tip and local electrode is approximately 20 µm, while the distance L between the specimen and the detector is 382 mm in the LEAP system employed for this study (distances not to scale in Fig. 9) [73]. Prior to measurement, the APT specimen is cooled to cryogenic temperatures as low as 20 K, to limit the thermal movement and diffusion of tip surface atoms. A standing DC voltage in the range of 2-20 kV is applied to the tip to generate an electric field of 10-50 V/nm at the apex. In the case of laser-assisted LEAPs, a laser beam is focused on the specimen tip. The LEAP system used for this work is equipped with a green laser (λ = 532 nm). Laser pulsing can be achieved with sub-ns durations at frequencies larger than 100 kHz, whereas in voltage pulsing mode, the counter-electrode is connected to a HV pulser delivering negative HV pulses in the ns range [72,73].

A delay-line detector measures the TOF of each field-evaporated ion and records the impact position. Thereby, the TOF is defined as the time between pulse initiation and impact on the detector. It can be directly related to the mass-to-charge ratio (m/n) of the ion.

$$\frac{m}{n} = 2eV\left(\frac{TOF}{L}\right)^2. \tag{12}$$

Here, e is the elementary charge, V is the total applied voltage, and L is the flight path (382 mm) [73].

A LEAP system operated in laser pulsing mode typically has a mass resolving power (MRP, *m/Δm* at FWHM) of 1000, while the field-of-view is still larger than 150 nm. More than 10^7 atoms can be measured per hour with an analytical sensitivity as high as 1 ppm. The spatial resolution is better than 0.3 nm in all directions and volumes on the order of 10^6 nm^3 can be successfully analyzed [72,75].

However, as every characterization technique, APT also has its limitations, especially when it comes to the difficult and time-consuming sample preparation involved. An APT specimen must meet three fundamental requirements: *(i)* the tip must be sharp enough to enable field evaporation, *(ii)* it must mechanically tolerate the applied electric field, and *(iii)* the region of interest must be included within the first 100 nm of the specimen apex [72]. There are two established techniques to produce such specimens, electropolishing and site-specific focused ion beam (FIB) methods. The latter is the method of choice for APT samples investigated within this study, since it is necessary that the interfacial region between the thin films is contained in the tip volume.

It is also not certain that all prepared tips will subsequently run in the experiment. Some specimens might fracture as soon as the standing voltage is applied. Once the specimen is measured, sample reconstruction can be problematic. This is one of the main limitations in the case of more complex material structures such as thin film stacks, as will be discussed in chapter 1.6.2.B [75].

1.6.2 Measurement and Data Evaluation

A. Measurement parameters

APT measurement parameters can be tuned to optimize the MRP and at the same time minimize background noise in the recorded mass spectrum. In a laser-assisted measurement, these parameters are [72]:

- *Laser pulse rate:* The laser pulse rate should be as high as possible to promote a high acquisition rate, but still low enough so that ions with a long TOF can reach the detector within the pulse duration.
- *Laser pulse energy:* High laser pulse energies lower the required evaporation field and result in mass spectra with high MRP and low background. However, it has been reported in literature that low laser energies are beneficial when measuring oxides and nitrides [72,76,77]. Similar observations were made when measuring specimens in this study.
- *Base temperature:* A low base temperature (20-60 K) is always preferable, as it restricts surface diffusion and results in better heat transport away from the tip apex. Low-temperature measurements therefore yield mass spectra of good data quality. However, not all specimen materials can withstand the associated mechanical stress.

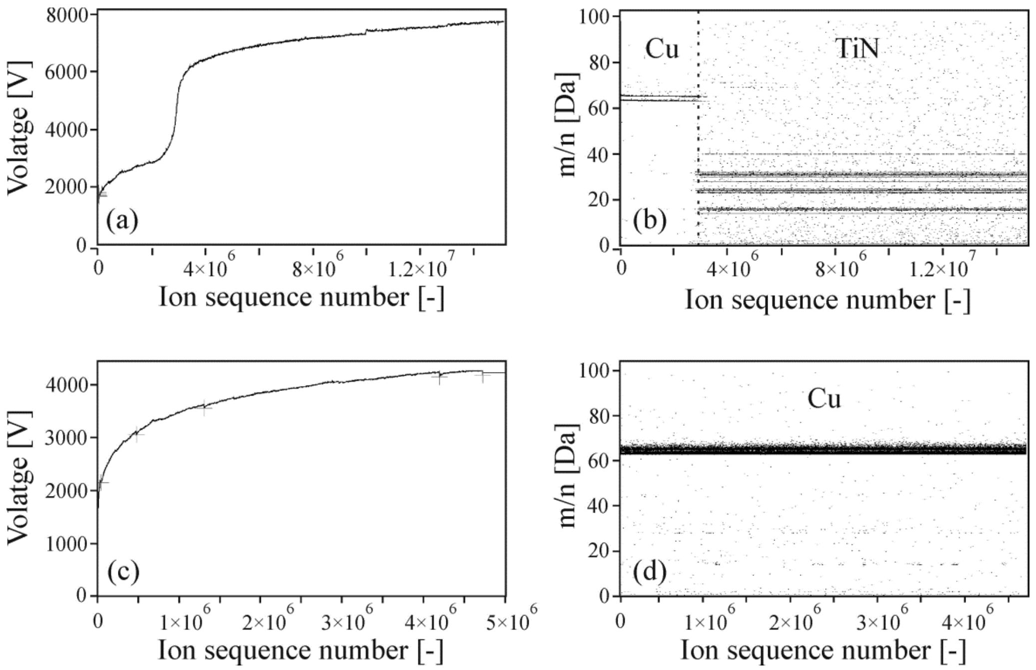

Figure 10: Evolution of evaporation voltage with ion sequence number (left) and corresponding mass-to-charge ration *m/n* of the detected ions (right) shown for (a,b) a specimen containing a TiN/Cu interface and (c,d) a specimen prepared from a single Cu layer [1].

B. Data reconstruction

APT data reconstruction follows an algorithm that links the detector hit sequence and impact position of ions to their original (*x,y,z*)-position on the specimen surface. The underlying mathematical procedure was developed by Bas *et al.* [78] and later refined for a larger field-of-view by Geiser *et al.* [79].

In order to maintain a constant evaporation rate during a LEAP measurement, the standing voltage applied to the specimen tip is continuously and automatically increased. The voltage evolution over ion sequence number (translating to the *z*-coordinate) is shown in Fig. 10 for a thin film bilayer specimen containing a TiN/Cu interface (Fig. 10 (a)) and for a specimen cut from a single Cu layer (Fig. 10 (c)). In the elemental Cu film, the evaporation voltage increases steadily. In contrast, a discontinuity is encountered when analyzing the tip containing the interface. This discontinuity arises at the transition from the Cu to the TiN film (Fig. 10 (d)), and is a manifestation of the higher evaporation field of TiN compared to Cu. In the final reconstruction this sudden increase in evaporation voltage can lead to artefacts. It will be examined in more detail when discussing three-dimensional reconstruction later in this chapter.

Acquired TOF data is converted to *m/n* according to equation (12) [72], resulting in a cumulative mass spectrum. The correct peak assignment in this spectrum can be aggravated by peak overlaps, deviations from natural isotope abundances, and the appearance of molecular ions. The problem of peak overlaps in mass spectra is also addressed in chapter 5, where peaks related to Si^{2+} and N^+ and Si^+ and

N^{2+} ions are demonstrated to be successfully separated thanks to the excellent mass resolution of APT. Spatial reconstruction of the acquired data is based on magnifying detector hit positions to real-space *x,y*-coordinates (see equation 11), while the *z*-component is determined from the ion number sequence, the assigned ionic volume and the estimated imaged area of the tip surface. The radius evolution of an analyzed tip can be modelled with two different approaches [72]:

- *Shank evolution:* The increase of the radius during evaporation from the tip is based on geometrical parameters such as the initial tip radius and the shank angle, which are measured in an electron microscope prior to the APT investigation. A specimen reconstructed based on the shank evolution is shown in Fig. 11 (a).
- *Voltage evolution:* The voltage evolution reconstruction protocol is based on equation (10), so that the radius increases with the applied voltage. However, if the evaporation field is not constant over the analysis direction, this leads to a discontinuity in the voltage curve as shown for a TiN/Cu stack in Fig. 10 (a). Naturally, a reconstruction based on such a voltage evolution is distorted. In case of a low-field material on a high-field material (e.g. Cu on TiN), the resultant tip profile will look as displayed in Fig. 11 (b).

Currently, the characterization of thin film stacks remains a challenging task in APT, since the reconstruction protocol cannot account for changes in evaporation

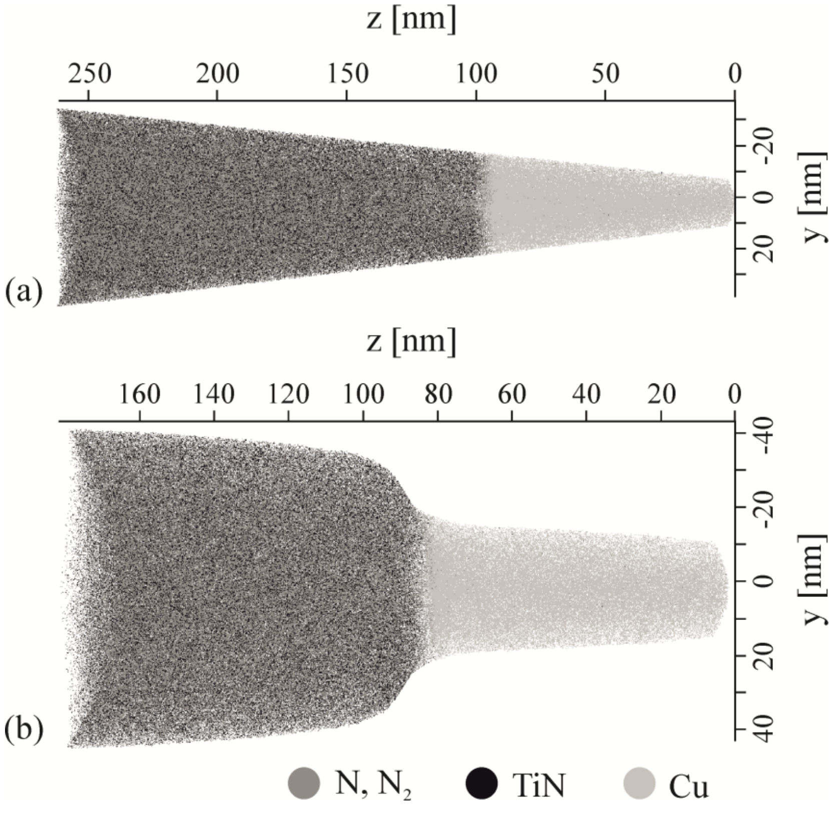

Figure 11: Three-dimensional reconstructions of a single-crystal TiN/Cu bilayer specimen in (a) shank evolution and (b) voltage evolution mode. Each plotted data point represents one (molecular) ion, but only a fraction of all measured ions is plotted for better visualization [1].

field within the measurement [80–82]. Investigated specimens in the present study were reconstructed in shank and voltage evolution mode, and both Cu and Ti were tested as primary elements determining the evaporation field. All reconstructions were evaluated in terms of interface flatness and relation to the tip geometry observed in the scanning electron microscope. Reconstructions presented in chapters 3 and 4 are shown in voltage evolution mode, with Cu as the element determining the evaporation field. In chapter 5, APT reconstructions are displayed in shank evolution mode to better highlight the different diffusion characteristics of Cu and Si in the whole analyzed tip volume.

1.6.3 Thin Film Interdiffusion Studies in APT

Lately, APT has gained recognition as a valuable tool for the investigation of interdiffusion phenomena in thin film systems, due to the high spatial resolution and superior chemical sensitivity inherent to the technique. For example, laser-assisted APT has been used to analyze the spinodal decomposition of TiAlN coatings. In this context, spinodal decomposition can be viewed as an uphill diffusion process described by a negative diffusion coefficient [83–85]. APT studies concerning the distribution and segregation of dopants in materials for microelectronics are also available in a comprehensive review on the subject by Kelly *et al.* [86]. The following chapters will briefly showcase two examples of how interdiffusion in the TiN/Cu thin film system has been explored and visualized by APT within the present study.

A. One-dimensional chemical profiling

One-dimensional chemical depth profiling across interfaces is an obvious way to characterize interdiffusion in layered material systems. This is also possible with other, less laborious techniques; however, APT offers two main advantages: *(i)* Interfaces do not necessarily have to be oriented normal to the analysis direction. The APT software package allows for the calculation of profiles along any direction in the dataset. *(ii)* Profiles can be calculated for single ions, molecular ions, decomposed ions or combinations of ions. Fig. 12 depicts a comparison of Cu concentration profiles in single-crystal and polycrystalline TiN films before and after annealing treatments. The profiles are acquired across the interfaces 20-30 nm into the respective TiN barrier layers. The interface is defined at a Cu concentration of 50 at.% and the profiles are calculated with a fixed bin width of 0.1 nm. It is apparent from Fig. 12 that Cu diffusion into the single-crystal layer is only active during the 12 h annealing treatment at 1000 °C, while the diffusion depth in the case of the polycrystalline barrier is already more than 20 nm after annealing at 900 °C for 1 h. This is reasonable given the different mechanisms of lattice and grain boundary diffusion.

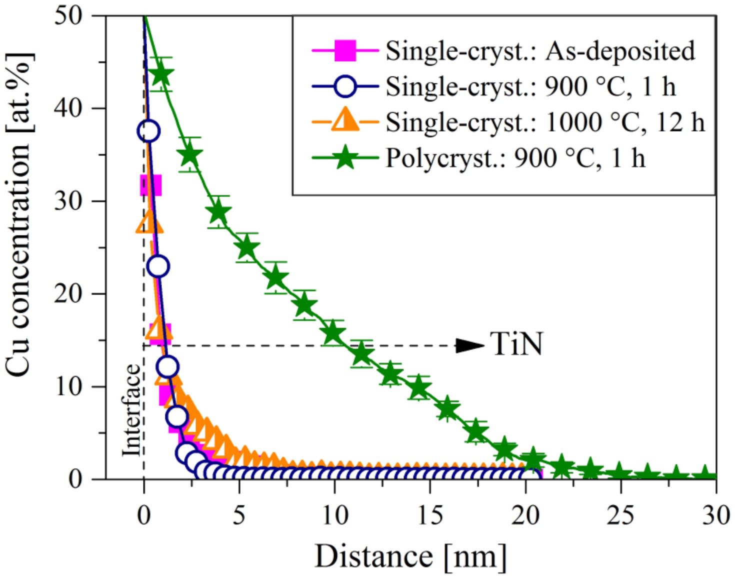

Figure 12: One-dimensional Cu concentration profiles with error bars in single-crystal and polycrystalline TiN diffusion barrier layers before and after annealing treatments. Not every measured data point is represented by a symbol in the plots. The error bars in the single-crystal cases are smaller than the symbols and therefore not visible [1].

B. Proximity histograms and isoconcentration surfaces

Isoconcentration surfaces can be constructed within an APT dataset by defining a specific threshold value for an arbitrary ion species or even an ion ratio. Instead of obtaining a one-dimensional profile along an explicit direction, so-called proximity histograms can be calculated with respect to distance from the isoconcentration surface. This approach restricts the influence of the interface roughness on the acquired interdiffusion profile over the interface [72]. Therefore, it is useful when studying the uniform lattice diffusion in single-crystal TiN barriers, but not applicable to analyze localized grain boundary diffusion phenomena.

Exemplary isoconcentration surfaces illustrating Cu diffusion in single- and poly-crystalline TiN films vacuum annealed at 900 °C are displayed in Fig. 13. In the latter case, non-uniform diffusion of Cu presumably occurring along a grain boundary or even a triple junction is observable (Fig. 13 (b)). The volume concentration plots used to demonstrate this in chapter 4 are an extension of the isoconcentration surfaces.

Isoconcentration surfaces can also be utilized to illustrate local elemental concentrations in different sample regions as presented in chapter 5. Thus, it is shown that while the overall Si concentration in the studied underdense TiN layer is below a certain threshold value of 10 at.% after a 1 h annealing treatment at 700 °C, the Cu/TiN interface is enriched in Si. Furthermore, a pronounced and correlated accumulation of Cu and Si most likely segregated at a grain boundary is revealed. Conclusions based on these observations are further discussed in chapter 5.

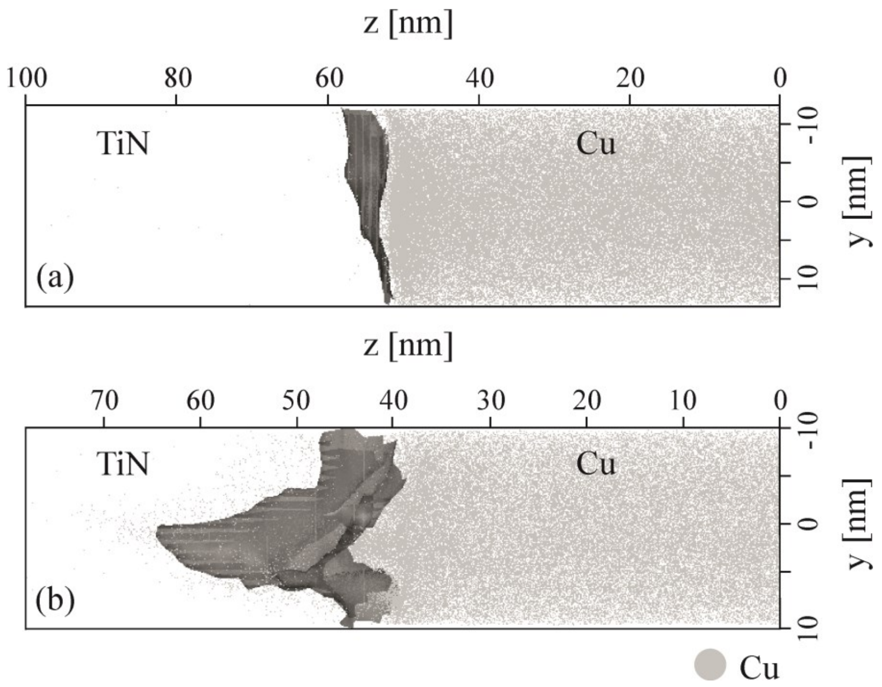

Figure 13: Side-view of cylindrical regions of interest containing isoconcentration surfaces plotted at 50 at.% Cu for a (a) single-crystal and (b) polycrystalline TiN diffusion barrier layer after a 1 h annealing treatment at 900 °C. Ions related to the TiN film are not plotted for better clarity [1].

1.7 OTHER THIN FILM CHARACTERIZATION METHODS

1.7.1 X-ray Diffraction and Reflection

X-ray diffraction (XRD) and reflection are versatile, non-destructive thin film characterization techniques. Applications range from phase analysis, to the investigation of crystalline structure and epitaxial orientation, over the measurement of interfacial roughness and film density, to the determination of texture and residual stress in films. In a crystalline material, XRD proceeds according to Bragg's law as described for TEM in section 1.5.2.C, with the difference that now X-rays instead of electron waves are diffracted by the lattice planes. Bragg's law shall be repeated here, due to its vital importance for understanding diffraction. From geometrical considerations illustrated in Fig. 14, it is found that constructive interference of X-rays occurs when

$$n\lambda = 2d\ sin\theta_B\ , \tag{13}$$

with n as an integer, λ as the X-ray wavelength, d as the lattice spacing in the crystalline specimen, and θ_B as the Bragg angle [87,88].

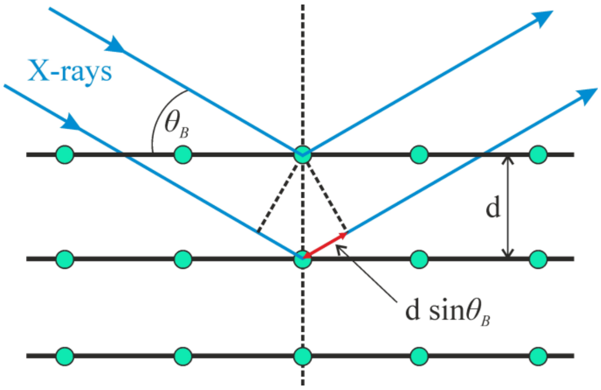

Figure 14: Geometrical representation of X-ray diffraction occurring at lattice planes in a crystalline material.

Depending on the arrangement of the X-ray source, the sample, and the detector in the diffraction system, several different XRD techniques can be distinguished. The most common mode is a so called Bragg-Brentano (symmetric $\theta/2\theta$) scan, which is used to identify chemical phases in a material. A $\theta/2\theta$ diffraction pattern consists of the set of scattering angles 2θ where Bragg reflections occur and their corresponding integral intensities. Thus, the components of the analyzed material can be identified by comparison to databases. However, the penetration depths of X-rays in the symmetric $\theta/2\theta$ configuration are in the 10–100 µm range, much too large for thin film investigations [88]. Therefore, thin films are often analyzed in grazing incidence configurations, where the X-ray beam is incident at a small angle (< 5°), thus limiting the penetration depth. The detector is scanned over a 2θ range of interest. Due to the geometrical arrangement in this mode, the Bragg condition can only be satisfied in polycrystalline materials [87]. This technique is thus capable of verifying the presence or absence of any polycrystalline components in single-crystal thin films as demonstrated in chapter 4 [9].

Single-crystal TiN/Cu bilayers are also characterized by pole-figure measurements in chapter 3 [8]. In these measurements, a reflection from a specified crystallographic zone axis is scanned under various orientations by simultaneously tilting and rotating the sample. The results are plotted in a stereographic projection. This yields information about the epitaxial relationship between the thin film and the substrate or about preferred orientation in polycrystalline films [87,88].

To conclude this section, lastly X-ray reflectivity (XRR) measurements should be mentioned. They are especially relevant for the characterization of bi- or multilayered thin film systems. The XRR setup is the same as for the Bragg-Brentano geometry, only with much smaller $\theta/2\theta$ angles (usually $2\theta < 5°$). In the resulting reflectogram, typically two regions are fitted to provide information: *(i)* The plateau of constant reflectivity for scattering angles smaller than the critical angle is caused by the total reflection of the incident beam on the sample surface. Thus, the critical angle can be determined as the angle where the reflected intensity first starts to decrease. This angle in turn can be used to calculate the mass density of the top layer. *(ii)* In the region above the critical angle, the reflected intensity decreases over several orders of magnitude. Under ideal measurement conditions, this intensity decrease is accompanied by the appearance of intensity oscillations, so-called Kiessig fringes. The intensity decrease and oscillations provide information about film thickness, as well as on the roughness of external and internal interfaces in layered systems [87,88].

1.7.2 Scanning Electron Microscopy

A scanning electron microscope (SEM) is used to characterize the topography and structure of sample materials. An electron beam with an energy of 100 eV to 30 keV scans the surface or a cross-section of the sample. The thereby created secondary or backscattered electrons are collected by an appropriate detector. Additionally, excited characteristic X-rays provide elemental information following the same principle as described in chapter 1.5.3 for analytical TEM. A main advantage of SEM is that there is no need for extensive sample preparation.

However, the achievable resolution is significantly lower than for TEM techniques [87].

Secondary electrons (SEs) are ejected due to inelastic interactions of the beam electrons with the valence electrons of the specimen atoms. The major part of the detected SEs has an energy of less than 10 eV. Therefore, they do not travel far in the sample and can be considered a surface sensitive signal. The contrast formation in SE SEM images is mainly governed by the tilt angle and topography of the investigated sample surface, often giving these micrographs a somewhat three-dimensional appearance [87,89]. An example of a plan-view SE SEM image of a de-wetted Cu layer on an otherwise bare $Ti_{0.92}Ta_{0.08}N$ film surface is shown in Fig. 15 (a).

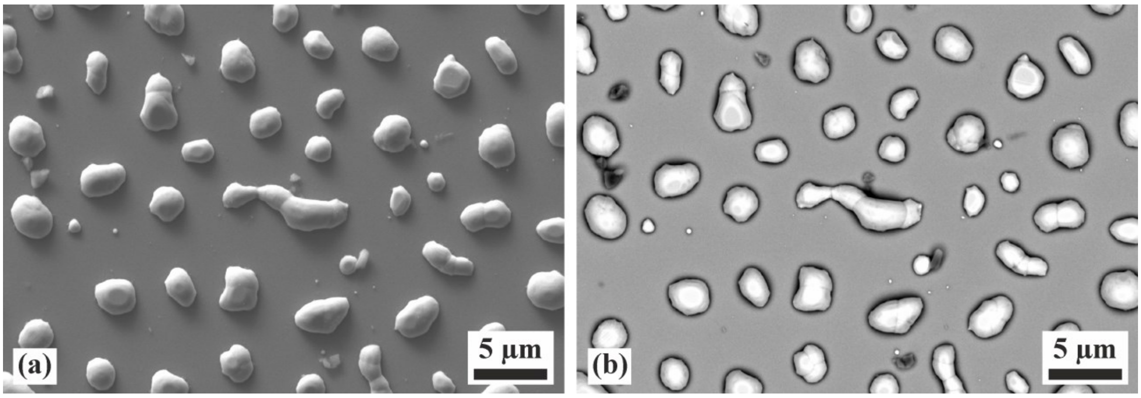

Figure 15: Plan-view scanning electron micrographs of a de-wetted Cu layer on a $Ti_{0.92}Ta_{0.08}N$ film obtained on the same sample area with a (a) secondary electron detector and a (b) backscattered electron detector.

Backscattered electrons (BSEs) are the result of elastic interactions of beam electrons with nuclei of sample atoms. The involved excitation volume depends strongly on the energy of the incident beam. Atomic nuclei can scatter incident electrons by angles of up to 180°. The fraction of beam electrons scattered in such a way is determined by the atomic number Z of the scattering atoms. In the resulting BSE SEM micrograph, sample areas of high average Z appear brighter than those of low average Z. Therefore, these images can be used to gain information about the spatial distribution of elements within a specimen depth of approximately 1 µm [87,89]. Fig. 15 (b) shows a plan-view BSE micrograph of the same sample area as depicted in Fig. 15 (a). The Cu islands apparent on the annealed sample have a higher average atomic number than the underlying $Ti_{0.92}Ta_{0.08}N$ film, and are therefore imaged brighter.

SE as well as BSE SEM investigations of pristine and annealed sample surfaces are presented in chapters 5 and 6 to illustrate interdiffusion damage.

1.7.3 Four-Point-Probe Sheet Resistivity

Four-point-probe (FPP) sheet resistivity measurements are an important tool for the assessment of interdiffusion damage in Cu metallization/barrier/Si stacks. The breakdown of the barrier layer can be defined as the annealing temperature and time after which a specific compound is formed by constituents of the Cu metallization and the Si substrate. Therefore, many studies take the formation of the intermetallic η''-Cu_3Si phase, which is the equilibrium phase at room temperature [90,91], as a benchmark in evaluating barrier performance in Cu/barrier/Si systems [2,6,65,92–99]. Increased sheet resistivity of the Cu metallization layer as measured by a FPP setup indicates the presence of this high-resistivity η''-Cu_3Si compound [2,65,92,94,95], as demonstrated in chapters 5 and 6.

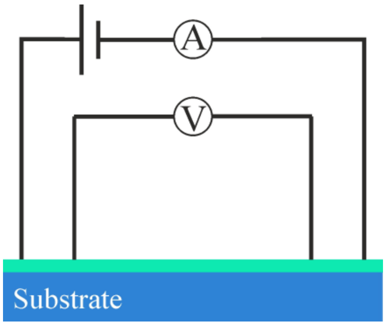

Figure 16: Typical four-point-probe sheet resistivity measurement setup consisting of two pairs of electrode probes.

The measurement principle of FPP is based on the assumption that thin films are essentially two-dimensional systems, so that the current flow is confined to rings in the thin film plane. The FPP setup then consists of two probes which introduce a constant current, while the potential drop on another pair of probes is measured with a high-impedance voltmeter, as schematically shown in Fig. 16. With the measured voltage V, the sheet resistivity ρ can be calculated according to the following formula

$$\rho = \frac{\pi t}{ln2} \frac{V}{I}, \tag{14}$$

where I is the set current and t the film thickness. Thus, the influence of the contact resistance on the overall resistivity is eliminated, allowing for accurate resistivity measurements of values below 100 µΩ cm [100–102].

References

[1] M. Mühlbacher, High-resolution characterization of TiN diffusion barrier layers, Licentiate thesis, Linköping University, 2015.

[2] C. Lee, Y.-L. Kuo, The evolution of diffusion barriers in copper metallization, JOM 59 (2007) 44–49.

[3] A.E. Kaloyeros, E. Eisenbraun, Ultrathin diffusion barriers/liners for gigascale copper metallization, Annu. Rev. Mater. Sci. 30 (2000) 363–385.

[4] International Technology Roadmap for Semiconductors, (2013). http://www.itrs.net/home.html (accessed February 4, 2015).

[5] A. Gupta, H. Wang, A. Kvit, G. Duscher, J. Narayan, Effect of microstructure on diffusion of copper in TiN films, J. Appl. Phys. 93 (2003) 5210–5214.

[6] M. Moriyama, T. Kawazoe, M. Tanaka, M. Murakami, Correlation between microstructure and barrier properties of TiN thin films used Cu interconnects, Thin Solid Films 416 (2002) 136–144.

[7] A.K. Petford-Long, A.N. Chiaramonti, Transmission electron microscopy of multilayer thin films, Annu. Rev. Mater. Res. 38 (2008) 559–584.

[8] M. Mühlbacher, F. Mendez-Martin, B. Sartory, N. Schalk, J. Keckes, J. Lu, L. Hultman, C. Mitterer, Copper diffusion into single-crystalline TiN studied by transmission electron microscopy and atom probe tomography, Thin Solid Films 574 (2015) 103–109.

[9] M. Mühlbacher, A.S. Bochkarev, F. Mendez-Martin, B. Sartory, L. Chitu, M.N. Popov, P. Puschnig, J. Spitaler, H. Ding, N. Schalk, J. Lu, L. Hultman, C. Mitterer, Cu diffusion in single-crystal and polycrystalline TiN barrier layers: A high-resolution experimental study supported by first-principles calculations, J. Appl. Phys. 118 (2015) 085307.

[10] H. Mehrer, Diffusion in solids, 1st ed., Springer, Berlin-Heidelberg-New York, 2007.

[11] A. Fick, Ueber Diffusion, Ann. Phys. 170 (1855) 59–86.

[12] D. Gupta, Diffusion in bulk solids and thin films: Some phenomenological examples, in: D. Gupta (Ed.), Diffusion Processes in Advanced Technological Materials, 1st ed., William Andrew Publishing, Norwich, NY, 2005: pp. 1–68.

[13] D.S. Wilkinson, Mass transport in solids and fluids, Cambridge University Press, Cambridge, 2000.

[14] M. Ohring, Materials Sscience of thin films: Deposition and structure, 2nd ed., Academic Press, San Diego, 2002.

[15] D. Turnbull, R.E. Hoffman, The effect of relative crystal and boundary orientations on grain boundary diffusion rates, Acta Metall. 2 (1954) 419–426.

[16] L.G. Harrison, Influence of dislocations on diffusion kinetics in solids with particular reference to the alkali halides, Trans. Faraday Soc. 57 (1961) 1191–1199.

[17] S.I. Shah, G.H. Jaffari, E. Yassitepe, B. Ali, Evaporation: Processes, bulk microstructures, and mechanical properties, in: P.M. Martin (Ed.), Handbook of Deposition Technologies for Films and Coatings, 3rd ed., William Andrew Publishing, Oxford, 2010: pp. 135–252.

[18] D.M. Mattox, Handbook of physical vapor deposition (PVD) processing, 1st ed., Noyes Publications, Westwood, NJ, 1998.

[19] D. Depla, S. Mahieu, J.E. Greene, Sputter deposition processes, in: P.M. Martin (Ed.), Handbook of Deposition Technologies for Films and Coatings, 3rd ed., William Andrew Publishing, Oxford, 2010: pp. 253–296.

[20] G. Bräuer, B. Szyszka, M. Vergöhl, R. Bandorf, Magnetron sputtering - Milestones of 30 years, Vacuum 84 (2010) 1354–1359.

[21] P.J. Kelly, R.D. Arnell, Magnetron sputtering: a review of recent developments and applications, Vacuum 56 (2000) 159–172.

[22] P.H. Mayrhofer, F. Kunc, J. Musil, C. Mitterer, A comparative study on reactive and non-reactive unbalanced magnetron sputter deposition of TiN coatings, Thin Solid Films 415 (2002) 151–159.

[23] W.D. Sproul, D.J. Christie, D.C. Carter, Control of reactive sputtering processes, Thin Solid Films 491 (2005) 1–17.

[24] K. Sarakinos, J. Alami, S. Konstantinidis, High power pulsed magnetron sputtering: A review on scientific and engineering state of the art, Surf. Coat. Technol. 204 (2010) 1661–1684.

[25] V. Kouznetsov, K. Macák, J.M. Schneider, U. Helmersson, I. Petrov, A novel pulsed magnetron sputter technique utilizing very high target power densities, Surf. Coat. Technol. 122 (1999) 290–293.

[26] U. Helmersson, M. Lattemann, J. Bohlmark, A.P. Ehiasarian, J.T. Gudmundsson, Ionized physical vapor deposition (IPVD): A review of technology and applications, Thin Solid Films 513 (2006) 1–24.

[27] G. Greczynski, J. Lu, S. Bolz, W. Kölker, C. Schiffers, O. Lemmer, I. Petrov, J.E. Greene, L. Hultman, Novel strategy for low-temperature, high-rate growth of dense, hard, and stress-free refractory ceramic thin films, J. Vac. Sci. Technol. A 32 (2014) 0415151–04151512.

[28] J.E. Greene, Thin film nucleation, growth, and microstructural evolution: An atomic scale view, in: P.M. Martin (Ed.), Handbook of Deposition Technologies for Films and Coatings, 3rd ed., William Andrew Publishing, Oxford, 2010: pp. 554–620.

[29] J. Bøttiger, J. Chevallier, J.H. Petersen, N. Schell, W. Matz, A. Mücklich, Observation of the growth mode of TiN during magnetron sputtering using synchrotron radiation, J. Appl. Phys. 91 (2002) 5429–5433.

[30] P. Patsalas, S. Logothetidis, Interface properties and structural evolution of TiN/Si and TiN/GaN heterostructures, J. Appl. Phys. 93 (2003) 989–998.

[31] E.G. Bauer, B.W. Dodson, D.J. Ehrlich, L.C. Feldman, C.P. Flynn, M.W. Geis, J.P. Harbison, R.J. Matyi, P.S. Peercy, P.M. Petroff, J.M. Phillips, G.B. Stringfellow, A. Zangwill, Fundamental issues in heteroepitaxy—A Department of Energy, Council on Materials Science Panel Report, J. Mater. Res. 5 (1990) 852–894.

[32] International Centre for Diffraction Data, Powder Diffraction File 00-045-0946, 2007.

[33] International Centre for Diffraction Data, Powder Diffraction File 00-038-1420, 2007.

[34] International Centre for Diffraction Data, Powder Diffraction File 00-004-0836, 2007.

[35] S. Cazottes, Z.L. Zhang, R. Daniel, J.S. Chawla, D. Gall, G. Dehm, Structural characterization of a Cu/MgO(001) interface using C_S-corrected HRTEM, Thin Solid Films 519 (2010) 1662–1667.

[36] Z. Zhang, Y. Long, S. Cazottes, R. Daniel, C. Mitterer, G. Dehm, The peculiarity of the metal-ceramic interface, Sci. Rep. 5 (2015) 11460.

[37] P.B. Barna, M. Adamik, Fundamental structure forming phenomena of polycrystalline films and the structure zone models, Thin Solid Films 317 (1998) 27–33.

[38] J.A. Thornton, High rate thick film growth, Annu. Rev. Mater. Sci. 7 (1977) 239–260.

[39] A. Anders, A structure zone diagram including plasma-based deposition and ion etching, Thin Solid Films 518 (2010) 4087–4090.

[40] D.M. Mattox, Particle bombardment effects on thin-film deposition: A review, J. Vac. Sci. Technol. A 7 (1989) 1105–1114.

[41] S. Grasser, Influence of pulsed bias on CrN coatings prepared by reactive magnetron sputtering, Diploma thesis, Montanuniversität Leoben, 2008.

[42] L.E. Toth, Transition metal carbides and nitrides, Academic Press, New York, 1971.

[43] H. Okamoto, N-Ti (Nitrogen-Titanium), J. Phase Equilibria Diffus. 34 (2012) 151–152.

[44] J.-E. Sundgren, Structure and properties of TiN coatings, Thin Solid Films. 128 (1985) 21–44.

[45] J.-E. Sundgren, B.-O. Johansson, S.-E. Karlsson, H.T.G. Hentzell, Mechanisms of reactive sputtering of titanium nitride and titanium carbide II: Morphology and structure, Thin Solid Films 105 (1983) 367–384.

[46] J.-E. Sundgren, B.-O. Johansson, H.T.G. Hentzell, S.-E. Karlsson, Mechanisms of reactive sputtering of titanium nitride and titanium carbide III: Influence of substrate bias on composition and structure, Thin Solid Films 105 (1983) 385–393.

[47] J.-E. Sundgren, B.-O. Johansson, S.-E. Karlsson, Mechanisms of reactive sputtering of titanium nitride and titanium carbide I: Influence of process parameters on film composition, Thin Solid Films 105 (1983) 353–366.

[48] P. Patsalas, C. Charitidis, S. Logothetidis, The effect of substrate temperature and biasing on the mechanical properties and structure of sputtered titanium nitride thin films, Surf. Coat. Technol. 125 (2000) 335–340.

[49] H. Ljungcrantz, M. Odén, L. Hultman, J.E. Greene, J.-E. Sundgren, Nanoindentation studies of single-crystal (001)-, (011)-, and (111)-oriented TiN layers on MgO, J. Appl. Phys. 80 (1996) 6725–6733.

[50] C. Stampfl, W. Mannstadt, R. Asahi, A. Freeman, Electronic structure and physical properties of early transition metal mononitrides: Density-functional theory LDA, GGA, and screened-exchange LDA FLAPW calculations, Phys. Rev. B. 63 (2001) 1–11.

[51] B.O. Johansson, J.E. Sundgren, J.E. Greene, A. Rocket, S.A. Barnett, Growth and properties of single crystal TiN films deposited by reactive magnetron sputtering, J. Vac. Sci. Technol. A 3 (1985) 303–307.

[52] R.S. Ningthoujam, N.S. Gajbhiye, Synthesis, electron transport properties of transition metal nitrides and applications, Prog. Mater. Sci. 70 (2015) 50–154.

[53] W. Tsai, M. Delfino, J.A. Fair, D. Hodul, Temperature dependence of the electrical resistivity of reactively sputtered TiN films, J. Appl. Phys. 73 (1993) 4462–4467.

[54] N. Savvides, B. Window, Electrical transport, optical properties, and structure of TiN films synthesized by low-energy ion assisted deposition, J. Appl. Phys. 64 (1988) 225–234.

[55] M. Kawamura, Y. Abe, H. Yanagisawa, K. Sasaki, Characterization of TiN films prepared by a conventional magnetron sputtering system: Influence of nitrogen flow percentage and electrical properties, Thin Solid Films 287 (1996) 115–119.

[56] S. Niyomsoan, W. Grant, D.L. Olson, B. Mishra, Variation of color in titanium and zirconium nitride decorative thin films, Thin Solid Films 415 (2002) 187–194.

[57] A. Mumtaz, W.H. Class, Color of titanium nitride prepared by reactive dc magnetron sputtering, J. Vac. Sci. Technol. 20 (1982) 345–348.

[58] S.P. Murarka, Diffusion barriers in semiconductor devices/circuits, in: D. Gupta (Ed.), Diffusion Processes in Advanced Technological Materials, 1st ed., William Andrew Publishing, Norwich, NY, 2005: pp. 239–281.

[59] M.B. Chamberlain, Diffusion of copper in thin TiN films, Thin Solid Films 91 (1982) 155–162.

[60] M. Mändl, H. Hoffmann, P. Kücher, Diffusion barrier properties of Ti/TiN investigated by transmission electron microscopy, J. Appl. Phys. 68 (1990) 2127–2132.

[61] W. Sinke, G.P.A. Frijlink, F.W. Saris, Oxygen in titanium nitride diffusion barriers, Appl. Phys. Lett. 47 (1985) 471–473.

[62] J.O. Olowolafe, J. Li, J.W. Mayer, E.G. Colgan, Effects of oxygen in TiN_x on the diffusion of Cu in Cu/TiN/Al and Cu/TiN_x/Si structures, Appl. Phys. Lett. 58 (1991) 469–471.

[63] K.T. Nam, A. Datta, S.-H. Kim, K.-B. Kim, Improved diffusion barrier by stuffing the grain boundaries of TiN with a thin Al interlayer for Cu metallization, Appl. Phys. Lett. 79 (2001) 2549–2551.

[64] K.-C. Park, K.-B. Kim, Effect of annealing of titanium nitride on the diffusion barrier property in Cu metallization, J. Electrochem. Soc. 142 (1995) 3109–3115.

[65] W.-H. Lee, Y.-L. Kuo, H.-J. Huang, C. Lee, Effect of density on the diffusion barrier property of TiN_x films between Cu and Si, Mater. Chem. Phys. 85 (2004) 444–449.

[66] F. Krumeich, Properties of electrons, their interactions with matter and applications in electron microscopy, (2015). http://www.microscopy.ethz.ch/downloads/Interactions.pdf (accessed January 25, 2015).

[67] D.B. Williams, C.B. Carter, Transmission electron microscopy: A textbook for materials science, Springer Science+Business Media, New York, 2009.

[68] R.H. Wade, A brief look at imaging and contrast transfer, Ultramicroscopy. 46 (1992) 145–156.

[69] J. Palisaitis, Electron energy loss spectroscopy of III-nitride semiconductors, Licentiate thesis, Linköping University, 2011.

[70] O. Scherzer, The theoretical resolution limit of the electron microscope, J. Appl. Phys. 20 (1949) 20–29.

[71] W. Sigle, Analytical transmission electron microscopy, Annu. Rev. Mater. Res. 35 (2005) 239–314.

[72] D.J. Larson, T.J. Prosa, R.M. Ulfig, B.P. Geiser, T.F. Kelly, Local electrode atom probe tomography, Springer Science+Business Media, New York, 2013.

[73] B. Gault, M.P. Moody, J.M. Cairney, S.P. Ringer, Atom probe microscopy, Springer Science+Business Media, New York, 2012.

[74] H. Gnaser, Atom probe tomography of nanostructures, Surf. Interface Anal. 46 (2014) 383–388.

[75] T.F. Kelly, D.J. Larson, Atom probe tomography 2012, Annu. Rev. Mater. Res. 42 (2012) 1–31.

[76] E.A. Marquis, N.A. Yahya, D.J. Larson, M.K. Miller, R.I. Todd, Probing the improbable: Imaging C atoms in alumina, Mater. Today. 13 (2010) 34–36.

[77] G. Sha, S.P. Ringer, Effect of laser pulsing on the composition measurement of an Al–Mg–Si–Cu alloy using three-dimensional atom probe, Ultramicroscopy 109 (2009) 580–584.

[78] P. Bas, A. Bostel, B. Deconihout, D. Blavette, A general protocol for the reconstruction of 3D atom probe data, Appl. Surf. Sci. 87-88 (1995) 298–304.

[79] B. Geiser, D. Larson, E. Oltman, S. Gerstl, D. Reinhard, T. Kelly, T. Prosa, Wide-field-of-view atom probe reconstruction, Microsc. Microanal. 15 (2009) 292–293.

[80] D.J. Larson, T.J. Prosa, B.P. Geiser, W.F. Egelhoff, Effect of analysis direction on the measurement of interfacial mixing in thin metal layers with atom probe tomography, Ultramicroscopy 111 (2011) 506–511.

[81] E.A. Marquis, B.P. Geiser, T.J. Prosa, D.J. Larson, Evolution of tip shape during field evaporation of complex multilayer structures, J. Microsc. 241 (2011) 225–33.

[82] D.J. Larson, B.P. Geiser, T.J. Prosa, S.S.A. Gerstl, D.A. Reinhard, T.F. Kelly, Improvements in planar feature reconstructions in atom probe tomography, J. Microsc. 243 (2011) 15–30.

[83] L.J.S. Johnson, M. Thuvander, K. Stiller, M. Odén, L. Hultman, Spinodal decomposition of $Ti_{0.33}Al_{0.67}N$ thin films studied by atom probe tomography, Thin Solid Films 520 (2012) 4362–4368.

[84] R. Rachbauer, S. Massl, E. Stergar, D. Holec, D. Kiener, J. Keckes, J. Patscheider, M. Stiefel, H. Leitner, P.H. Mayrhofer, Decomposition pathways in age hardening of Ti-Al-N films, J. Appl. Phys. 110 (2011) 0235151–02351510.

[85] R. Rachbauer, E. Stergar, S. Massl, M. Moser, P.H. Mayrhofer, Three-dimensional atom probe investigations of Ti–Al–N thin films, Scr. Mater. 61 (2009) 725–728.

[86] T.F. Kelly, D.J. Larson, K. Thompson, R.L. Alvis, J.H. Bunton, J.D. Olson, B.P. Gorman, Atom probe tomography of electronic materials, Annu. Rev. Mater. Res. 37 (2007) 681–727.

[87] D.R. Baer, S. Thevuthasan, Characterization of thin films and coatings, in: P.M. Martin (Ed.), Handbook of Deposition Technologies for Films and Coatings, 3rd ed., William Andrew Publishing, Oxford, 2010: pp. 749–864.

[88] M. Birkholz, Thin Film Analysis by X-Ray Scattering, WILEY-VCH Verlag GmbH & Co. KGaA, Weinheim, 2006.

[89] A. Aijaz, PVD: Thin film growth by magnetron sputtering and basic plasma and film characterization - Thin Film Physics lab compendium, Linköping University, 2010.

[90] Z. Zhang, L.M. Wong, H.G. Ong, X.J. Wang, J.L. Wang, S.J. Wang, H. Chen, T. Wu, Self-assembled shape- and orientation-controlled synthesis of nanoscale Cu_3Si triangles, squares, and wires., Nano Lett. 8 (2008) 3205–10.

[91] J.K. Solberg, The crystal structure of η-Cu_3Si precipitates in silicon, Acta Crystallogr. Sect. A. 34 (1978) 684–698.

[92] J. Sommer, C. Herzig, Direct determination of grain-boundary and dislocation self-diffusion coefficients in silver from experiments in type-C kinetics, J. Appl. Phys. 72 (1992) 2758.

[93] S.H. Hsieh, C.M. Chien, W.L. Liu, W.J. Chen, Failure behavior of ITO diffusion barrier between electroplating Cu and Si substrate annealed in a low vacuum, Appl. Surf. Sci. 255 (2009) 7357–7360.

[94] J.T. No, J.H. O, C. Lee, Evaluation of Ti-Si-N as a diffusion barrier between copper and silicon, Mater. Chem. Phys. 63 (2000) 44–49.

[95] Y. Wang, C. Zhao, Z. Song, F. Cao, D. Yang, Effect of substrate bias voltages on the diffusion barrier properties of Zr-N films in Cu metallization, Appl. Surf. Sci. 253 (2007) 8858–8862.

[96] K.-L. Ou, M.-H. Tsai, H.-M. Huang, S.-Y. Chiou, C.-T. Lin, S.-Y. Lee, Interfacial reactions and electrical properties of hafnium-based thin films in Cu/barrier/n^+–p junction diodes, Microelectron. Eng. 77 (2005) 184–192.

[97] Y.M. Zhou, M.Z. He, Z. Xie, Diffusion barrier performance of novel Ti/TaN double layers for Cu metallization, Appl. Surf. Sci. 315 (2014) 353–359.

[98] S.-H. Kim, K.T. Nam, A. Datta, K. Kim, Failure mechanism of a multilayer (TiN/Al/TiN) diffusion barrier between copper and silicon, J. Appl. Phys. 92 (2002) 5512.

[99] Y.-L. Kuo, J.-J. Huang, S.-T. Lin, C. Lee, W.-H. Lee, Diffusion barrier properties of sputtered TaN_x between Cu and Si using TaN as the target, Mater. Chem. Phys. 80 (2003) 690–695.

[100] J. Chan, Four-point probe manual, University of California, Berkeley, EECS Web Site. (1994). http://www-inst.eecs.berkeley.edu/~ee143/fa10/lab/four_point_probe.pdf (accessed October 7, 2015).

[101] D.M. Mattox, Non-elemental characterization of films and coatings, in: P.M. Martin (Ed.), Handbook of Deposition Technologies for Films and Coatings, 3rd ed., William Andrew Publishing, Oxford, 2010: pp. 716–748.

[102] S.S. Cohen, Contact resistance and methods for its determination, Thin Solid Films 104 (1983) 361–379.

CHAPTER 2

EXPERIMENTAL AND NUMERICAL DETAILS

2.1 FUNDAMENTAL INTERDIFFUSION STUDIES

TiN/Cu bilayer stacks discussed in the subsequent chapters 3 and 4 are deposited in a laboratory-scale magnetron sputtering system shown in Fig. 17 on polished single-crystal (001)-oriented MgO substrates ($10\times10\times0.5$ mm^3) and polished (001)-oriented Si wafers ($20\times6\times0.5$ mm^3) with a 5 nm thick thermal SiO_2 layer. This amorphous SiO_2 layer prevents the diffusion of Si from the substrate into the TiN layer at elevated temperatures during the deposition process. The substrates are cleaned by successive rinses in ultrasonic baths of acetone and ethanol before being mounted on a rotating substrate holder in the deposition chamber, which has a base pressure below 10^{-5} mbar. The deposition system is equipped with three independent magnetron sputtering sources. The target-to-substrate distance is 80 mm and the targets are tilted at an angle of 13° with respect to the substrate normal. All targets are sputter-cleaned in pure Ar for 5 min, with a shutter shielding the substrates. Additionally, the substrates are

Figure 17: Laboratory-scale magnetron sputtering system “Josefine II” used to synthesize the TiN/Cu layer stacks discussed in chapters 3 and 4.

etched for 5 min in an Ar plasma immediately prior to deposition by applying a bias voltage of -500 V to activate and clean the surface. TiN layers are grown reactively in mixed Ar/N_2 atmosphere (35 sccm Ar, 5 sccm N_2) at a substrate temperature of 700 °C and a pressure of 4.5×10^{-3} mbar. During deposition, two 2 inch diameter Ti (99.995% pure) targets are operated in magnetically unbalanced direct current mode with a power density of 6.2 W cm^{-2}. Using these conditions, a deposition rate of 11 nm min^{-1} is achieved for TiN grown onto substrates at an asymmetrically pulsed bias potential of -100 V. Subsequently, the samples are cooled down for 1 h inside the vacuum chamber until a substrate temperature of 50 °C is reached. To remove possible impurities that might have adsorbed during this cooling step, the TiN surface is cleaned again for 1 min by Ar ion etching with a bias voltage of -500 V. The Cu top layer is then deposited in a pure Ar discharge at a pressure of 4.6×10^{-3} mbar. The power density at the single 2 inch diameter Cu (99.99% pure) target operated in magnetically unbalanced direct current mode is set to 2.1 W cm^{-2}. The Cu deposition is carried out at floating potential with a film growth rate of 13 nm min^{-1}.

Three sets of bilayers with different layer thicknesses as measured in cross-sectional TEM are discussed in chapter 3: TiN (160 nm) / Cu (20 nm), TiN (100 nm) / Cu (130 nm), and TiN (80 nm) / Cu (130 nm). The samples with the thicker Cu film are used in the subsequent annealing studies, where Cu acts as the diffusion source. Isothermal annealing treatments are performed in vacuum (base pressure < 10^{-6} mbar) for 1 h at 900 °C, and in Ar atmosphere for 12 h at 1000 °C. The choice of a protective gas atmosphere for the high temperature annealing treatment is necessary to prohibit Cu evaporation. It has to be noted that during the annealing treatments de-wetting of the Cu layer and consequently Cu island formation is observed. In the following investigations, the Cu diffusion into TiN is studied directly beneath the center of such Cu islands, to ensure that a sufficient amount of diffusing species was available.

In chapter 4, two additional batches of TiN/Cu stacks with different layer thicknesses are discussed: TiN (100 nm) / Cu (130 nm) and TiN (180 nm) / Cu (130 nm). To obtain distinct diffusion profiles of Cu in TiN, the samples with the thicker TiN layer are subjected to isothermal annealing treatments at 900 °C for 1 h in an HTM Reetz vacuum furnace at a pressure below 10^{-6} mbar. The annealing program comprises a ramp-up step with a heating rate of 30 K/min, an isothermal annealing step lasting 1 h, and a cooling step at a system dependent cooling rate.

Crystal structures of the pristine samples are characterized by XRD measurements with a Bruker-AXS D8 Advance diffractometer. The used Cu-K_α radiation is parallelized in a Goebel mirror and recorded with an energy-dispersive SolX detector with a 0.12° slit via scans in $\theta/2\theta$ and grazing incidence (2° incidence angle) mode. Pole figure measurements are performed using a Rigaku SmartLab 5-axis diffractometer also equipped with Cu-K_α radiation, a parabolic multilayer mirror in the primary beam and a secondary graphite monochromator in 5° steps for the azimuth angle Ψ, $0° \leq \Psi \leq 85°$ and the polar angle Φ, $0° \leq \Phi \leq 360°$. The data is evaluated using the MATLAB® toolbox MTEX 3.5.0 for quantitative texture analysis [1]. Single-layer TiN films deposited with the same parameters as the bilayer films are used to determine the density and surface roughness of the TiN film by XRR measurements and to study the TiN surface by electron backscatter diffraction (EBSD) and atomic force microscopy (AFM). XRR characterization is performed using the Rigaku system in the same setup as for the pole-figure analysis. For the fitting of the measured data the Leptos Bruker software is used. Values for the density and surface roughness of the TiN layer are obtained by fitting the critical angle and the intensity slope according to the Nevot-Croce interface model with a genetic algorithm fit [2,3]. EBSD scans are performed with an EDAX DigiView IV EBSD detector inside a SEM. Areas of 10x10 μm^2 are scanned with the pixel size set to 30 nm^2. The surface roughness of the as-deposited TiN layer is also measured by AFM in tapping mode in ambient atmosphere with a BRR/SPM device designed by DME.

Elemental composition of the TiN film deposited on MgO is obtained by time-of-flight energy elastic recoil detection analysis (ToF-E ERDA) provided by the Tandem Laboratory at Uppsala University. 36 MeV $^{127}I^{8+}$ ions are used as projectiles with the incidence angle set to 67.5° with respect to the surface normal and a recoil angle of 45° [4]. The recoil ToF-E ERDA spectra are analyzed using the CONTES code [5], where the measured recoil energy spectrum of each element is converted to relative atomic concentration, providing an error margin of ±1.5 at.% for the reported elemental compositions.

To investigate the TiN/Cu interface region in pristine and annealed samples with APT and cross-sectional TEM, samples are prepared site-specifically [6] using the FIB lift-out technique in a Zeiss Auriga SMT SEM equipped with an Orsay Physics Cobra Z-05 FIB unit with a Ga^+ ion source. In a final step all samples are polished with 5 kV Ga^+ ions to remove surface defects. Additional TEM samples are prepared by the conventional method, where specimens glued into a Ti grid are mechanically polished down to a thickness of approximately 60 µm. Etching of the samples is completed in a Gatan precision ion polishing system by bombardment with 5 keV Ar^+ ions until electron transparency is reached. Fine polishing is performed in the same system using 2 keV Ar^+ ions.

HRTEM, collection of selected area diffraction (SAED) patterns and STEM are carried out by using a FEI Tecnai G^2 TF20 UT TEM with a field emission gun operated at 200 kV. The instrument has a point resolution of 0.19 nm and is equipped with an EDX system. EDX analyses are performed during STEM investigations to obtain elemental composition maps across the interfaces. Furthermore, *Z*-contrast STEM imaging with a HAADF detector is employed to detect electrons elastically scattered from the specimen with high angles, thus providing strong atomic number contrast in the image.

Atom probe data collection is executed in an Imago LEAP 3000X HR local electrode atom probe operated in laser (532 nm wavelength) pulsing mode. The base pressure in the analysis chamber is below 5×10^{-11} mbar. While all investigated specimens have a similar geometry with a tip radius smaller than 50 nm and a shank angle around 10°, it is found that two different parameter sets are needed to optimize measurement conditions for the two substrate materials, MgO and Si/SiO_2. The parameters are chosen to maximize the signal-to-noise ratio and avoid pronounced thermal tails in the recorded mass spectra. In case of bilayers grown on MgO, a pulse rate of 200 kHz and pulse energy of 0.2 nJ at a specimen base temperature of 60 K yields the highest spectral quality. Samples deposited on Si/SiO_2 are analyzed with pulse energy of 0.1 nJ and a repetition rate of 200 kHz at 40 K. The three-dimensional reconstruction of the tips is performed with the Cameca IVAS 3.6.6 software based on the tip radius evolution with increasing evaporation voltage. Input parameters are an evaporation field of 30 V nm^{-1}, image compression factor of 1.65 and field factor of 3.3.

First-principles calculations presented in chapter 4 and provided by the Materials Center Leoben GmbH are based on DFT employing the generalized-gradient approximation with the PBEsol exchange-correlation functional [7] and are performed with the Vienna *ab initio* simulation package [8,9]. Ion-electron interactions are described by means of the projector augmented wave method [10], with a plane-wave energy cutoff of 400 eV. For all calculations, a 3×3×3 supercell of TiN is used, consisting of 216 atoms for a defect-free cell. A Monkhorst-Pack *k*-point mesh [11] of 4×4×4 is used for Brillouin zone sampling with a Methfessel-Paxton [12] smearing of 0.2 eV. This *k*-point mesh ensures the convergence of the migration barriers within 10 meV. The calculations are performed with two different lattice constants: *i)* 4.212 Å (corresponding to the equilibrium lattice parameter at 0 K) and *ii)* 4.278 Å (corresponding to the experimental value at 1273 K [13]). Migration barriers are calculated using the nudged elastic band method (NEB) [14] with three intermediate images. For selected cases, the convergence of the minimum-energy pathway is tested by comparing NEB calculations with three and seven intermediate images. The resulting heights of the migration barriers are found to agree within the numerical accuracy, suggesting that three intermediate images are sufficient for the present investigations. The equilibrium defect concentrations are predicted by the dilute-solution model (DSM) [15,16] as a function of the TiN composition.

2.2 DEGRADATION AND OPTIMIZATION OF DIFFUSION BARRIERS

TiN/Cu bilayer stacks discussed in chapter 5 are grown in a CC800/9 CemeCon industrial-scale deposition system shown in Fig. 18 by conventional DC magnetron sputtering, using Ti and Cu targets (8.8×50 cm^2). Si(001) substrates (2×1 cm^2) with a native SiO_2 layer are cleaned in ultrasonic baths of acetone and isopropyl alcohol. Cleaned substrates are mounted in the deposition chamber symmetrically with respect to the targets at a target-to-substrate distance of 18 cm. The system is evacuated to a base pressure below 3×10^{-5} mbar. Prior to deposition, the targets are sputter cleaned behind closed shutters in pure Ar for 1 min. Depositions are carried out without external substrate heating. During the TiN deposition the Ar flow is set to 350 sccm, while the N_2 flow is regulated automatically by a feedback loop to maintain a constant deposition pressure of 4.2×10^{-3} mbar. The Ti magnetron is operated at 6 kW and a negative bias potential of 100 V is applied to the Si substrates, resulting in a deposition rate of

Figure 18: Industrial-scale CemeCon magnetron sputtering system “Samson” used to synthesize the TiN/Cu and TiTaN/Cu layer stacks discussed in chapters 5 and 6, respectively.

28 nm min^{-1} for TiN. Subsequently, the Cu layer is deposited without breaking the vacuum at a magnetron power of 2 kW and a negative bias potential of 100 V, yielding a deposition rate of 150 nm min^{-1}. The Ar flow rate is increased to 440 sccm to maintain a pressure of 4.2×10^{-3} mbar during the Cu deposition. The pristine Cu and TiN layers are 600 and 420 nm thick, respectively. These chosen layer thicknesses are higher than for diffusion barriers employed in actual industrial microelectronic devices. This is intentional, since it allows for more accurate EDX profiling and imaging of defects, while the diffusion mechanisms remain the same as on the smaller scale.

TiN/Cu and $Ti_{0.84}Ta_{0.16}N$/Cu bilayer stacks discussed in chapter 6 are deposited on Si(001) substrates in the same CC800/9 CemeCon magnetron sputtering system (Fig. 18) outfitted with cast rectangular 8.8×50 cm^2 Ti, Ta, and Cu targets. The exact setup inside the deposition chamber is described in detail in Ref. [17]. For the deposition of the TiN/Cu layers, the system is evacuated to a base pressure of 2.3×10^{-5} mbar. The process proceeds as detailed above with the exception that during the TiN deposition, the Si substrates are electrically floating, resulting in a deposition rate of 33 nm min^{-1} for TiN. The pristine Cu and TiN layers are 160 and 200 nm thick, respectively.

For the deposition of the $Ti_{0.84}Ta_{0.16}N$/Cu layers, the system is evacuated to a base pressure of 0.4×10^{-5} mbar. Settings regarding sputter cleaning of targets, gas flow, and deposition pressure are the same as for the TiN/Cu stack. The Ti magnetron is run in conventional direct current magnetron sputtering (DCMS) mode with a constant power of 6 kW. The Ta magnetron is operated in high-power impulse magnetron sputtering (HIPIMS) mode with an average power of 1.5 kW at a fixed pulsing frequency of 100 Hz (2% duty cycle). A negative, pulsed substrate bias of 60 V is applied at an offset time of 80 µs after HIPIMS pulse initiation, thus synchronously with the 200 µs long metal-ion-rich portion of each HIPIMS pulse. This results in a deposition rate of 34 nm min^{-1} for the $Ti_{0.84}Ta_{0.16}N$ film. The subsequent Cu deposition proceeds as described for the TiN/Cu stack. Pristine Cu and $Ti_{0.84}Ta_{0.16}N$ layers are 160 and 150 nm thick, respectively.

To induce interdiffusion between the layers, samples are subjected to isothermal annealing treatments in an HTM-Reetz vacuum annealing furnace with a base pressure in the order of 10^{-7} mbar. The annealing process comprises a ramp-up step with a heating rate of 30 K/min, the isothermal annealing itself at temperatures of 600, 700, 800, and 900 °C with a holding time of 1 h, and a cooling phase at a system-dependent cooling rate.

The average surface roughness R_a of the pristine Cu top layers is determined with a Wyko NT 1000 optical 3D white light profiling system on sample areas of 0.5×0.5 mm^2. Pristine and annealed samples are characterized by XRD measurements in the Bruker-AXS D8 Advance diffractometer described above. The diffractograms are recorded with an energy-dispersive SolX detector with a

0.12° slit via scans in grazing incidence (2° incidence angle) mode. Sheet resistivity measurements of the Cu top layer are carried out under the assumption of a constant pristine Cu film thickness on three different spots on each sample with a linear-array Jandel FPP with the output current set to 9.990 mA DC. The resistivity ρ is calculated according to equation (14).

A Zeiss Auriga SMT SEM with a SE and a BSE detector is used to obtain plan-view images of the sample surfaces before and after the annealing treatments. In addition, some specimen cross-sections are prepared in the same instrument by FIB cutting with an Orsay Physics Cobra Z-05 FIB unit fitted with a Ga^+ ion source. Before further analysis, all cross-sections are fine-polished with a 5 kV Ga^+ beam to remove surface defects due to Ga^+ implantation. Cross-sectional EDX profiles are then obtained with an EDAX Apollo 40+ EDX detector with an energy resolution of 120 eV.

TEM and APT samples are prepared and investigated in the same systems as described above. Specimens discussed in chapter 5 are measured in APT with a pulse energy of 0.2 nJ and a repetition rate of 200 kHz at 30 K. The three-dimensional reconstruction of the tips is performed with the Cameca IVAS 3.6.6 software based on the shank evolution as determined from SEM micrographs. Input parameters are an evaporation field of 30 V nm^{-1}, image compression factor of 1.65 and field factor of 3.3. Results for the analyzed tips are consistent.

References

[1] F. Bachmann, R. Hielscher, H. Schaeben, Texture analysis with MTEX – Free and open source software toolbox, Solid State Phenom. 160 (2010) 63–68.

[2] L. Névot, P. Croce, Caractérisation des surfaces par réflexion rasante de rayons X. Application à l'étude du polissage de quelques verres silicates, Rev. Phys. Appliquée 15 (1980) 761–779.

[3] A. Ulyanenkov, Novel methods and universal software for HRXRD, XRR and GISAXS data interpretation, Appl. Surf. Sci. 253 (2006) 106–111.

[4] J. Jensen, D. Martin, A. Surpi, T. Kubart, ERD analysis and modification of TiO_2 thin films with heavy ions, Nucl. Instrum. Meth. B 268 (2010) 1893–1898.

[5] M.S. Janson, CONTES, Conversion of time-energy spectra, a program for ERDA data analysis, Internal Report, Uppsala University. (2004).

[6] K. Thompson, D. Lawrence, D.J. Larson, J.D. Olson, T.F. Kelly, B. Gorman, In situ site-specific specimen preparation for atom probe tomography, Ultramicroscopy 107 (2007) 131–139.

[7] J.P. Perdew, A. Ruzsinszky, G.I. Csonka, O.A. Vydrov, G.E. Scuseria, L.A. Constantin, X. Zhou, K. Burke, Restoring the density-gradient expansion for exchange in solids and surfaces, Phys. Rev. Lett. 100 (2008) 136406.

[8] G. Kresse, J. Furthmüller, Efficiency of ab-initio total energy calculations for metals and semiconductors using a plane-wave basis set, Comput. Mater. Sci. 6 (1996) 15–50.

[9] G. Kresse, J. Furthmüller, Efficient iterative schemes for ab initio total-energy calculations using a plane-wave basis set, Phys. Rev. B 54 (1996) 11169–11186.

[10] P.E. Blöchl, Projector augmented-wave method, Phys. Rev. B 50 (1994) 17953–17979.

[11] H.J. Monkhorst, J.D. Pack, Special points for Brillouin-zon integrations, Phys. Rev. B 13 (1976) 5188–5192.

[12] M. Methfessel, A.T. Paxton, High-precision sampling for Brillouin-zone integration in metals, Phys. Rev. B 40 (1989) 3616–3621.

[13] K. Aigner, W. Lengauer, D. Rafaja, P. Ettmayer, Lattice parameters and thermal expansion of $Ti(C_xN_{1-x})$, $Zr(C_xN_{1-x})$, $Hf(C_xN_{1-x})$ and TiN_{1-x} from 298 to 1473 K as investigated by high-temperature X-ray diffraction, J. Alloys Compd. 215 (1994) 121–126.

[14] D. Sheppard, R. Terrell, G. Henkelman, Optimization methods for finding minimum energy paths, J. Chem. Phys. 128 (2008) 134106.

[15] C. Woodward, M. Asta, G. Kresse, J. Hafner, Density of constitutional and thermal point defects in $L1_2$ Al_3Sc. Phys. Rev. B 63 (2001) 094103.

[16] H. Ding, B. Medasani, W. Chen, K.A. Persson, M. Haranczyk, M. Asta, PyDII: A python framework for computing equilibrium intrinsic point defect concentrations and extrinsic solute site preferences in intermetallic compounds, Comput. Phys. Commun. 193 (2015) 118–123.

[17] G. Greczynski, J. Lu, S. Bolz, W. Kölker, C. Schiffers, O. Lemmer, I. Petrov, J.E. Greene, L. Hultman, Novel strategy for low-temperature, high-rate growth of dense, hard, and stress-free refractory ceramic thin films, J. Vac. Sci. Technol. A 32 (2014) 0415151–04151512.

CHAPTER 3

Cu DIFFUSION INTO SINGLE-CRYSTAL TiN

3.1 FUNDAMENTALS

Diffusion barriers are employed in microelectronic devices to prohibit the migration of atoms from the Cu- or Al-based interconnects to adjacent dielectric and semiconductor regions during fabrication and operation. Sputter-deposited TiN barrier layers in Cu metallization schemes have been widely studied because of their high thermal (melting point T_m = 2930 °C) and structural stability combined with a low electrical resistivity (20-197 μΩ cm) [1–3]; thus meeting all the requirements for application in miniaturized electronic devices.

In an early experimental investigation, Chamberlain [4] reported Cu diffusion into r.f. sputtered TiN films with an activation energy $E_a = 4.4$ eV, which was attributed to grain boundary diffusion. More recent studies have looked into the correlation between the barrier performance and microstructure of TiN films. For example, Moriyama *et al.* [5] found that polycrystalline TiN films with small mosaic-spread angles and large grain sizes are generally favorable, because the overall amount of grain boundary phase in these films is low. They measured the activation energy for grain boundary and lattice diffusion of Cu to be 1.4 and 2.7 eV, respectively. For nanocrystalline (average grain size around 8 nm) TiN barriers grown by pulsed laser deposition, Gupta *et al.* [6] observed significantly less Cu diffusion than for comparable polycrystalline and single-crystal TiN films. An explanation for this behavior could be the effectively much longer diffusion paths along grain boundaries in the case of nano-sized grains. In comparison, columnar grain structures or low angle grain boundaries provide direct diffusion paths in polycrystalline and single-crystal layers, respectively.

Improved TiN barrier performance was also observed in films with oxidized grain boundaries [7–10]. This mechanism works well for Al metallization by the stuffing of grain boundaries with Al oxides. However, it is not as effective in Cu metallization because the formation of Cu oxides in the TiN grain boundaries is thermodynamically less favorable [10,11].

While Cu diffusion in TiN barriers has been extensively studied from a phenomenological point of view, especially in the case of lattice diffusion, there is a lack of literature reporting experimental investigations of the underlying atomic migration mechanisms. This may be partly due to the fact that during the early stages of lattice diffusion the diffusion length is so small and the concentration of the diffusing species so low, that it is often below the detection threshold of conventional techniques for chemical analyses. Furthermore, theoretical studies of bulk TiN suggest that point defects present in the TiN barrier layer strongly affect the migration of impurity atoms [12–16]. TiN retains its stable rock salt structure for a wide stoichiometry range, often resulting in high numbers of native point defects such as vacancies or interstitials that interact with impurity species. For example impurities like O, C, H and Ar can be trapped at N vacancy sites in TiN and may be released again due to interactions with N interstitials. In the cases of C or Ar this results in the formation of stable defect complexes, while O and H are untrapped and released back into the host crystal. This release of O can also explain its segregation to grain boundaries and the subsequent stuffing observed in polycrystalline TiN [16]. Similar interactions with native point defects have been proposed by first-principles calculations for Cu atoms in TiN [13,15].

These point defects are hard to capture accurately by experiment. The two established characterization instruments used today are TEM in conjunction with EDX and electron energy loss spectrometry for structural analysis and compositional/chemical mapping as well as secondary ion mass spectrometry for chemical depth profiling. However, none of these techniques offers true 3D characterization at the atomic scale [17,18].

With the emergence and development of APT in the last decades this gap can now be closed. APT yields a discrete 3D compositional image with very high analytical sensitivity (as good as 1 atom per million) and a spatial resolution of 0.2-0.3 nm in all directions. All elements can be detected with an equally high efficiency without prior knowledge of the specimen's composition [17,18]. There are already several reports where APT has been used effectively for the characterization of materials and processes in semiconductor devices and advanced metallization [17,19–21].

The aim of the investigations summarized in this chapter is to combine various TEM techniques with APT in order to present a sophisticated and comprehensive analysis approach for the nanometer scale characterization of the interface and inter-diffusion processes in the Cu/bulk TiN system. The present chapter shows how the two complementary methods can be used to provide both structural and chemical information of high resolution at buried interfaces. Experimental findings are correlated with results of first-principles studies [12–16]. Ultimately, this information will on the one hand contribute to the understanding of complex segregation and diffusion phenomena; on the other hand this combined experimental approach could become the basis for innovations in materials for microelectronics such as ultrathin and highly effective diffusion and oxidation barrier layers, or - more generally - reliable and degradation-resistant layered materials.

3.2 STRUCTURAL AND COMPOSITIONAL CHARACTERIZATION

Fig. 19 shows XRD pole figure maps of a TiN (160 nm thickness) / Cu (20 nm thickness) bilayer grown on MgO(001). The pole figures were measured at constant 2 theta angles corresponding to the (111) and (200) reflections of TiN and Cu. At this point it has to be noted that because of the lattice mismatch of only -0.7% [19,20] between TiN and MgO their reflections nearly overlap. Due to the small film thicknesses, the substrate will partly contribute to the measured TiN pole figures. Nevertheless, in the 002-pole figures of both layers (Figs. 19 (a,c)) there are no maxima present apart from the single one at the origin. This indicates that all (001) planes in the TiN and the Cu film are oriented parallel to the substrate surface. The weak maximum in the center of the Cu 111-pole figure (Fig. 19 (d)) results from the (200) reflection of MgO (and possibly TiN), whose 2 theta angle of 42.917° [22] (TiN: 42.597° [23]) is very close to that of the Cu (111) reflection at 43.298° [24]. On the other hand, in both 111-pole figures (Figs. 19 (b,d)) four symmetric maxima at a tilt angle of about 55° can be observed. In cubic materials the angle between the (001) and (111) planes is 54.7°, again suggesting that TiN/Cu bilayers grow with their (001) planes parallel to the MgO (001) planes. Additionally, the maxima corresponding to the {111} planes of TiN and Cu appear at polar angles of 45, 135, 225 and 315°. Therefore, it can be concluded that the bilayers grow with a cube-on-cube epitaxial relationship on the substrate, i.e. {001}<010>TiN/Cu || {001}<010>MgO.

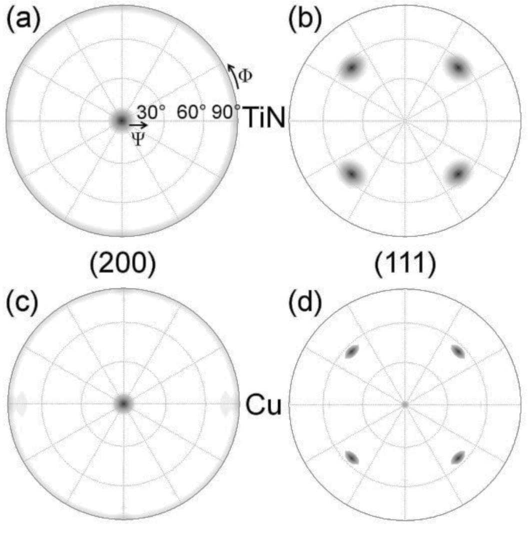

Figure 19: XRD pole figures obtained from the respective (a,c) (200) and (b,d) (111) reflections of TiN (160 nm) / Cu (20 nm) bilayers grown on (001)-oriented MgO substrates.

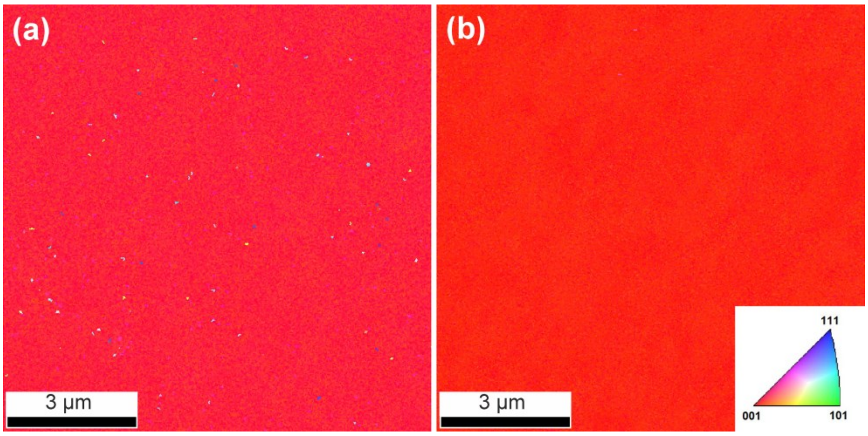

Figure 20: Plan-view EBSD maps of the (a) TiN and (b) Cu surface, recorded over an area of 10 × 10 µm^2 with a pixel size of 30 nm^2. The TiN and Cu layers were 160 and 20 nm thick, respectively.

Fig. 20 shows plan-view EBSD scans of the TiN and Cu surfaces. In the case of TiN some pixels give diffraction information deviating from the expected (001) orientation. These are most likely pixel errors due to debris on the surface and not actual growth defects. Otherwise the misorientation would carry on into the Cu top layer, which is not the case as can be seen in Fig. 20 (b). Thus, the EBSD scans further point to the epitaxial, single-crystalline growth of fcc TiN/Cu bilayers on (001)-oriented MgO.

The average surface roughness of the TiN layer is measured to be below 0.8 nm by AFM, which is in the range of the surface roughness of the substrate. A fit of the XRR curve of the TiN layer yields a comparable roughness value of 0.9 ± 0.2 nm.

Cross-sectional samples of the as-deposited and annealed bilayers are investigated by conventional TEM. In both cases the observable region of the TiN layer is free of grain boundaries, indicating that the film is single-crystalline. HRTEM micrographs (Figs. 21 (a,b)) and the corresponding SAED patterns (inserts in Figs. 21 (a,b)) of both the TiN/MgO and Cu/TiN interfaces in the as-deposited state are recorded along the [100] zone axis. In Fig. 21 (a) the (020) lattice spacings of MgO and TiN are both measured to be 0.21 nm. Because of the small lattice mismatch there is an overlap in the SAED patterns, which confirm the epitaxial relationship found by the pole figure maps. No indication of Mg-Ti-spinel formation at the interface, as previously reported in [25], can be detected during the TEM investigations or in the SAED patterns. The measured (020) lattice spacing of 0.18 nm in Cu (Fig. 21 (b)) goes along with clearly discernible reflections in the corresponding SAED pattern of the Cu/TiN interface, again confirming epitaxial, single-crystalline film growth.

Fig. 21 (c) shows a HRTEM micrograph of the TiN/MgO interface after annealing for 12 h at 1000 °C in Ar atmosphere. The TiN layer remains stable up to this temperature and no reaction with the MgO substrate is observed. Since

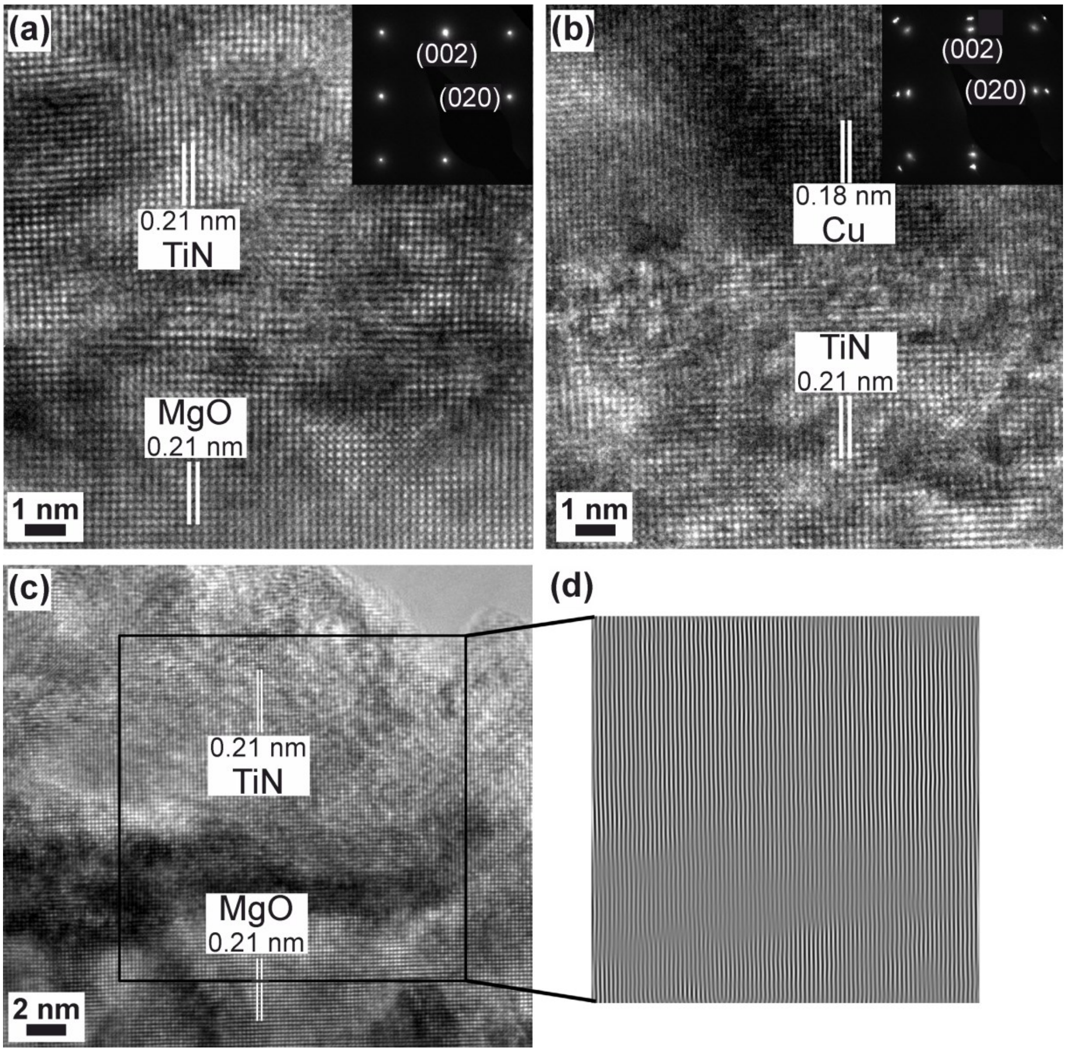

Figure 21: Cross-sectional HRTEM images of the (a) TiN/MgO and (b) Cu/TiN interface in the as-deposited state and corresponding SAED patterns (inserts) recorded along the [100] zone axis. The TiN and Cu layers were 160 and 20 nm thick, respectively. A high resolution micrograph of the TiN/MgO interface after annealing at 1000 °C for 12 h recorded along the [100] zone axis is shown in (c) as well as the corresponding calculated (020) Bragg image in (d).

there is a considerable difference in the thermal expansion coefficients of TiN and MgO, the compressive stress due to differential thermal contraction after cooling down the sample from the deposition temperature of 700 °C is calculated to be 2.2 GPa in the TiN film [26]. It can be assumed that at least a part of that stress is relieved by the formation of dislocations. Thus, annealing the film above the deposition temperature again will lead to a significant decrease in dislocation density. This is corroborated by the (020) Bragg image of the annealed TiN layer (Fig. 21 (d)), where no dislocations can be found in the layer. However, there are some misfit dislocations present directly at the interface, which is revealed by a darker contrast in the Bragg image. Overall, the low dislocation density and the lack of direct diffusion paths such as grain boundaries potentially enhance the performance of the single-crystal TiN diffusion barrier.

3.3 DIFFUSION STUDIES

3.3.1 Experimental Findings

The diffusion depth of Cu in the annealed samples is evaluated by STEM *Z*-contrast imaging techniques [27] and EDX mappings. After annealing at 900 °C for 1 h in vacuum, no perceptible Cu diffusion into bulk TiN is detected. A STEM image obtained with a HAADF detector is shown in Figs. 22 (a,b). Cu as the heaviest element gives the brightest contrast while MgO appears darkest. Figs. 22 (c,d) show EDX mappings of the Cu-K and the Ti-K edge recorded across the Cu/TiN interface with the pixel size set to 1 nm^2. In both the STEM image and the EDX mappings, the Cu/TiN interface appears sharp and well defined in terms of elemental distribution and no indications of Cu diffusion can be found over the investigated area.

Results for the sample annealed at 1000 °C for 12 h in Ar atmosphere are shown in Figs. 22 (e-h). The STEM *Z*-contrast image (Figs. 22 (e,f)) reveals a layer with lighter contrast reaching from the Cu/TiN interface into the TiN film. EDX mappings (Figs. 22 (g,h)) suggest that this layer is due to Cu diffusion into the bulk TiN. While the interface appears relatively sharp when mapping the Ti-K

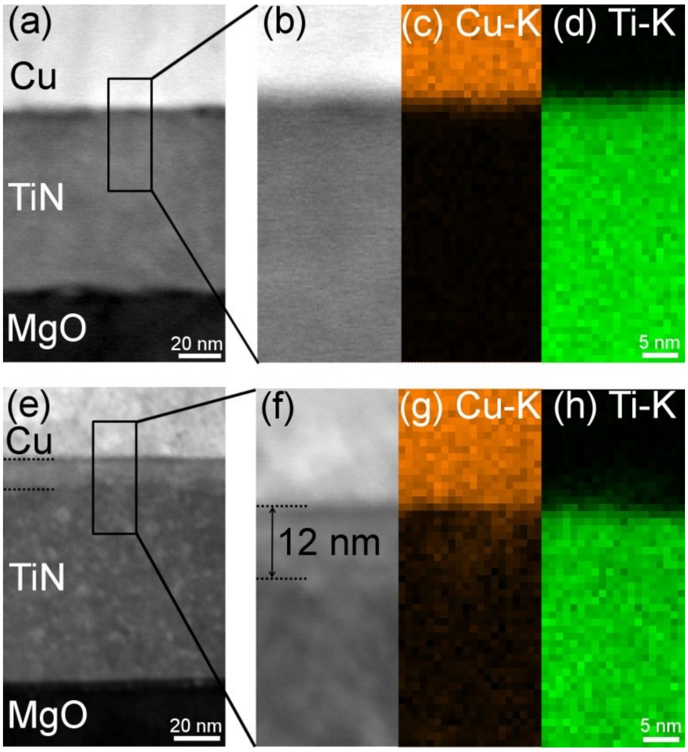

Figure 22: Cross-sectional STEM images obtained with a HAADF detector of samples with an initial Cu layer thickness of 130 nm annealed at (a,b) 900 °C for 1 h and at (e,f) 1000 °C for 12 h. The zoom denotes the areas where EDX maps of the (c) Cu-K and (d) Ti-K edge for the 900 °C sample and of the (g) Cu- K and (h) Ti-K edge for the 1000 °C sample have been recorded. The diffusion layer after annealing at 1000 °C is marked in (e,f).

edge (Fig. 22 (h)), mapping of the Cu-K edge (Fig. 22 (g)) shows diffused Cu in the single-crystal TiN film. The uniformity of the diffusion layer indicates that Cu diffuses via a bulk diffusion mechanism. Based upon the contrast difference in the STEM image the diffusion length is measured to be approximately 12 nm.

The characteristic diffusion length $\bar{x}$ is given by

$$\bar{x} = 2\sqrt{Dt} \ , \tag{15}$$

where *D* is the diffusion coefficient at a given temperature and *t* the time for diffusion.

With the measured diffusion length of 12 nm, the diffusion coefficient at 1000 °C can thus be calculated to be about 8×10^{-18} cm^2s^{-1}. In comparison, diffusion coefficients published for polycrystalline TiN barrier layers are typically in the range of 10^{-15} - 10^{-14} cm^2s^{-1} for annealing temperatures of 900 °C and would be even higher at 1000 °C [5,28]. This illustrates the strong influence of grain boundaries on the performance of the diffusion barrier.

To support the TEM investigations, concentration depth profiles are extracted from APT reconstructions of the Cu/TiN interface of the pristine and annealed samples as shown in Fig. 23. Due to its high sensitivity and sub-nanometer resolution, APT can provide detailed insights into the elemental distribution directly at the interface. APT reveals that the TiN film is slightly substoichiometric for all three sample states (Fig. 23 (a)). In the case of the annealed samples there seems to be a further N loss directly at the interface, but from a depth of about 5 nm into the TiN film, the composition of all three sample states is identical.

A quantitative comparison of the elemental composition of the as-deposited TiN layer as measured by ERDA and APT is given in Tab. 1. The results of the two analyses are in excellent agreement, especially regarding the stoichiometry of the TiN film. Both techniques give a N/Ti ratio of 0.92, indicating the presence of N vacancies in the TiN layer. The measurement error of ERDA is below 1.5 at.% and of APT below 0.1 at.% for all analyzed elements. Deviations in the measured Ar and O contents are present at the error margin of ERDA.

Table 1: Comparison of the elemental composition of the as-deposited TiN film measured by ERDA and APT.

	Ti [at.%]	N [at.%]	Ar [at.%]	O [at.%]	C [at.%]
ERDA	50.9	47.0	1.6	0.1	0.4
APT	51.0	47.2	0.9	0.8	0.1

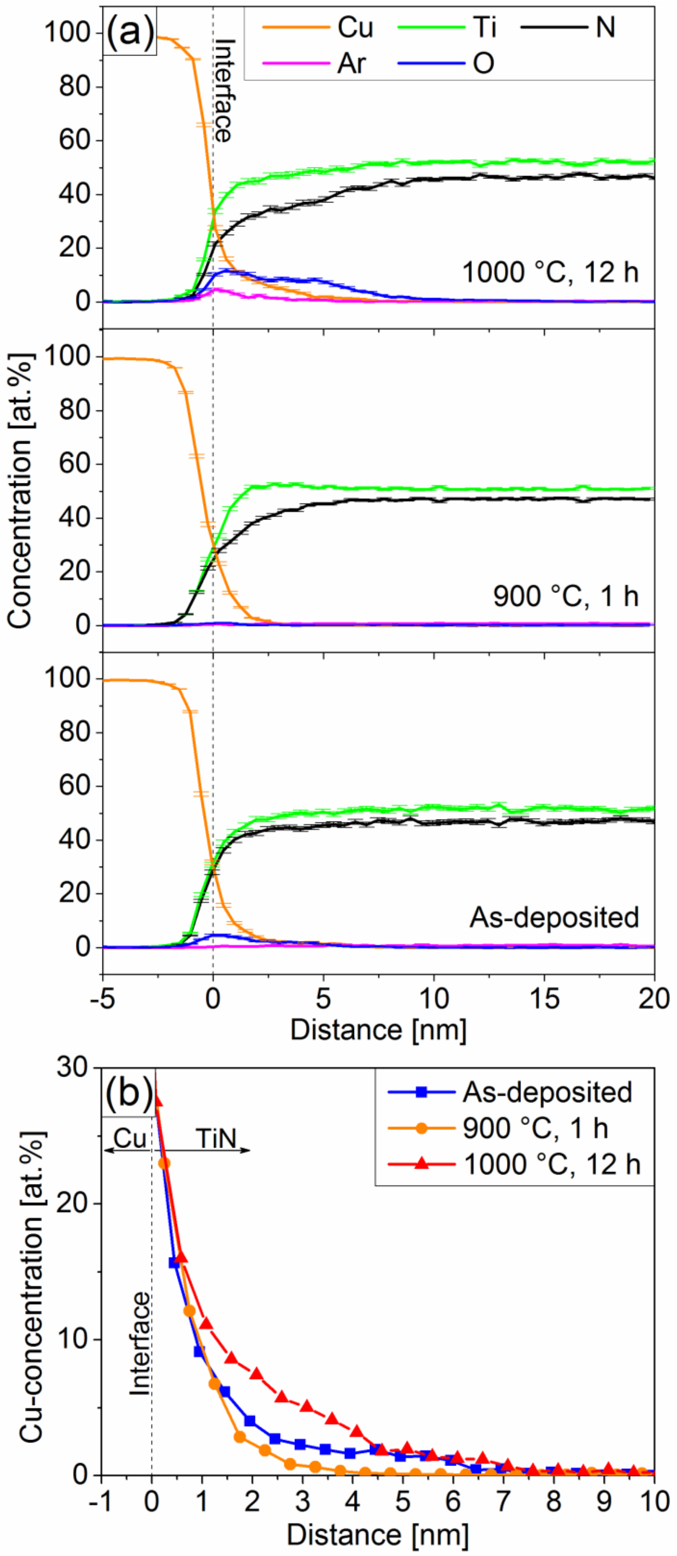

Figure 23: Concentration depth profiles with error bars acquired from representative 3D APT reconstructions of all three sample states (a) and a comparison of the Cu distribution directly at the interface (b). The initial Cu layer thickness was 20 nm in case of the pristine sample and 130 nm in case of the annealed sample states.

In order to test the finding of a slight substoichiometry of the TiN films, XRR measurements of single-layer TiN are performed. The results show a density of 5.4 ± 0.2 g cm^{-3}, which is in agreement with the bulk value of 5.39 g cm^{-3} [29]. Since the TiN density is a direct function of the N concentration in TiN_x ($0.6 \leq x \leq 1.2$) [3], it can be concluded that the TiN films are at most slightly substoichiometric. Also the films are effectively dense without porosity or open percolation paths, as supported by the TEM analyses (Figs. 21 and 22).

The evident Ar incorporation into TiN is a side effect of the biased sputtering process in mixed N_2-Ar atmosphere. According to Hultman *et al.* [30], Ar will likely be incorporated interstitially or in the form of small bubbles (< 2 nm). Furthermore, an O enrichment directly at the Cu/TiN interface is observable in the as-deposited sample in Fig. 23 (a), although no indications for this could be found during the TEM investigations. This O accumulation can most likely be related to the cooling process between the TiN and Cu depositions, where residual gas in the chamber could have adsorbed on the TiN surface. However, the fact that the Cu overlayer adopts the (001) orientation of the underlying TiN points towards a negligibly thin adsorbate layer, so that it cannot be resolved with HRTEM. The O enrichment at the interface is not discernible after the 900 °C annealing treatment in vacuum. Presumably the low amounts of O have diffused into the Cu and TiN layers during the annealing treatment, where they are now evenly distributed as impurities. In case of the sample annealed at 1000 °C in Ar atmosphere, again higher levels of Ar and O are present at the Cu/TiN interface, which is probably a side effect of the annealing treatment and the aforementioned Cu island formation. It is conceivable that during this process Ar and residual O are captured at the interface of the formed Cu islands and the underlying TiN film. The following considerations will not take into account the influence of the O and Ar impurities that are found by APT on the Cu bulk diffusion. Especially in transition metal nitrides, the interplay of defects and impurities is very complex and its comprehensive analysis would go beyond the scope of this study. As shown in Fig. 23 (a) the Cu/TiN interface is spread over approximately 2 nm in the as-deposited sample. From the direct comparison of the Cu depth concentration profiles in Fig. 23 (b) no significant change in the Cu distribution is evident after annealing at 900 °C for 1 h. This is in agreement with the findings of STEM and EDX mapping. On the other hand, after annealing at 1000 °C for 12 h first indications of beginning Cu diffusion are evident in Fig. 23 (b). A slightly elevated Cu concentration is apparent, reaching from the interface approximately 7 nm into the TiN layer. This diffusion length agrees reasonably well with the 12 nm measured in the STEM image. This is an exceptionally short diffusion length compared to values published for polycrystalline TiN diffusion barriers [5,6,31]. A possible reason for the higher efficiency of single-crystal TiN barrier layers is the absence of fast diffusion paths in the form of grain boundaries. The diffusion mechanism is solely controlled by lattice diffusion, where the activation energy is much higher.

3.3.2 Relation to Theoretical Studies

Extensive theoretical studies illustrating diffusion of Cu and other species in TiN are available by Tsetseris *et al.* [12–16], where especially the importance of the defect structure in the TiN film is analyzed based on density-functional theory. In a perfectly stoichiometric, defect-free TiN film the activation energy E_a for diffusion of an interstitial Cu atom is calculated to be 1.4 eV. However, if there is a small number of N vacancies present in the TiN, the Cu atom may be trapped at a N vacancy site with a binding energy of 4.08 eV. According to Tsetseris *et al.* the migration activation energy for such a trapped Cu atom would be so large that in fact it can be considered immobile. A different mechanism emerges when the density of N vacancies becomes so high that another N vacancy is in the vicinity of the trapped Cu atom. The Cu atom can now move to the neighboring N vacancy site while leaving behind a new vacancy. In a second step this new vacancy will then hop to a vicinal N site. The effective activation energy for the migration of such a complex is 2.8 eV [13,15].

Considering the composition of the TiN layers investigated in the present study (Tab. 1), the formation and migration of Cu-N vacancy complexes should be the energetically most favorable atomic-scale mechanism for the lattice diffusion of Cu atoms. With the diffusion coefficient $D = 8\times10^{-18}$ cm^{2}s^{-1} calculated from the measured diffusion length after annealing at 1000 °C, the pre-exponential factor D_0 can be obtained from the Arrhenius-relation

$$D = D_0 \exp\left(-\frac{E_a}{kT}\right), \tag{16}$$

where k denotes the Boltzmann constant and T is the absolute temperature. Solving this equation yields a pre-exponential factor $D_0 = 9.7\times10^{-7}$ cm^{2}s^{-1}.

In summary, Cu diffusion is not active in substoichiometric bulk TiN when Cu atoms get trapped at isolated N vacancies and moderate when the Cu atom can diffuse as a complex together with a N vacancy. If no grain boundaries or fast percolation paths such as connected N vacancy networks are present, the migration of Cu atoms is controlled by a lattice diffusion mechanism.

3.4 CLOSING REMARKS

A complementary combination of HRTEM, STEM and APT is established to study the bulk diffusion of Cu in TiN. HRTEM confirms the single-crystal structure of the TiN layer, and APT uncovers low levels of O and Ar impurities at the interface and reveals a substoichiometry of the TiN film. No discernible Cu diffusion is observed with either technique after annealing at 900 °C for 1 h. After an annealing treatment at 1000 °C for 12 h, a uniform interdiffusion layer with a thickness of 12 nm is observable in STEM images, indicating that Cu diffuses via a lattice diffusion mechanism in single-crystal TiN. APT depth concentration profiles show a comparable diffusion length of 7 nm.

With these values the diffusion coefficient at 1000 °C is calculated to be about 8×10^{-18} cm^{2}s^{-1}. A comparison to theoretical studies [12–16] based on density-functional theory shows that the likely diffusion mechanism in the present substoichiometric TiN films is Cu migration from one N vacancy site to another with an activation energy of 2.8 eV and a pre-exponential factor of about 9.7×10^{-7} cm^{2}s^{-1}. The lack of fast diffusion paths such as grain boundaries contributes to the excellent diffusion barrier properties of single-crystal TiN.

References

[1] K.-C. Park, K.-B. Kim, I.J.M.M. Raaijmakers, K. Ngan, The effect of density and microstructure on the performance of TiN barrier films in Cu metallization, J. Appl. Phys. 80 (1996) 5674–5681.

[2] S.-Q. Wang, I. Raaijmakers, B.J. Burrow, S. Suthar, S. Redkar, K.-B. Kim, Reactively sputtered TiN as a diffusion barrier between Cu and Si, J. Appl. Phys. 68 (1990) 5176–5187.

[3] J.-E. Sundgren, B.-O. Johansson, S.-E. Karlsson, H.T.G. Hentzell, Mechanisms of reactive sputtering of titanium nitride and titanium carbide II: Morphology and structure, Thin Solid Films 105 (1983) 367–384.

[4] M.B. Chamberlain, Diffusion of copper in thin TiN films, Thin Solid Films 91 (1982) 155–162.

[5] M. Moriyama, T. Kawazoe, M. Tanaka, M. Murakami, Correlation between microstructure and barrier properties of TiN thin films used Cu interconnects, Thin Solid Films 416 (2002) 136–144.

[6] A. Gupta, H. Wang, A. Kvit, G. Duscher, J. Narayan, Effect of microstructure on diffusion of copper in TiN films, J. Appl. Phys. 93 (2003) 5210–5214.

[7] M. Mändl, H. Hoffmann, P. Kücher, Diffusion barrier properties of Ti/TiN investigated by transmission electron microscopy, J. Appl. Phys. 68 (1990) 2127–2132.

[8] W. Sinke, G.P.A. Frijlink, F.W. Saris, Oxygen in titanium nitride diffusion barriers, Appl. Phys. Lett. 47 (1985) 471–473.

[9] J.O. Olowolafe, J. Li, J.W. Mayer, E.G. Colgan, Effects of oxygen in TiN_x on the diffusion of Cu in Cu/TiN/Al and Cu/TiN_x/Si structures, Appl. Phys. Lett. 58 (1991) 469–471.

[10] K.T. Nam, A. Datta, S.-H. Kim, K.-B. Kim, Improved diffusion barrier by stuffing the grain boundaries of TiN with a thin Al interlayer for Cu metallization, Appl. Phys. Lett. 79 (2001) 2549–2551.

[11] K.-C. Park, K.-B. Kim, Effect of annealing of titanium nitride on the diffusion barrier property in Cu metallization, J. Electrochem. Soc. 142 (1995) 3109–3115.

[12] L. Tsetseris, N. Kalfagiannis, S. Logothetidis, S.T. Pantelides, Structure and interaction of point defects in transition-metal nitrides, Phys. Rev. B. 76 (2007) 224107.

[13] L. Tsetseris, S. Logothetidis, S.T. Pantelides, Atomic-scale mechanisms for diffusion of impurities in transition-metal nitrides, Surf. Coat. Technol. 204 (2010) 2089–2094.

[14] L. Tsetseris, N. Kalfagiannis, S. Logothetidis, S.T. Pantelides, Role of N defects on thermally induced atomic-scale structural changes in transition-metal nitrides, Phys. Rev. Lett. 99 (2007) 125503.

[15] L. Tsetseris, S. Logothetidis, S.T. Pantelides, Migration of species in a prototype diffusion barrier: Cu, O, and H in TiN, Appl. Phys. Lett. 94 (2009) 161903.

[16] L. Tsetseris, N. Kalfagiannis, S. Logothetidis, S. Pantelides, Trapping and release of impurities in TiN: A first-principles study, Phys. Rev. B 78 (2008) 094111.

[17] T.F. Kelly, D.J. Larson, K. Thompson, R.L. Alvis, J.H. Bunton, J.D. Olson, B.P. Gorman, Atom probe tomography of electronic materials, Annu. Rev. Mater. Res. 37 (2007) 681–727.

[18] T.F. Kelly, M.K. Miller, K. Rajan, S.P. Ringer, Atomic-scale tomography: A 2020 vision, Microsc. Microanal. 19 (2013) 652–664.

[19] D. Mangelinck, F. Panciera, K. Hoummada, M. El Kousseifi, C. Perrin, M. Descoins, A. Portavoce, Atom probe tomography for advanced metallization, Microelectron. Eng. 120 (2014) 19–33.

[20] E.A. Marquis, M. Bachhav, Y. Chen, Y. Dong, L.M. Gordon, A. McFarland, On the current role of atom probe tomography in materials characterization and materials science, Curr. Opin. Solid St. M. 17 (2013) 217–223.

[21] F. Panciera, K. Hoummada, M. Gregoire, M. Juhel, F. Lorut, N. Bicais, D. Mangelinck, Atom probe tomography of SRAM transistors: Specimen preparation methods and analysis, Microelectron. Eng. 107 (2013) 167–172.

[22] International Centre for Diffraction Data, Powder Diffraction File 00-045-0946, 2007.

[23] International Centre for Diffraction Data, Powder Diffraction File 00-038-1420, 2007.

[24] International Centre for Diffraction Data, Powder Diffraction File 00-004-0836, 2007.

[25] L. Hultman, Thermal stability of nitride thin films, Vacuum 57 (2000) 1–30.

[26] G. Abadias, Y.Y. Tse, Determination of intrinsic stresses in textured and epitaxial TiN thin films deposited by dual ion beam sputtering, Surf. Coat. Technol. 180-181 (2004) 33–40.

[27] H. Wang, A. Tiwari, X. Zhang, A. Kvit, J. Narayan, Copper diffusion characteristics in single-crystal and polycrystalline TaN, Appl. Phys. Lett. 81 (2002) 1453–1455.

[28] C. Lee, Y.-L. Kuo, The evolution of diffusion barriers in copper metallization, JOM 59 (2007) 44–49.

[29] L.E. Toth, Transition metal carbides and nitrides, Academic Press, New York, 1971.

[30] L. Hultman, J.-E. Sundgren, L.C. Markert, J.E. Greene, Ar and excess N incorporation in epitaxial TiN films grown by reactive bias sputtering in mixed Ar/N_2 and pure N_2 discharges, J. Vac. Sci. Technol. A 7 (1989) 1187–1193.

[31] K.Y. Lim, Y.S. Lee, Y.D. Chung, I.W. Lyo, C.N. Whang, J.Y. Won, H.J. Kang, Grain boundary diffusion of Cu in TiN film by X-ray photoelectron spectroscopy, Appl. Phys. A-Mater. 70 (2000) 431–434.

CHAPTER 4

COMPARISON OF Cu DIFFUSION IN SINGLE-CRYSTAL AND POLYCRYSTALLINE TiN BARRIER LAYERS

4.1 FUNDAMENTALS

Since its implementation in the 1970s, TiN has become one of the commercially most successful thin film materials [1,2]. Its applications range from hard protective films [3], decorative purposes [4], and coatings on medical implants [5], to diffusion barriers in microelectronics [6]. Such barrier layers are employed to separate the conducting Cu or Al metallization from the Si substrate and surrounding dielectric materials in integrated circuits. Refractory transition metal nitrides in general and TiN in particular are well suited as diffusion barrier materials, due to their high melting points, high thermal stability and good electrical conductivity [7]. Numerous studies are available concerning the barrier performance of TiN and putting forward ways of improving its efficiency. One of the earliest investigations by Chamberlain [8] showed that interdiffusion between r.f. sputtered polycrystalline Cu and TiN layers at temperatures up to 600–700 °C was very limited and presumably occurring via grain boundary or dislocation mechanisms. As a consequence, a widely applied approach to improve the TiN barrier performance is densification by rapid thermal processing or a plasma treatment in NH_3 atmosphere [9–11], or by facilitating the formation of Al-oxides to stuff grain boundaries [12–15]. However, the second effect is limited to Al metallization, since the formation of Cu-oxides at the TiN grain boundaries is thermodynamically not favorable [13,16]. A more promising strategy for Cu metallization might therefore be to tune the microstructure of the TiN barrier layer by adjusting the deposition parameters [16]. For example, Gupta *et al.* [17] grew TiN layers with different microstructures by varying the substrate temperature T_S in a pulsed laser deposition process. Temperatures around 600 °C led to domain matching epitaxial growth of TiN on Si(100), while lower substrate temperatures resulted in polycrystalline (T_S ~ 450 °C) and nanocrystalline (T_S ~ 25 °C) TiN films. Polycrystalline barriers were least resistant against Cu diffusion, with the boundaries between columnar grains providing direct diffusion paths. In the highly textured epitaxial TiN films, the Cu diffusion presumably occurred along low angle grain boundaries. Additionally, the TiN/Si interface with its high dislocation density could have acted as a segregation sink for Cu atoms. Nanocrystalline TiN performed best, which was attributed to the effectively much longer diffusion paths along grain boundaries between nanosized, equiaxial grains. The diffusivity of Cu in TiN could also be influenced by the relative orientation of adjacent grains, as proposed by Moriyama *et al.* [18], who found that in fiber structured TiN layers the Cu diffusivity decreased with decreasing the mosaic spread angle of the grains by depositing at higher substrate temperatures. However, it has to be considered that a variation in the deposition temperature will not only lead to the formation of different microstructures, but will also influence the overall film density. In general, deposition at higher temperatures results in the growth of denser films, due to enhanced surface diffusion of ad-atoms to equilibrium sites, promotion of island coalescence and stimulated desorption of impurities [19]. The application of a negative bias potential to the substrate has similar effects. Bombardment of the growing film with energetic particles will lead to the elimination of interfacial voids and subsurface porosity, and therefore increases film density [20]. Studies by Lee *et al.* [21] showed that for TiN films of comparable stoichiometry and microstructure, the film density was the decisive factor determining the failure temperature of the barrier. An evaluation of Cu diffusion in TiN films of different microstructures should therefore ideally be carried out by studying barrier layers grown at the same substrate temperature and with the same bias voltage, to ensure comparable conditions during film formation and growth.

In the present investigation, the diffusion of Cu in single- and polycrystalline TiN barrier layers deposited at a substrate temperature of 700 °C under a bias voltage of -100 V, sufficient to obtain dense films, is compared. The microstructural variation is achieved by using different substrate materials. Single-crystal (001)-oriented TiN can be readily grown on MgO(001), since both materials have the same crystal structure and a lattice mismatch of only -0.7% [22–25]. Similarly, the growth of columnar polycrystalline TiN on Si and SiO_2 is widely reported [1,26,27]. Pristine and annealed TiN/Cu stacks are investigated by HRTEM techniques and APT. TEM is used to gain insight into the microstructures of the TiN layers, while APT provides three-dimensional maps of the chemical composition in the interface and diffusion regions. Additionally, possible atomic Cu diffusion mechanisms in the single-crystal TiN barrier are examined by density-functional theory (DFT) calculations.

This combined approach of state-of-the-art experimental techniques and first-principles calculations allows to draw a direct comparison between diffusion of Cu in films with different microstructures but deposited under the same conditions. It is thus possible to pinpoint diffusion phenomena and mechanisms in the bulk (supported by DFT calculations) as well as along distinct grain boundaries (by site-specific APT measurements) in a technologically relevant material for diffusion barriers.

4.2 STRUCTURE OF PRISTINE TiN/Cu STACKS

Fig. 24 shows X-ray diffractograms comparing patterns of as-deposited TiN/Cu bilayers grown on (001)-oriented MgO and Si/SiO$_2$ substrates. Both samples are measured in grazing incidence and Bragg-Brentano geometry. In Bragg-Brentano mode the scattering vector is always oriented normal to the substrate surface and thus only reflections from crystallographic planes parallel to the substrate plane are observable. However, in grazing incidence configuration the Bragg reflections are caused by sets of crystallographic planes that are not parallel to the substrate surface nor to each other [28]. This fact can be utilized when comparing data from single- and polycrystalline films measured in both configurations. Fig. 24 (a) shows the grazing incidence diffractogram of the TiN/Cu stack grown on Si/SiO$_2$. All peaks are consistent with (111), (200), and (220) reflections of fcc TiN [29] or fcc Cu [30], indicating that both layers are polycrystalline when grown on Si/SiO$_2$. Due to the small incidence angle of 2° no Si substrate peak is observable. The measurement in Bragg-Brentano mode (not shown) yields an identical diffraction pattern apart from an additional Si substrate peak at 69.1°. On the other hand, the TiN/Cu bilayer assembly deposited on a MgO substrate (Fig. 24 (b)) exhibits no peaks in grazing incidence geometry, suggesting that the TiN as well as the Cu layer grow with their (001) planes oriented parallel with the substrate surface. This can be verified by repeating the measurement in Bragg-Brentano mode. In this configuration, a

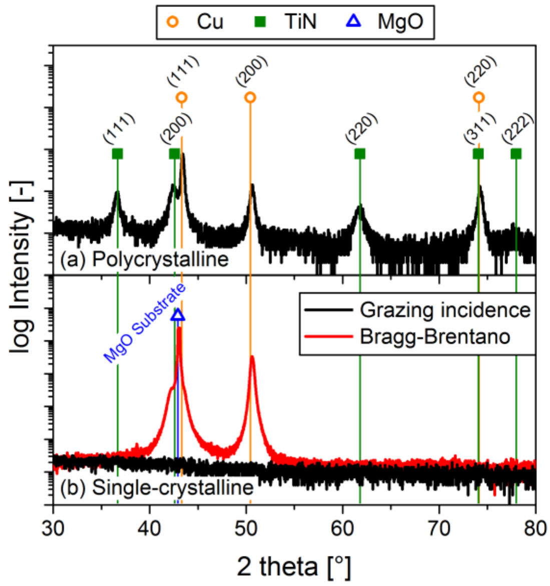

Figure 24: X-ray diffractograms of pristine TiN/Cu stacks grown on (a) Si(001)/SiO$_2$ and (b) MgO(001) measured in grazing incidence and Bragg-Brentano geometry.

pronounced double peak is observable, related to the (200) planes of the TiN film and the MgO substrate [29,31]. Additionally, a reflection consistent with the (001)-oriented Cu top layer [30] appears at a diffraction angle of 50.4°, indicating that both the TiN and the Cu layer grow epitaxially on (001)-oriented MgO. Since the lattice parameters of fcc TiN and fcc MgO are almost identical (4.24 and 4.21 Å, respectively), which is also evident in the peak overlap in the diffractogram, epitaxial TiN of high single-crystalline quality can be grown readily on MgO substrates, given enough energy is provided during film nucleation and growth. In case of the epitaxial Cu top-layer misfit dislocations will relieve some of the strain between the TiN and Cu lattices. This is confirmed by high-resolution TEM investigations (Fig. 25) of the pristine TiN/Cu bilayer deposited on MgO(001). Fig. 25 (a) provides a cross-sectional overview image of the layer arrangement obtained with a HAADF detector in STEM mode. Both layers appear single-crystalline and free of grain boundaries within the observed area. Furthermore, the interfaces are smooth and without any evident interdiffusion. Information about the atomic arrangement directly at the Cu/TiN interface can be gained from a high-resolution bright-field micrograph recorded along the [100] zone axis (Fig. 25 (b)). The measured lattice spacing of the (020) planes in Cu is 0.182 nm. Compared to the bulk value of 0.181 nm for fcc Cu [30], the Cu layer is minimally strained along the [010] direction. Since the lattice mismatch between Cu and TiN is -17%, fully strained epitaxial growth of Cu would result in a larger lattice strain. The excessive strain is thus relaxed by misfit dislocations at the Cu/TiN interface as also found in Refs. [32,33]. A similar mechanism has also been observed for the growth of epitaxial Cu on MgO(001) [34]. As an example, one misfit dislocation represented by an extra half plane in the Cu layer terminating at the interface is marked with an arrow in Fig. 25 (b). The (020) lattice spacing in the TiN layer is 0.202 nm. With respect to the bulk value of 0.212 nm, TiN is compressed along the [010] direction. In addition to the complex strain state resulting from the lattice mismatch between the layers and the substrate, and the differential contraction of the materials during cooling-down from deposition temperature [35], another possible reason for these compressive lattice strains could be the incorporation of Ar as well as

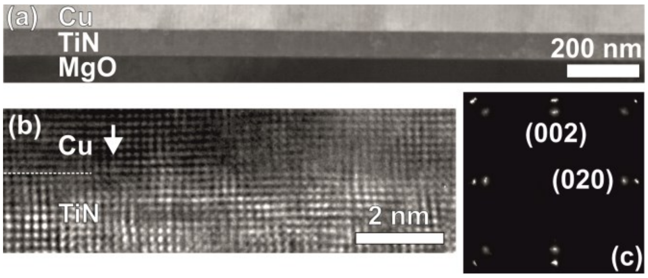

Figure 25: TEM images of the pristine single-crystal TiN/Cu stack grown on MgO(001): (a) cross-sectional dark field image giving an overview of the layer arrangement, (b) high-resolution bright field micrograph of the Cu/TiN interface with a misfit dislocation marked by an arrow, and (c) the corresponding SAED pattern showing an epitaxial cube-on-cube orientation relationship between the Cu and the TiN layer.

the interplay of point defects (interstitials and vacancies) often observed in sputtered TiN [1,36,37]. To confirm epitaxial growth of the TiN/Cu stack, selected area electron diffraction (SAED) patterns are recorded along the Cu/TiN interface. A representative SAED pattern (Fig. 25 (c)) shows spots consistent with single-crystal Cu (appearing farther outside due to the smaller lattice parameter) and single-crystal TiN with a cube-on-cube alignment between the two layers.

In contrast, the TiN film grown on the Si/SiO_2 substrate exhibits a fine grained nucleation layer close to the Si/SiO_2/TiN interface, morphing into a typical polycrystalline zone T microstructure [38] with a dense array of cone-shaped columnar grains, as displayed in the cross-sectional bright-field TEM image in Fig. 26 (a). The Cu top layer consists of comparably large grains without a discernible orientation relationship to the underlying TiN. While the TiN/Cu interface is smooth and well-defined, the Cu surface is wavy. A bright surface layer visible on top of the Cu film can be related to the formation of a native Cu_2O layer in ambient atmosphere. Similarly, the amorphous SiO_2 grown to prevent Si diffusion into the TiN film is visible in Fig. 26 (a) as a bright 5 nm thick interlayer at the TiN/Si interface. To rule out the possibility of Cu diffusion occurring already during the deposition process, micrographs as shown in Fig. 26 (b) are recorded with a HAADF detector, where the contrast scales with Z^2 (atomic number squared) [39,40]. No interdiffusion layers of different contrast are detected across either of the two interfaces, nor along the grain boundaries in

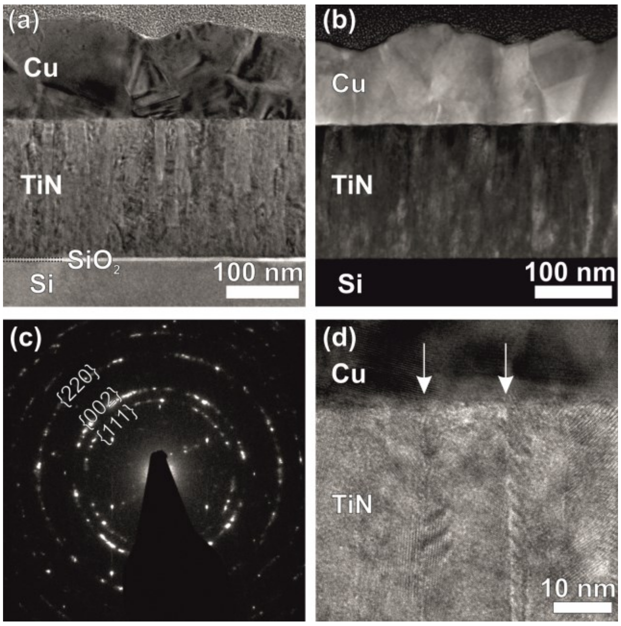

Figure 26: TEM images of the pristine polycrystalline TiN/Cu stack grown on Si/SiO2: (a) cross-sectional bright field image giving an overview of the layer arrangement, (b) dark field micrograph displaying no discernible Cu or Si diffusion along the grain boundaries between columnar TiN grains, (c) corresponding SAED pattern showing (111), (002), and (220) diffraction rings related to TiN, and (d) a high-resolution bright field micrograph of the Cu/TiN interface with two grain boundaries marked by arrows.

TiN. A SAED pattern obtained along the [110] zone axis at the TiN/Si interface (Fig. 26 (c)) shows diffraction rings for polycrystalline TiN in agreement with the XRD investigations. Brighter sections of the rings are not related to film texture but to the restricted sample area and thus the limited number of grains illuminated within the selected area aperture. Fig. 26 (d) provides a closer look at the Cu/TiN interface in a high-resolution micrograph. As an example, two grain boundaries running almost perpendicular to the interface in the columnar TiN barrier layer are marked by arrows. The boundaries are dense without discernible intercolumnar porosity. In the vicinity of the interface the column width is approximately 10-15 nm. The Cu/TiN interface is flat and the tops of the TiN columns are only marginally rounded, revealing very shallow troughs at the boundaries.

Not only the film structure but also the film density affects the diffusion barrier performance [21]. Therefore, the development of the density in the TiN/Cu stack is investigated by XRR measurements. In the previous chapter, the density of a single-crystal TiN film deposited on MgO(001) with the same parameters as for the TiN barriers presented here is found to be 5.4 ± 0.2 g cm^{-3}, which is in agreement with the bulk value of 5.39 g cm^{-3} [41]. Due to the contribution of grain boundaries, sputtered polycrystalline films are generally expected to be less dense. The recorded XRR curve for the polycrystalline barrier is shown in Fig. 27 (a). The best fit is achieved by a model comprised of a 4.8 nm thick Cu_2O surface layer, a 139.0 nm thick Cu layer, a 214.6 nm thick TiN barrier, and a 4.9 nm thick SiO_2 layer on the Si substrate. A slight deviation in film thicknesses

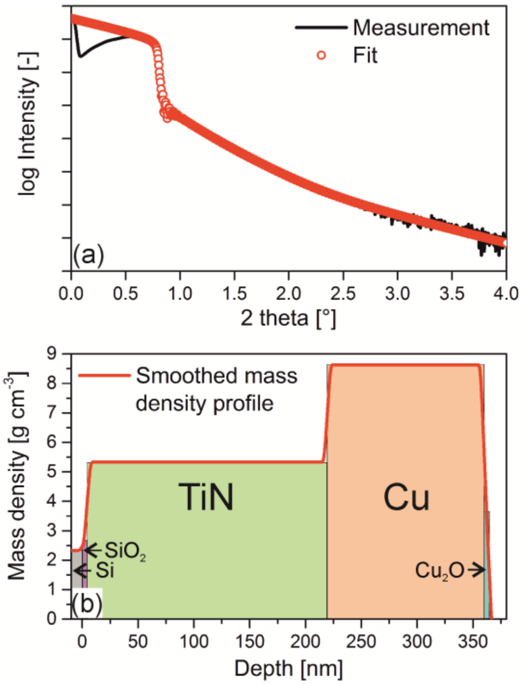

Figure 27: (a) Experimental and calculated XRR (fitted by a genetic algorithm fit according to the Nevot-Croce interface model) curves and (b) corresponding density depth profile of the polycrystalline TiN/Cu stack grown on Si/SiO_2 at 700 °C.

measured by TEM and obtained from XRR fits can be attributed to variations due to shadowing effects at the outer margins of the samples and the limited area observed in TEM. Fig. 27 (b) displays the resulting density depth profile, where the zero point is defined as the interface between the Si substrate and the thermal SiO_2. The density of the polycrystalline TiN layer deposited at 700 °C is 5.3 ± 0.2 g cm^{-3}, which is 98% of bulk density. Similar observations have been reported by Petrov *et al.* [27] and Patsalas *et al.*[42], who found that given enough energy in the form of moderate ion bombardment or substrate heating is provided to the film forming species to promote ad-atom surface diffusion and to fill voids, sputtered polycrystalline TiN films will grow with almost fully dense grain boundaries and a relatively low intragranular defect density. Although the grain boundaries still will be the main diffusion channel in polycrystalline barrier layers, their high internal density is expected to restrict the migration of Cu atoms more severely than in comparable barrier layers deposited at lower substrate temperatures without externally applied bias potential. The density of the Cu top layer with a value of 8.6 ± 0.2 g cm^{-3} is slightly below bulk density (8.9 g cm^{-3}), owing to limited atomic mobility during the growth process at 50 °C and floating potential.

4.3 DIFFUSION IN ANNEALED TiN/Cu STACKS

To activate the diffusion of Cu from the top layer into the TiN films, the samples are subjected to isothermal annealing treatments at 900 °C for 1 h. In case of the single-crystal TiN/Cu stack, de-wetting of the Cu top layer is evident after the annealing treatment. The reasons for solid state de-wetting of Cu films include strain-induced instabilities due to the lattice mismatch and faceting instabilities (surface energy $\gamma_{\mathrm{Cu}(111)} < \gamma_{\mathrm{Cu}(001)}$) [43]. This behavior was observed previously and can be interpreted as a sign of the efficiency of the employed barrier layer [44]. Further investigations are performed directly at the center of the formed Cu agglomerates, to ensure that enough Cu is available as a diffusion source. Cross-sectional TEM images of the TiN/Cu stacks after annealing obtained with a HAADF detector are shown in Fig. 28. The single-crystal TiN/Cu bilayers grown on MgO(001) (Fig. 28 (a)) still exhibit no internal structure, indicating that the epitaxial configuration is stable up to temperatures of 900 °C. The Cu top layer is now discontinuous and has agglomerated to islands with a diameter of up to 4 µm due to solid state de-wetting. A black rectangle at the Cu/TiN interface marks the area where the corresponding qualitative EDX maps, also displayed in Fig. 28 (a), have been recorded with the pixel size set to 1×1 nm^2. The RGB image constructed from the signals of the Cu-K and the Ti-K edges, which are also shown separately for clarity, has an area of 20×50 nm^2. The signal from the N-K edge is too weak to be considered significant and is therefore not plotted. During scanning, the Cu/TiN interface is oriented slightly inclined, to ensure that no sample drift takes place influencing the EDX mapping over the otherwise featureless sample. No discernible diffusion of Cu across the interface can be detected by EDX.

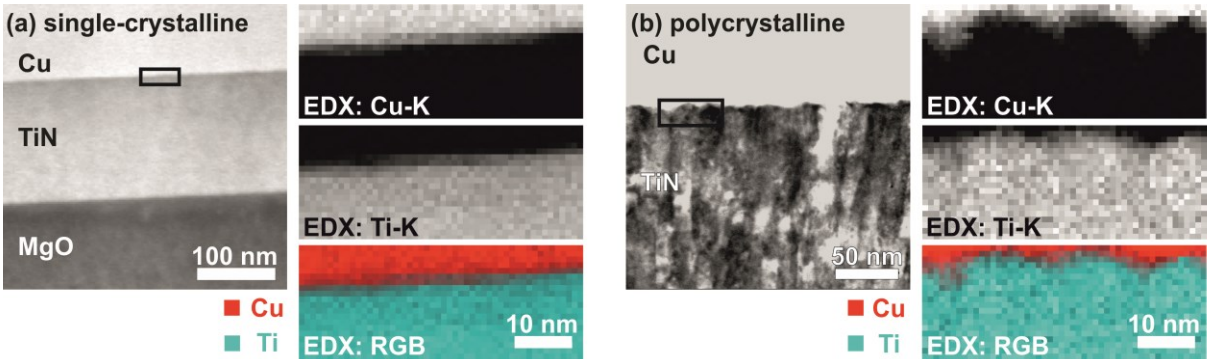

Figure 28: STEM-HAADF images and corresponding EDX maps (pixel size 1×1 nm) of the Cu-K and the Ti-K edges of the (a) single-crystal TiN/Cu stack grown on MgO(001) and (b) polycrystalline TiN/Cu stack grown on Si/SiO$_2$ after the annealing treatment (900 °C, 1 h).

In contrast to the single-crystal bilayers, the onset of grain boundary diffusion is evident in the polycrystalline TiN/Cu stack presented in Fig. 28 (b). While the Cu/TiN interface is smooth with minimal troughs at the column boundaries in the pristine sample (Fig. 26 (a,d)), pronounced Cu accumulation and beginning penetration is observed locally at TiN column boundaries after annealing at 900 °C for 1 h, leading to a wavy appearance of the interface. Corresponding elemental maps (pixel size 1×1 nm^2) confirm the preferential diffusion of Cu along grain boundaries in the polycrystalline TiN layer. Because of the uncertainty of the exact location of the interface and limitations in the spatial resolution of the probe, it is however not possible to quantify the diffusion length precisely from the acquired maps. Moreover, according to Fick's second law, the concentration of the diffusing Cu atoms will decrease with increasing diffusion length [45]. In combination with the small excitation volume in the thin TEM foil, the EDX detector might not receive sufficient X-ray counts to resolve the low Cu concentrations further along the grain boundaries [46].

To complement the TEM findings, the annealed single- and polycrystalline TiN/Cu bilayers are also investigated by APT. Three datasets are measured and evaluated in each case with consistent results. A cylindrical region of interest (ø 20 nm×100 nm) containing the Cu/TiN interface is shown in Fig. 29 for both samples after annealing at 900 °C. For clarity, only Cu and TiN ions have been plotted. Throughout the TiN layer, Ti and N ions have also been detected in their dissociated forms, but are not shown here. Additionally, significant amounts of Ar ions have been observed as impurities. This is a result of the sputter deposition process, where Ar ions impinge on the growing film and become trapped [47].

Hereafter, the differences in chemical composition and diffusion characteristics in the two samples will be discussed in more detail: Fig. 29 (a) shows the three-dimensional reconstruction of the annealed single-crystal TiN/Cu stack. Each data point in the reconstruction represents one measured Cu or TiN ion. The corresponding volume concentration distribution of Cu ions is plotted alongside to visualize the elemental composition in the vicinity of the interface. The N/Ti ratio in the TiN(001) barrier layer, obtained after performing a decomposition of overlapping peaks in the recorded APT mass spectrum, is 0.92. This ratio is confirmed by elastic recoil detection analysis of a single-layer TiN(001) film deposited with the same parameters as the studied barrier layer, indicating that the peak decomposition algorithm is suitable to accurately describe the chemical composition in the investigated sample volumes. A slightly substoichiometric composition is typical for sputtered TiN films, and N vacancies have been identified as the primary defect in these structures [26,48]. Ar impurities are evenly distributed in the TiN(001) barrier layers as discrete atoms without any evident clustering. According to APT the overall Ar concentration in TiN is below 1 at.%. The Cu(001) layer is essentially Ar free as a result of the limited ion irradiation during the deposition at floating potential. The Cu/TiN interface appears well-defined in the reconstruction. Only minor intermixing with some Cu atoms positioned in the TiN layer (3 nm into the TiN layer, one out of every 100 atoms is Cu) and vice versa can be observed in the near interface region. In the concentration distribution of Cu, a rapid drop occurs from 100 at.% Cu in the pure Cu film to 0 at.% Cu in the barrier layer. This behavior corroborates the TEM and EDX findings, confirming that single-crystal TiN is effective in preventing Cu diffusion after annealing at 900 °C for 1 h. The onset of Cu diffusion into the TiN(001) barrier could only be observed after a 12 h annealing treatment at 1000 °C, as reported in the previous chapter as well as Ref. [49]. The good performance of this barrier can be related to the dense, ordered structure of the single-crystal TiN layer and the lack of fast diffusion channels such as grain boundaries.

Fig. 29 (b) displays the reconstruction and Cu distribution profile in a representative annealed polycrystalline APT specimen. All of the three evaluated specimen reconstructions contain at least one TiN grain boundary along which Cu diffusion is observed. The reconstruction shown in Fig. 29 (b) is chosen as a representation because the specimen contains several grain boundaries, and thus offers the most diverse illustration of Cu diffusion profiles. Again the chemical composition of the TiN layer is calculated after analyzing the mass spectrum. The obtained N/Ti ratio of 0.99 is higher than for the single-crystalline case. During the annealing treatment, the grain boundaries can act as sinks for N vacancy annihilation in polycrystalline TiN, giving a possible explanation for this observation [50]. Furthermore, a change in the distribution of Ar impurities is evident when a larger reconstructed region (not shown here) of the TiN layer is investigated. While the Ar is still evenly spread throughout the TiN, some Ar bubbles with a diameter in the range of a few nanometers can be found.

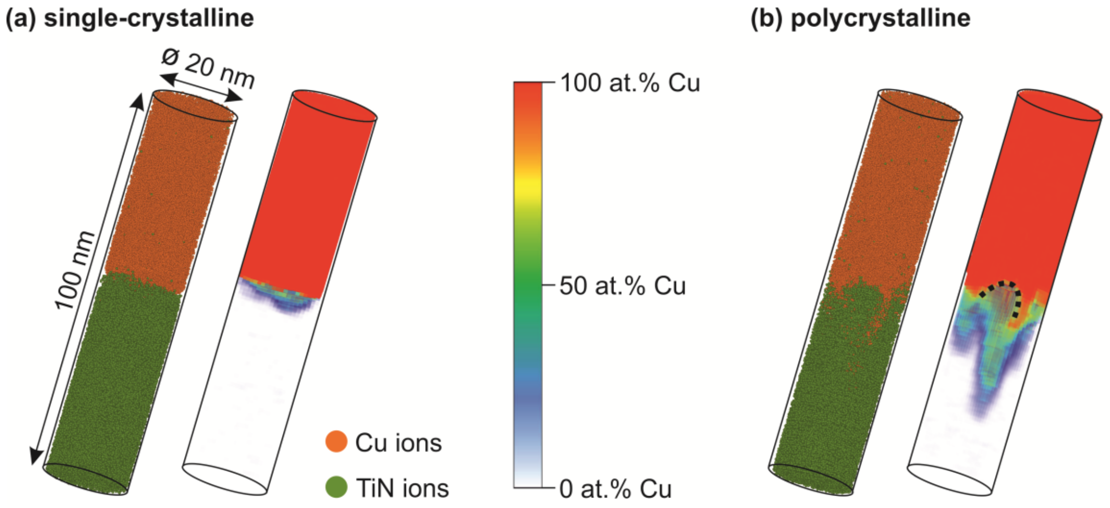

Figure 29: Three-dimensional APT reconstructions (ø 20 nm×100 nm) and corresponding Cu concentration plots of the (a) single-crystal TiN/Cu stack grown on MgO(001) and (b) polycrystalline TiN/Cu stack grown on Si/SiO$_2$ after the annealing treatment (900 °C, 1 h).

Presumably, the formation of these bubbles is energetically more favorable at the boundaries between the columnar grains, because of the relatively large stress associated with the incorporation of Ar in bulk TiN [47,51]. The overall Ar concentration in the TiN layer is below 1 at.%, and no Ar impurities can be observed in the Cu layer. To my knowledge, this is the first observation of Ar bubbles in TiN films containing so little as 1 at.% Ar, and it corroborates the usefulness of APT for functional ceramics.

In the three-dimensional reconstruction shown in Fig. 29 (b), local migration of Cu across the interface is evident, which is indicative of an active grain boundary diffusion mechanism during the annealing treatment at 900 °C. This is even more prominently displayed in the volume concentration plot of Cu. The TiN structure revealed in the TEM images (Fig. 28 (b)) after annealing is reproduced with its characteristic columns (diameter in the range of 10-15 nm) and troughs at the boundaries, as marked by the black dotted line in the APT concentration plot in Fig. 29 (b). Along these boundaries a locally increased Cu concentration can be measured. A grain boundary represents a transition structure between two crystals and thus the incorporation of local defects is required to account for the change in grain orientation and translation. Therefore, the atomic packing in a grain boundary core is less dense than in a perfect crystal. As a result, a grain boundary will always provide a faster diffusion path than a single crystal [52]. Still, the migration of atoms along the boundary may be hindered by tuning its density. In the present study, a high internal density of grain boundaries is achieved by promoting the ad-atom surface diffusion and film densification during deposition of the TiN barrier layer by supplying energy in the form of substrate heating (700 °C) and moderate ion bombardment (-100 V bias potential). The longest Cu diffusion path measured in a grain boundary in Fig. 29 (b) is approximately 30 nm. In comparison, the diffusion depth in a polycrystalline TiN barrier deposited at room temperature without an externally applied bias potential is already more than 25 nm after annealing for 30 min at temperatures as low as 750 °C, as reported by Moriyama *et al.* [18]. Fig. 29 (b) also shows that the penetration depth of Cu into the TiN layer is not uniform, which further illustrates the dependence of Cu migration through grain boundaries on their atomic structure. For example, it was found that grain boundaries with small misorientation and mosaic spread angles generally perform better in constricting diffusion, due to their higher atomic packing density [18,53,54]. In this context it also has to be noted that because of the nature of TEM and especially APT investigations, only limited areas of the samples can be analyzed. It is therefore possible that for other grain boundary configurations in the same sample, Cu atoms could migrate further into the TiN layer. However, to demonstrate the general good performance of the dense polycrystalline TiN barrier, a maximum diffusion length $\bar{x}$ of 30 nm as measured in Fig. 29 (b) is assumed. Since no significant lattice diffusion is observed in the single-crystal TiN film, it is further assumed that diffusion only occurs along the grain boundaries and diffusion into the grains is negligible. With an infinite source diffusion approximation, the grain boundary diffusion coefficient *D* at a given temperature can then be derived from Einstein's formula [55]

$$\bar{x} = 2\sqrt{Dt}\,, \tag{17}$$

where *t* is the time for diffusion. This yields a grain boundary diffusion coefficient of $(6 \pm 2)\times10^{-16}$ $\mathrm{cm^2s^{-1}}$ for a temperature of 900 °C in dense polycrystalline TiN, which is 1-2 orders of magnitude lower than for comparable TiN coatings deposited without external substrate heating [7,18].

4.4 THEORETICAL CONSIDERATIONS

The experiments outlined above suggest that diffusion in polycrystalline TiN occurs via grain boundaries at a rate 2 orders of magnitude higher than bulk diffusion [49]. To explain such a difference, a thorough comparison of the diffusion mechanisms in bulk and along the grain boundaries is required. There are, however, two factors to consider: *i)* the structure of the grain boundaries involved in the diffusion process is presently unknown; and *ii)* although the Cu-diffusion in bulk TiN has already been investigated by means of *ab initio* atomistic calculations [56], the relevant diffusion mechanism and the role of stoichiometry in TiN remains unclear. Thus, in this section the focus is laid on the diffusion mechanisms in single-crystal TiN [57].

The diffusion process from a macroscopic point of view can be described with an Arrhenius type equation:

$$D = D_0 \exp\left(-\frac{Q}{k_B T}\right). \tag{18}$$

Here, D_0 is the exponential pre-factor and Q is the activation energy. The diffusion parameters, D_0 and Q, are determined by the underlying atomistic mechanism of diffusion and are often used to compare different mechanisms. To predict the most probable diffusion mechanism, the activation energies corresponding to various possible mechanisms described below are calculated, and the mechanism with the lowest activation energy is identified as the most likely one for the diffusion of Cu in bulk-like TiN. In particular, it has to be distinguished between vacancy-mediated impurity diffusion and a diffusion mechanism via interstitial positions.

The vacancy-mediated impurity diffusion coefficient for a fcc lattice can be written as follows [58]

$$D_2 = a^2 f_2 C_v \omega_2 \tag{19}$$

Here, a is the lattice parameter, f_2 is the impurity diffusion correlation factor, $C_v = exp\left(-\frac{G_f + G_b}{k_B T}\right)$ is the vacancy concentration adjacent to the solute atom and $\omega_2 = \frac{k_B T}{h} exp\left(-\frac{G_2^m}{k_B T}\right)$ is the impurity jump rate from transition state theory [59]. The free energies difference G (symbol Δ is omitted for convenience) in the previous equations can be written as $G = E - TS$ with E being the energy difference and S the entropy difference. Thereby, equation (19) becomes

$$D_2 = \frac{k_B T}{h} a^2 f_2 \, exp\left(\frac{S_f + S_b + S_2^m}{k_B}\right) exp\left(-\frac{E_f + E_b + E_2^m}{k_B T}\right). \tag{20}$$

Here, $E_f(S_f)$ is the vacancy formation energy (entropy) and $E_b(S_b)$ is the vacancy-impurity binding energy (entropy). The latter is defined as the difference between vacancy formation energy (entropy) in the vicinity of solute atoms and that in the pure bulk. In the convention adopted here, negative values of E_b correspond to an attractive interaction between vacancy and solute. Finally, $E_2^m(S_2^m)$ is the impurity migration energy (entropy). This is the energy (entropy) difference between the system in the initial state and the system in a configuration corresponding to the top of the energy barrier which the impurity atom has to overcome in order to diffuse to the nearest-neighboring vacancy site.

For the interstitial diffusion mechanism, the diffusion coefficient is given by the following expression:

$$D_2 = \frac{k_B T}{h} a^2 exp\left(\frac{S_{Int}^m}{k_B}\right) exp\left(\frac{-E_{Int}^m}{k_B T}\right). \tag{21}$$

In the present study the entropic, in particular vibrational, contributions are not taken into account, which prohibits calculating D_2. However, when comparing equations (20) and (21) to the Arrhenius form for the diffusion coefficient (equation (18)), the activation energy can be approximated as $Q = E_f + E_b + E_2^m + C$ (here C takes the contribution from the correlation factor into account) for vacancy mediated mechanisms and $Q = E_{Int}^m$ for the interstitial mechanism. In the following, the focus is placed on comparing activation energies obtained for various mechanisms, in order to clarify their relative importance.

4.4.1 Defect Concentrations

The simplest point defects considered are vacancies both on the N and Ti sublattices denoted as V_N and V_{Ti}, respectively, antisites (Ti_N and N_{Ti}) and interstitials (Ti_{Int} and N_{Int}). In order to compute concentrations of those defects within the DSM, the associated excitation energies are calculated. They are defined as the energy difference between the defective and the perfect supercell.

Defect excitation energies are shown in Table 2. Here, the effect of temperature is taken into account by using the supercell calculations with the experimentally measured lattice parameter at 1273 K [60], but no entropy contribution is considered. It has to be noted that the values of the excitation energies themselves do not have a direct physical meaning, since they are governed by the number and kind of atoms in the supercells, which are different for each considered defect.

Table 2: Calculated excitation energies of intrinsic point defects in TiN. The ground state energy per formula unit of the stoichiometric TiN is $E_0 = -19.912$ eV.

Defect	Excitation energy, [eV]
V_N	10.705
V_{Ti}	11.972
Ti_N	10.098
N_{Ti}	11.957
Ti_{Int}	-1.636
N_{Int}	-3.918

Solving the DSM, concentrations of defects (c_d) as well as chemical potentials of Ti and N (μ_{Ti} and μ_{N}) are obtained as a function of the TiN composition. The concentrations of defects are converted to the *effective* formation energies (E_f) using the relation $E_f = -k_B T ln(c_d)$, where k_B denotes the Boltzmann constant and T is the temperature. These energies are shown in Fig. 30 as a function of the N concentration in TiN. V_N and V_{Ti} have the lowest defect formation energies in the N-deficient and Ti-deficient region respectively, and consequently they are the dominant defects in the corresponding concentration regions. Therefore, it can be concluded that the only defects which can significantly influence the Cu diffusion process are vacancies, while contributions from other types of defects are negligible.

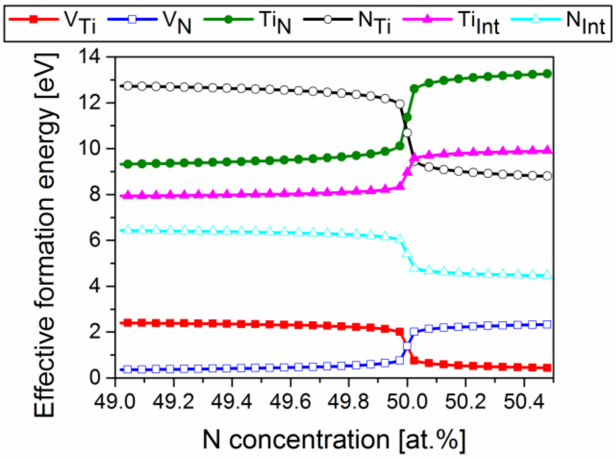

Figure 30: Effective formation energy of point defects in TiN as a function of composition obtained from the DSM at a temperature of 1273 K.

Furthermore, the formation energies $E_f(Cu_x)$ of a Cu impurity on the corresponding sublattices X (Ti, N or Int) in TiN are calculated. The following relations were used for calculating $E_f(Cu_x)$ for a dilute concentration of Cu:

$$E_f(Cu_{Ti}) = E(Cu_{Ti}) - E(TiN) + \mu_{Ti} - \mu_{Cu} , \tag{22}$$

$$E_f(Cu_N) = E(Cu_N) - E(TiN) + \mu_N - \mu_{Cu} , \tag{23}$$

$$E_f(Cu_{Int}) = E(Cu_{Int}) - E(TiN) - \mu_{Cu} . \tag{24}$$

Here, $E(TiN)$ is the total energy of the bulk TiN supercell, $E(Cu_X)$ is the total energy of the TiN supercell with Cu on site X, and μ_{Cu} is the chemical potential of Cu corresponding to the energy per atom in fcc Cu. The calculated values of $E_f(Cu_x)$ are plotted in Fig. 31. In the N-deficient region of TiN, the Cu impurities reside mostly on the N sublattice, while they occupy the Ti sublattice in stoichiometric TiN. The formation energy on the interstitial sublattice is significantly higher compared to the other two sublattices, which implies that the fraction of interstitial Cu impurity atoms is nearly vanishing in the whole considered composition range.

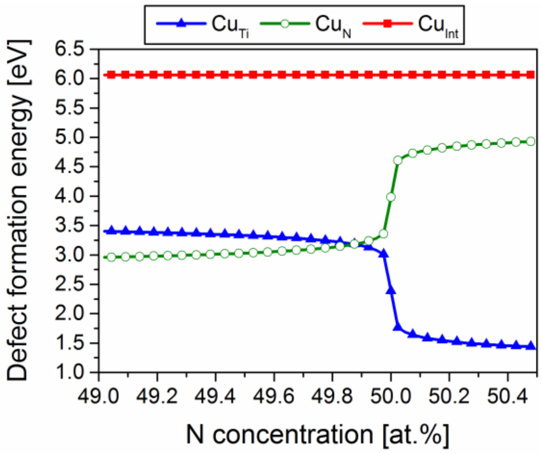

Figure 31: Formation energy $E_f(Cu_x)$ of a Cu impurity on different sites in TiN as a function of composition at 1273 K.

4.4.2 Migration Barriers and Activation Energies

Considering the two types of diffusion mechanisms discussed above, the respective migration barriers and the total diffusion activation energies have been calculated. The simplest possible diffusion mechanism for a Cu impurity in the TiN single crystal is diffusion via interstitial sites as described by equation (21). The most stable interstitial configuration for a Cu atom is found to be in the center of a TiN cell. Migration of a Cu impurity between stable positions is calculated using the NEB method and occurs with the energy barrier E_{Int}^{m} of 1.39 eV at 0 K and at the slightly lower value of 1.23 eV at high temperature, owing to the larger lattice spacing at elevated temperatures. The energy barrier of 1.39 eV at 0 K is in good agreement with the previously calculated value of 1.4 eV (Table 3).

The second possible mechanism for Cu impurity diffusion is via vacancies as described by equation (20). In this case, diffusion takes place via solute-vacancy exchange jumps. Both possibilities of Cu atom diffusion either via the Ti sublattice or via the N sublattice are considered: The five-frequency model is applied to analyze these processes [54]. This model is commonly used to describe the impurity diffusion correlation factor, which depends on the vacancy-jump frequencies near the impurity. Taking into account vacancy-impurity interactions only up to the second-nearest neighbor, in this model the correlation factor f_2 from equation (19) for the diffusion coefficient in the fcc lattice can be written as [61]

$$f_2 = \frac{2\omega_1+7F\omega_3}{2\omega_2+2\omega_1+7F\omega_3}, \tag{25}$$

where

$$7F = 7 - \left[\frac{10\alpha^4+180.5\alpha^3+927\alpha^2+1341\alpha}{2\alpha^4+40.2\alpha^3+254\alpha^2+597\alpha+436}\right]. \tag{26}$$

Here, $\alpha = \omega_4/\omega_0$, and $\omega_i = \frac{k_B T}{h} exp\left(-\frac{E_i^m}{k_B T}\right)$ are the rates of different types of vacancy jumps in the vicinity of a solute atom with E_i^m being equal to the migration barrier of the corresponding jump (entropic contribution is not included). ω_2 corresponds to the solute-vacancy exchange jumps, ω_1 is the rate of vacancy-solvent jumps in the first coordination shell of the solute atom, ω_3 is the rate of vacancy jumps from the first-nearest neighbor positions to solute atoms at more distant sites, and ω_4 is the rate of reverse jumps. All other vacancy-solvent jumps are assumed to occur at a rate of ω_0, which corresponds to the solvent-vacancy exchange jump in the pure solvent.

The migration barriers E_i^m corresponding to all ω_i for Cu diffusion are calculated both via the Ti and N sublattice and are presented together with the value for the barrier for migration via interstitial sites E_{Int}^{m} in Table 3. For the numerator in equation (9) it has been found that $2\omega_1 \gg 7F\omega_3$, and $2\omega_2 \gg (2\omega_1 + 7F\omega_3)$ for the denominator. Therefore, equation (25) can be approximated as $f_2 \approx \omega_1/\omega_2$. Substituting equation (25) into equation (19) for the diffusion coefficient results in

$$D_2 = a^2 C_v \omega_1. \tag{27}$$

This means that the diffusion process of a Cu impurity via a vacancy is limited by the vacancy exchange with a solvent atom in the vicinity of the solute atom. As a consequence, the activation energy for vacancy mediated diffusion transforms into $Q = E_f + E_b + E_1^m$.

Table 3: Migration barriers E_i^m [eV] corresponding to the different vacancy exchange jumps (ω_i) in the vicinity of the impurity atom and for migration via interstitial sites calculated with the lattice parameters at 0 K and 1273 K.

		E_0^m	E_1^m	E_2^m	E_3^m	E_4^m	E_{Int}^m
Ti sublattice	0 K	4.08	2.96	0.27	4.18	4.16	
	1273 K	3.69	2.54	0.08	3.74	3.74	
N sublattice	0 K	3.75	2.62 (2.8*)	1.90 (2.0*)	4.14	4.20	
	1273 K	3.32	2.20	1.70	3.67	3.63	
Interstitial	0 K						1.39 (1.4*)
	1273 K						1.23

*Tsetseris *et al.* [56] (values in parentheses)

Combining the results for *i)* the vacancy formation energies derived from the DSM calculation, *ii)* the binding energy E_b of a vacancy with a Cu impurity, which is found to be weak and repulsive (0.07 eV) for a Cu_N-V_N pair, and attractive (-0.05 eV) for a Cu_{Ti}-V_{Ti} pair, and *iii)* the migration barriers from the NEB, the composition dependent activation energy of Cu impurity diffusion in TiN is obtained as presented in Fig. 32. It is found that among all possible investigated diffusion mechanisms, the interstitial diffusion mechanism has the lowest activation energy. In the N-deficient region, the mechanism with the second lowest activation energy is Cu impurity diffusion via the N sublattice, while in the N-rich region the diffusion via the Ti sublattice is more favored.

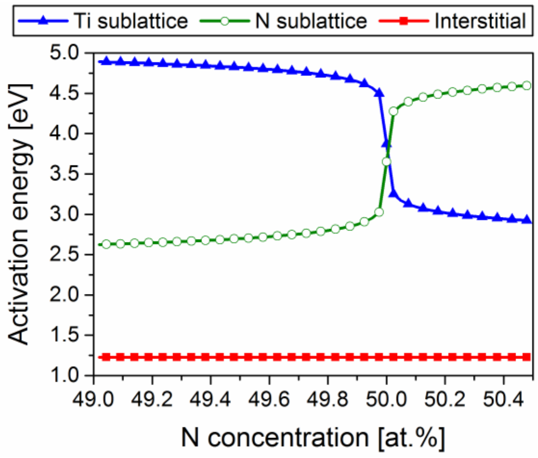

Figure 32: Activation energy of Cu impurity diffusion in TiN at 1237 K.

In summary, the calculations show that the diffusion of Cu via interstitial sites has the lowest activation energy as compared to the vacancy-mediated diffusion mechanisms. However, this diffusion mechanism is highly unlikely because of the high formation energy associated with a Cu atom on the interstitial site. Therefore, the diffusion of Cu in TiN is proposed to occur via a vacancy mechanism. From the DSM model it can be concluded that in N-deficient TiN, the Cu diffusion occurs via the N sublattice due to the elevated concentration of N vacancies. This results in a relatively small activation energy of about 2.6 eV for a N concentration of 49 at.% at 1273 K. This theoretical prediction is in good agreement with the activation energy of 2.7 eV obtained experimentally by Moriyama *et al.* for bulk diffusion of Cu in TiN, although it has to be noted that the TiN films investigated by Moriyama *et al.* were N-rich [18]. In stoichiometric TiN, however, the formation energy of Cu on the Ti sublattice is significantly lower compared to the N sublattice. For this reason, Cu is expected to diffuse via the Ti sublattice, with a considerably larger activation energy of 3.87 eV, while diffusion on the N sublattice is unlikely to take place, in spite of the slightly lower activation energy of 3.65 eV.

4.5 CLOSING REMARKS

A combination of high-resolution techniques for structural and chemical characterization is used to compare the diffusion of Cu in single- and polycrystalline TiN layers grown by reactive magnetron sputtering under the same deposition conditions. No Cu penetration into the single-crystal barrier can be observed either by TEM or APT after an annealing treatment at 900 °C for 1 h. Theoretical studies suggest that at higher temperatures, when diffusion becomes more prominent, the stoichiometry of the TiN film will determine the prevailing atomic diffusion mechanism. This implicates a strong dependence of Cu diffusion properties on the main type of defects in the TiN(001) structure. In the slightly substoichiometric films studied in the present chapter, Cu diffusion is therefore expected to occur eventually via vacancy sites on the N sublattice.

In comparison, localized diffusion of Cu occurring along TiN columnar grain boundaries can be observed after the 900 °C annealing treatment in the polycrystalline TiN barrier. The penetration depth is non-uniform and is presumably related to the internal structure and density of the respective grain boundaries. Still, the maximum measured diffusion length is only approximately 30 nm, which is considerably smaller than in underdense polycrystalline TiN deposited at low substrate temperatures.

These results for single- and polycrystalline TiN layers highlight the importance of maintaining a dense and, as far as possible, defect-free microstructure to design reliable and efficient diffusion barriers. This can be achieved by epitaxial growth of the TiN and Cu layers on lattice-matched substrates.

References

[1] J.-E. Sundgren, Structure and properties of TiN coatings, Thin Solid Films 128 (1985) 21–44.

[2] S. Zhang, W. Zhu, TiN coating of tool steels: a review, J. Mater. Process. Technol. 39 (1993) 165–177.

[3] P.H. Mayrhofer, C. Mitterer, L. Hultman, H. Clemens, Microstructural design of hard coatings, Prog. Mater. Sci. 51 (2006) 1032–1114.

[4] R. Constantin, B. Miremad, Performance of hard coatings, made by balanced and unbalanced magnetron sputtering, for decorative applications, Surf. Coat. Technol. 120-121 (1999) 728–733.

[5] S. Piscanec, L.C. Ciacchi, E. Vesselli, G. Comelli, O. Sbaizero, S. Meriani, A. De Vita, Bioactivity of TiN-coated titanium implants, Acta Mater. 52 (2004) 1237–1245.

[6] A.E. Kaloyeros, E. Eisenbraun, Ultrathin diffusion barriers/liners for gigascale copper metallization, Annu. Rev. Mater. Sci. 30 (2000) 363–385.

[7] C. Lee, Y.-L. Kuo, The evolution of diffusion barriers in copper metallization, JOM 59 (2007) 44–49.

[8] M.B. Chamberlain, Diffusion of copper in thin TiN films, Thin Solid Films 91 (1982) 155–162.

[9] S.-K. Rha, W.-J. Lee, S.-Y. Lee, Y.-S. Hwang, Y.-J. Lee, D.-I. Kim, D.-W. Kim, S.-S. Chun, C.-O. Park, Improved TiN film as a diffusion barrier between copper and silicon, Thin Solid Films 320 (1998) 134–140.

[10] L. Djomeni, T. Mourier, S. Minoret, S. Fadloun, F. Piallat, S. Burgess, A. Price, Y. Zhou, C. Jones, D. Mathiot, S. Maitrejean, Study of low temperature MOCVD deposition of TiN barrier layer for copper diffusion in high aspect ratio through silicon vias, Microelectron. Eng. 120 (2014) 127–132.

[11] S.-K. Rha, S.-Y. Lee, W.-J. Lee, Y.-S. Hwang, C.-O. Park, D.-W. Kim, Y.-S. Lee, C.-N. Whang, Characterization of TiN barriers against Cu diffusion by capacitance–voltage measurement, J. Vac. Sci. Technol. B 16 (1998) 2019.

[12] S.-H. Kim, K.T. Nam, A. Datta, K.-B. Kim, Failure mechanism of a multilayer (TiN/Al/TiN) diffusion barrier between copper and silicon, J. Appl. Phys. 92 (2002) 5512.

[13] K.T. Nam, A. Datta, S.-H. Kim, K.-B. Kim, Improved diffusion barrier by stuffing the grain boundaries of TiN with a thin Al interlayer for Cu metallization, Appl. Phys. Lett. 79 (2001) 2549–2551.

[14] L.C. Yang, C.S. Hsu, G.S. Chen, C.C. Fu, J.M. Zuo, B.Q. Lee, Strengthening TiN diffusion barriers for Cu metallization by lightly doping Al, Appl. Phys. Lett. 87 (2005) 121911.

[15] W. Sinke, G.P.A. Frijlink, F.W. Saris, Oxygen in titanium nitride diffusion barriers, Appl. Phys. Lett. 47 (1985) 471–473.

[16] K.-C. Park, K.-B. Kim, Effect of annealing of titanium nitride on the diffusion barrier property in Cu metallization, J. Electrochem. Soc. 142 (1995) 3109–3115.

[17] A. Gupta, H. Wang, A. Kvit, G. Duscher, J. Narayan, Effect of microstructure on diffusion of copper in TiN films, J. Appl. Phys. 93 (2003) 5210–5214.

[18] M. Moriyama, T. Kawazoe, M. Tanaka, M. Murakami, Correlation between microstructure and barrier properties of TiN thin films used Cu interconnects, Thin Solid Films 416 (2002) 136–144.

[19] M. Ohring, The Materials Science of Thin Films, 1st ed., Academic Press, San Diego, 1992, p. 233.

[20] M. Ohring, The Materials Science of Thin Films, 1st ed., Academic Press, San Diego, 1992, p. 131.

[21] W.-H. Lee, Y.-L. Kuo, H.-J. Huang, C. Lee, Effect of density on the diffusion barrier property of TiN_x films between Cu and Si, Mater. Chem. Phys. 85 (2004) 444–449.

[22] D. Chen, X. Ma, Y. Wang, L. Chen, Electronic properties and bonding configuration at the TiN/MgO(001) interface, Phys. Rev. B 69 (2004) 155401.

[23] A.M. Minor, E.A. Stach, J.W. Morris, I. Petrov, In-situ nanoindentation of epitaxial TiN/MgO (001) in a transmission electron microscope, J. Electron. Mater. 32 (2003) 1023–1027.

[24] H. Ljungcrantz, M. Odén, L. Hultman, J.E. Greene, J.-E. Sundgren, Nanoindentation studies of single-crystal (001)-, (011)-, and (111)-oriented TiN layers on MgO, J. Appl. Phys. 80 (1996) 6725–6733.

[25] K. Kutschej, B. Rashkova, J. Shen, D. Edwards, C. Mitterer, G. Dehm, Experimental studies on epitaxially grown TiN and VN films, Thin Solid Films 516 (2007) 369–373.

[26] J.-E. Sundgren, B.-O. Johansson, S.-E. Karlsson, H.T.G. Hentzell, Mechanisms of reactive sputtering of titanium nitride and titanium carbide II: Morphology and structure, Thin Solid Films 105 (1983) 367–384.

[27] I. Petrov, L. Hultman, J.-E. Sundgren, J.E. Greene, Polycrystalline TiN films deposited by reactive bias magnetron sputtering: Effects of ion bombardment on resputtering rates, film composition, and microstructure, J. Vac. Sci. Technol. A 10 (1992) 265–272.

[28] M. Birkholz, Thin Film Analysis by X-Ray Scattering, WILEY-VCH Verlag GmbH & Co. KGaA, Weinheim, 2006, p. 150.

[29] International Centre for Diffraction Data, Powder Diffraction File 00-038-1420, 2007.

[30] International Centre for Diffraction Data, Powder Diffraction File 00-004-0836, 2007.

[31] International Centre for Diffraction Data, Powder Diffraction File 00-045-0946, 2007.

[32] M. Ohring, The materials science of thin films, 1st ed., Academic Press, San Diego, 1992, p. 316.

[33] J.W. Matthews, A.E. Blakeslee, Defects in epitaxial multilayers, J. Cryst. Growth 27 (1974) 118–125.

[34] S. Cazottes, Z.L. Zhang, R. Daniel, J.S. Chawla, D. Gall, G. Dehm, Structural characterization of a Cu/MgO(001) interface using C_S-corrected HRTEM, Thin Solid Films 519 (2010) 1662–1667.

[35] G. Abadias, Y.Y. Tse, Determination of intrinsic stresses in textured and epitaxial TiN thin films deposited by dual ion beam sputtering, Surf. Coat. Technol. 180-181 (2004) 33–40.

[36] J.-D. Kamminga, T.H. de Keijser, R. Delhez, E.J. Mittemeijer, On the origin of stress in magnetron sputtered TiN layers, J. Appl. Phys. 88 (2000) 6332–6345.

[37] L. Hultman, Thermal stability of nitride thin films, Vacuum 57 (2000) 1–30.

[38] J.A. Thornton, High rate thick film growth, Annu. Rev. Mater. Sci. 7 (1977) 239–260.

[39] D.B. Williams, C.B. Carter, Transmission electron microscopy: A textbook for materials science, Springer Science+Business Media, New York, 2009, p. 161.

[40] H. Wang, A. Tiwari, X. Zhang, A. Kvit, J. Narayan, Copper diffusion characteristics in single-crystal and polycrystalline TaN, Appl. Phys. Lett. 81 (2002) 1453–1455.

[41] L.E. Toth, Transition metal carbides and nitrides, Academic Press, New York, 1971, p. 7.

[42] P. Patsalas, C. Charitidis, S. Logothetidis, The effect of substrate temperature and biasing on the mechanical properties and structure of sputtered titanium nitride thin films, Surf. Coat. Technol. 125 (2000) 335–340.

[43] C. V. Thompson, Solid-state dewetting of thin films, Annu. Rev. Mater. Res. 42 (2012) 399–434.

[44] J. Yu, J. Bian, L. Jiang, Y. Qiu, W. Duan, F. Meng, Z. Liu, Tungsten-doped indium oxide thin film as an effective high-temperature copper diffusion barrier, ECS Solid State Lett. 3 (2014) N15–N17.

[45] D. Gupta, Diffusion Processes in Advanced Technological Materials, William Andrew Publishing, Norwich, NY, 2005, p. 4.

[46] D.B. Williams, C.B. Carter, Transmission electron microscopy: A textbook for materials science, Springer Science+Business Media, New York, 2009, p. 616.

[47] L. Hultman, J.-E. Sundgren, L.C. Markert, J.E. Greene, Ar and excess N incorporation in epitaxial TiN films grown by reactive bias sputtering in mixed Ar/N_2 and pure N_2 discharges, J. Vac. Sci. Technol. A 7 (1989) 1187–1193.

[48] J.-E. Sundgren, B.-O. Johansson, S.-E. Karlsson, Mechanisms of reactive sputtering of titanium nitride and titanium carbide I: Influence of process parameters on film composition, Thin Solid Films 105 (1983) 353–366.

[49] M. Mühlbacher, F. Mendez-Martin, B. Sartory, N. Schalk, J. Keckes, J. Lu, L. Hultman, C. Mitterer, Copper diffusion into single-crystalline TiN studied by transmission electron microscopy and atom probe tomography, Thin Solid Films 574 (2015) 103–109.

[50] J.P. Schaffer, Defects in hard coatings studied by positron annihilation spectroscopy and x-ray diffraction, J. Vac. Sci. Technol. A 10 (1992) 193.

[51] L. Tsetseris, N. Kalfagiannis, S. Logothetidis, S. Pantelides, Trapping and release of impurities in TiN: A first-principles study, Phys. Rev. B 78 (2008) 094111.

[52] D. Gupta, Diffusion Processes in Advanced Technological Materials, William Andrew Publishing, Norwich, NY, 2005, p. 46.

[53] R.E. Hoffman, Anisotropy of grain boundary self-diffusion, Acta Metall. 4 (1956) 97–98.

[54] M. Murakami, D. DeFontaine, X-ray diffraction study of interdiffusion in bimetallic Ag/Cu thin films, J. Appl. Phys. 47 (1976) 2857–2861.

[55] A. Einstein, Investigations on the theory of the Brownian movement, Dover Publications, Inc., Mineola, NY, 1956, p. 17.

[56] L. Tsetseris, S. Logothetidis, S.T. Pantelides, Migration of species in a prototype diffusion barrier: Cu, O, and H in TiN, Appl. Phys. Lett. 94 (2009) 161903.

[57] M. Mühlbacher, A.S. Bochkarev, F. Mendez-Martin, B. Sartory, L. Chitu, M.N. Popov, P. Puschnig, J. Spitaler, H. Ding, N. Schalk, J. Lu, L. Hultman, C. Mitterer, Cu diffusion in single-crystal and polycrystalline TiN barrier layers: A high-resolution experimental study supported by first-principles calculations, J. Appl. Phys. 118 (2015) 085307.

[58] A.D. Le Claire, Solute diffusion in dilute alloys, J. Nucl. Mater. 69-70 (1978) 70–96.

[59] H. Eyring, The Activated Complex in Chemical Reactions, J. Chem. Phys. 3 (1935) 107–115.

[60] K. Aigner, W. Lengauer, D. Rafaja, P. Ettmayer, Lattice parameters and thermal expansion of $Ti(C_xN_{1-x})$, $Zr(C_xN_{1-x})$, $Hf(C_xN_{1-x})$ and TiN_{1-x} from 298 to 1473 K as investigated by high-temperature X-ray diffraction, J. Alloys Compd. 215 (1994) 121–126.

[61] J.R. Manning, Correlation factors for impurity diffusion. bcc, diamond, and fcc structures, Phys. Rev. 136 (1964) A1758–A1766.

CHAPTER 5

TiN DIFFUSION BARRIER FAILURE BY THE FORMATION OF Cu_3Si

5.1 FUNDAMENTALS

Recent progress in ultra large scale integration and accompanying device miniaturization in microelectronics has sparked renewed interest in diffusion barrier materials, which are employed to separate the metallization from the underlying substrate in integrated circuits [1–4]. To evaluate the performance of diffusion barriers in an experimental setup, model systems consisting of a substrate (most commonly Si), the barrier layer and the metallization are thermally loaded to induce diffusion of atoms through the barrier. This is usually achieved by rapid thermal annealing [5–8] or conventional vacuum annealing [3,9–11]. The breakdown of the barrier layer can then be defined as the annealing temperature and time after which a specific compound is formed by constituents of the metallization and the substrate material. This indicates that either a significant amount of atoms from the metallization has diffused through the barrier to the substrate or vice versa.

Since Cu has largely replaced Al as the prevalent metallization material in Si-based devices [1,3,6,12,13], many studies [3,5,6,11,12,14–19] take the formation of the η''-Cu_3Si phase (i.e., the equilibrium phase at room temperature [20,21]) as a benchmark in evaluating barrier performance. This silicide phase can be detected by XRD measurements of the film stack, where characteristic reflections corresponding to η''-Cu_3Si are observable [3,6,11,14,15,17,18]. Increased sheet resistivity of the Cu metallization layer as measured by a FPP setup also points towards the presence of the high-resistivity η''-Cu_3Si, signifying contact failure [3,6,14,15,18]. Reports on cross-sectional electron microscopy investigations show that the formation and growth of Cu_3Si originates from localized sites at the Si/diffusion barrier interface [3,5,9,11,18], and that it grows with an epitaxial relationship to the Si substrate [22,23]. Elemental depth profiling (e.g., by Auger electron spectroscopy or X-ray photoelectron spectroscopy) correspondingly reveals a smearing of the interface regions after high-temperature annealing treatments, consistent with progressive interdiffusion between the layers in the stack [3,12,15,24,25].

However, the methods described above only allow for a very general characterization of the barrier performance, mostly focusing on the impact of barrier failure on properties of the layer stack, rather than on changes in the elemental composition of the barrier layer itself. The study summarized in this chapter aims to complement these observations with more detailed high-resolution elemental investigations performed by APT. It presents a systematic examination of a model layer stack, consisting of a Cu metallization on a magnetron sputtered polycrystalline TiN diffusion barrier grown on a single-crystal Si(001) substrate. Pristine and annealed stacks are characterized by established techniques such as XRD, FPP sheet resistivity measurements, SEM, and EDX profiling in conjunction with state-of-the-art APT analyses. APT samples are prepared site-specifically with the help of a FIB workstation [26]. In contrast to conventional depth profiling methods, where a larger sample area is analyzed, APT therefore allows to distinguish between different regions of interest in the diffusion barrier layer. This approach offers further insights into barrier performance and provides a more complete picture of the ultimate failure mechanisms.

5.2 MICROSTRUCTURE AND SHEET RESISTIVITY MEASUREMENTS

Fig. 33 shows XRD patterns of the Cu/TiN stacks in pristine state and after 1 h vacuum annealing treatments at 600, 700, 800, and 900 °C. The pristine sample exhibits reflections from the Cu and TiN layers [27,28]. As a result of Cu grain growth, Cu peaks become progressively sharper in samples annealed at higher temperatures. The first appearance of the Cu_3Si phase comes after annealing at 700 °C, with the two main peaks at 44.6 and 45.0° consistent with η''-Cu_3Si [29]. This indicates the onset of TiN barrier breakdown. After the annealing treatment at 800 °C, the intensity of the Cu peaks is noticeably decreased while reflections related to the Cu_3Si phase become more prominent. In the sample annealed at 900 °C, no diffraction peaks associated with the Cu layer are found anymore. Presumably, at this stage all the available Cu has fully reacted with Si from the

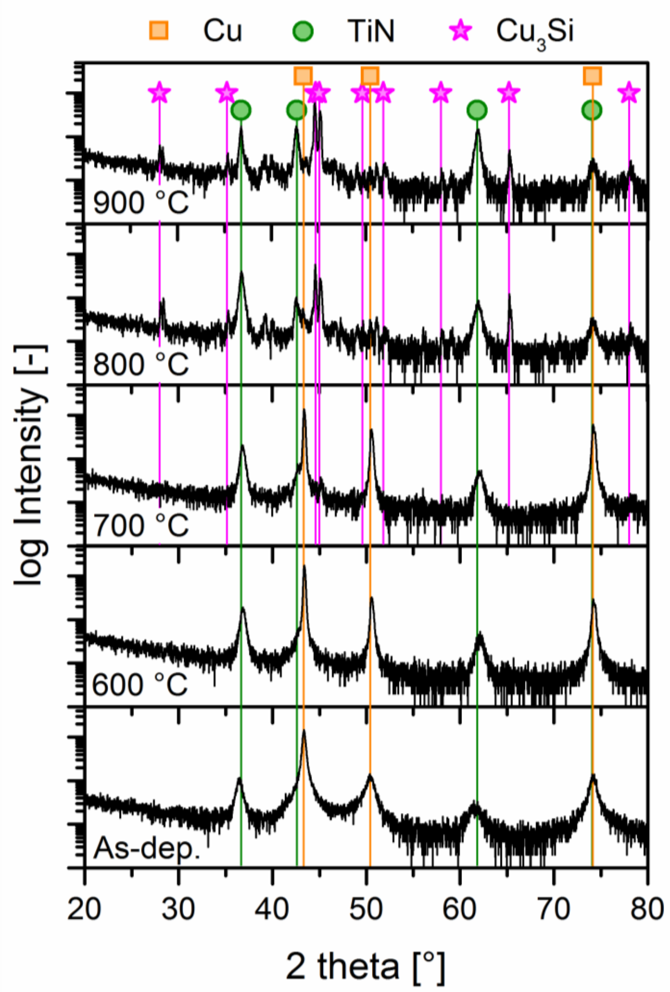

Figure 33: XRD patterns of the Cu/TiN stacks on Si in pristine state and after 1 h vacuum annealing treatments obtained in grazing incidence geometry. The Cu_3Si phase first appears after annealing at 700 °C.

underlying substrate. The microstructure of the TiN barrier layer on the other hand appears largely unaffected by the annealing treatments. Apart from a general peak sharpening linked to the reduced microstrain in annealed samples [30], where lattice faults have been annihilated, no significant changes can be observed in the corresponding reflections in the diffraction pattern.

The evolution of the Cu sheet resistivity with increasing annealing temperature is plotted in Fig. 34. FPP measurements on the pristine Cu top layer yield a resistivity of 8.89 ± 0.20 µΩ cm. Compared to the value of 1.74 µΩ cm for bulk Cu [31], this increase can be related to enhanced electron scattering at grain boundaries and the surface and interface of the thin film. For samples annealed at 600 and 700 °C, the resistivity decreases to 3.63 ± 0.15 µΩ cm as a result of defect annihilation and reduced grain boundary scattering due to Cu grain growth. Apparently, the small amount of Cu_3Si phase observed in the X-ray diffractogram of the sample annealed at 700 °C (Fig. 33) is not sufficient to cause resistivity changes measurable by FPP. However, after annealing at 800 and 900 °C, a significant rise can be observed caused by the formation of the high-resistivity silicide and elevated defect densities associated with interdiffusion damage in general. Values for these two samples are only indicated in Fig. 34, since the basic assumption of a constant Cu film thickness underlying the calculation of the resistivity does not apply anymore, judging from the diminishing Cu peak intensities in the X-ray diffractograms in Fig. 33.

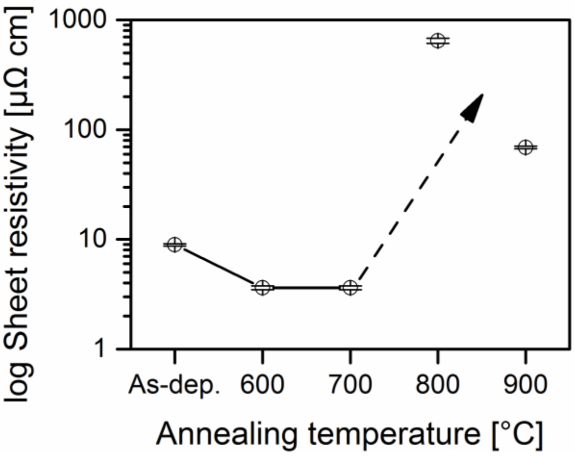

Figure 34: Evolution of the Cu sheet resistivity with increasing annealing temperature (1 h annealing time in each case) measured by FPP.

5.3. EVOLUTION OF BARRIER DAMAGE

SEM images of the sample surfaces obtained with SE and BSE detectors are plotted in Fig. 35. The pristine sputtered Cu layer exhibits growth defects in the form of hillocks and pores, related to reduced atomic mobility in sputter deposition without external substrate heating. After annealing at 600 °C, the pore size is increased. Presumably, this is one of the early stages of solid-state dewetting of Cu, which was previously observed for Cu metallization layers deposited on diffusion barriers [32]. In these two sample states, plan-view EDX area scans reveal the presence of Cu as well as low signal counts associated with Ti shooting through from the underlying TiN film. The first significant change in topography occurs after annealing at 700 °C. Already with the bare eye, the Cu layer appears duller compared to the shiny metallic surface of the pristine and the 600 °C samples. In the SEM, the formation of small hillocks with diameters around 3 µm is evident. In addition, some bigger hillocks (Ø 6-7 µm) are present, and the area around these is depleted of the smaller surface defects. Since BSE images show contrast differences, in addition to EDX area scans, measurements are also performed locally at large hillocks. Signals obtained from the area scan are comparable to results of the pristine and 600 °C samples, showing only Cu and minimal amounts of Ti. On the other hand, the local measurement at the hillock in the center of the BSE micrograph of the 700 °C sample (Fig. 35) yields signals related to Si in addition to Cu, while Ti counts drop. This indicates that Si or a Si-containing phase is present in the Cu/TiN layer stack after the annealing treatment at 700 °C, presumably due to localized diffusion. After annealing treatments at even higher temperatures of 800 and 900 °C, dramatic changes are apparent and several new features are visible on the sample surface. In plan-view SEM micrographs, the 800 °C sample exhibits a discontinuous surface layer in the form of bump- or slug-like features with sizes in the 50-100 µm range (Fig. 35). Qualitative EDX analysis shows that these features are composed of Si and Cu. Furthermore, EDX reveals the underlying film displayed with the dark contrast in the BSE micrograph to be the original TiN barrier layer. A crack network is visible in this film. The most striking features, however, are rectangular, cracked structures in the TiN layer, showing a slightly brighter contrast in the BSE image. The longer side of the biggest rectangles is around 50 µm. These structures have been associated with the formation of the Cu_3Si phase [3,11,18,19,33–35]. This is also corroborated by the local EDX measurements at hand, which yield Cu, Ti, and Si signals. After annealing at 900 °C the size of the bump- and slug-like features is increased, while their population density has decreased. Additionally, the rectangular structures have grown in size and number. Most of them are broken open and filled with a material containing Cu and Si, while others resemble empty indents. These empty features have an inverse pyramid shape with a rectangular base (see samples annealed at 900 °C in Fig. 35), with Si{111} faceting into the substrate, as shown below.

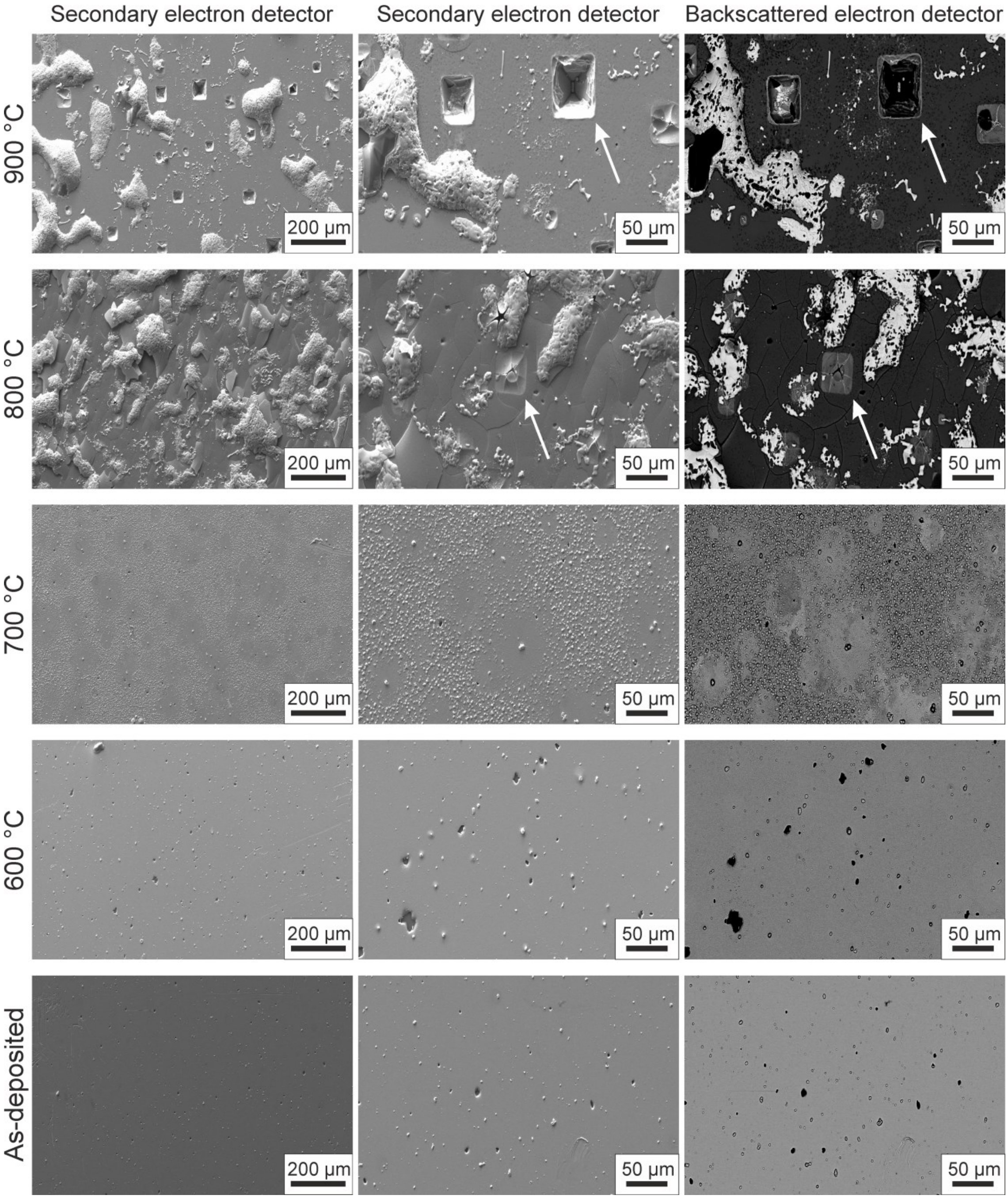

Figure 35: Plan-view SEM images obtained with a SE and a BSE detector systematically showing the surface evolution from the pristine sample to the sample annealed at 900 °C. Rectangular features associated with the epitaxial growth of the Cu_3Si phase in Si(001) are exemplarily marked by arrows in samples annealed at 800 and 900 °C.

To confirm the local formation of the Cu_3Si phase as the prevailing damaging mechanism of the diffusion barrier, EDX line profiles are acquired and superimposed on SEM micrographs of FIB cross-sections. Results are plotted in Fig. 36. The line profile direction is indicated by the arrow. Exact quantification of the chemical composition of the TiN layer is not possible by EDX because of an irresolvable energy overlap between the Ti-L and N-K edges, the Ti-L and O-K edges and the N-K and C-K edges, respectively. Generally heightened C contents are a by-product of the protective Pt deposition prior to FIB cutting. Figs. 36 (a,b) show the intact Cu/TiN bilayer stack on Si in the as-deposited and 600 °C annealed states. Some pores (marked by dashed ovals in Fig. 36 (a)) are visible at the pristine Cu/TiN interface, which can be related to insufficient ad-atom mobility during deposition without external substrate heating. After annealing at 600 °C, pores (marked by dashed ovals in Fig. 36 (b)) are also evident at grain boundaries within the Cu layer, indicating an early stage of solid state de-wetting [36]. In both cases, no intermixing or diffusion across the interfaces is observable. On the other hand, the cross-sectional cut performed at one of the hillocks in the 700 °C sample (Fig. 36 (c)) reveals localized terminal barrier failure. The EDX line scan shows that Cu is diffusing through the TiN

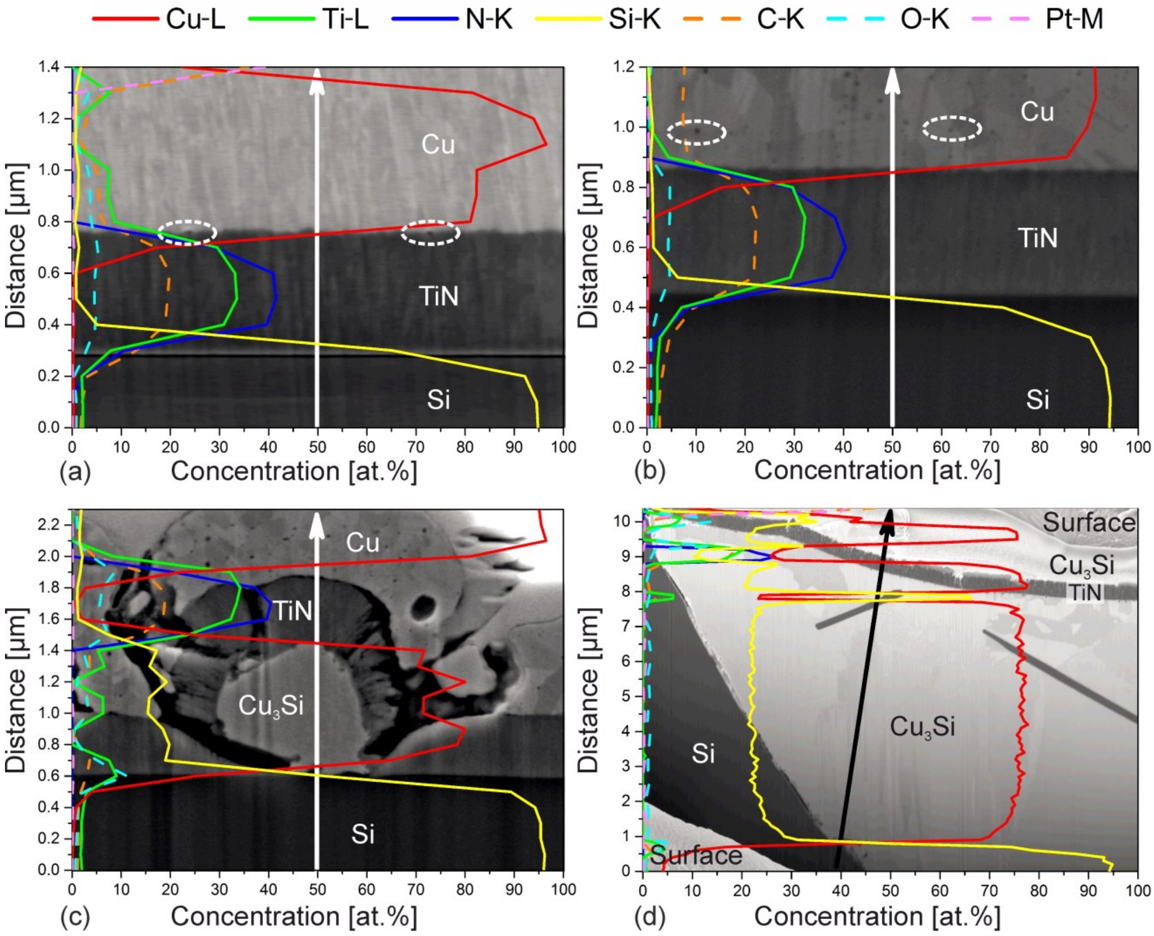

Figure 36: Cross-sectional EDX line profiles obtained from FIB cuts of the sample (a) in the as-deposited state, (b) annealed at 600 °C, (c) at 700 °C, and (d) at 900 °C for 1 h. In (a) and (b) pores are marked exemplarily by dashed ovals.

film to form a compound with Si from the substrate. The elemental concentration suggests formation of the Cu_3Si phase, which has an orthorhombic unit cell and crystallizes in a two-dimensional long-period superstructure [21,22]. Growth of Cu_3Si at the TiN/Si interface is accompanied by a significant volume expansion, since the η''-Cu_3Si phase has a molecular volume of 46 Å^3, compared to 20 Å^3 for pure Si [37]. To accommodate the silicide, the TiN barrier layer is lifted from the substrate. Thereby, the layer cracks perpendicular to the interfaces along grain boundaries, which provide the fast diffusion paths for Cu. The volume expansion associated with the silicide formation leads to the appearance of the hillocks found for the sample annealed at 700 °C in plan-view SEM in Fig. 35. If annealed at higher temperatures of 800 or 900 °C, when enough diffused Cu is available, the η''-Cu_3Si phase proceeds to grow in a characteristic {111} faceted fashion into the Si substrate. This is further illustrated in Fig. 36 (d) with an inclined view on a FIB cut performed into one of the filled rectangular features in the sample annealed at 900 °C. In the lower left and upper right corner of Fig. 36 (d) the sample surface is visible. The cross-section shows the Si substrate with dark contrast and the silicide compound grown into the Si crystal. EDX reveals the compound to be composed of 25 at.% Si and 75 at.% Cu, confirming the presence of the η''-Cu_3Si phase known to generally form [3,5,6,11,12,14–19]. The plate-like precipitates visible in the compound are suspected to be Ti silicides. However, their exact composition could not be determined by EDX. The original TiN layer is still visible running through the upper part of the Cu silicide. Boundaries between the columnar grains are cracked and serve to provide diffusion paths. The sample surface is also partly covered with the Cu_3Si compound, visible as the bright phase in Fig. 35. Apparently, after diffusion through the barrier and nucleation at the TiN/Si interface, when enough Cu is available, the growth of the Cu_3Si grains into the (001)-oriented Si crystal proceeds regardless of the presence of a barrier layer along the close packed <101> directions as described by Weber *et al.* [22]. This is illustrated in Fig. 37 for the sample annealed at 900 °C. The angle between the sample surface and the boundary of the Si substrate and the formed Cu_3Si is measured to be around 55°, which corresponds to the angle of 54.7° between the {100} and {111} plane families in cubic systems (Figs. 37 (a,b)). A schematic sketch of the geometric relationship adapted from Ref. [22] is presented in Fig. 37 (c).

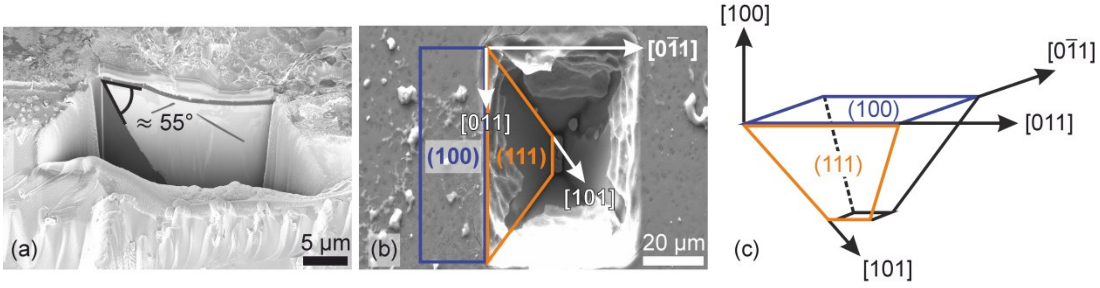

Figure 37: SEM images illustrating the growth of Cu_3Si after barrier failure in a Cu/TiN/Si(001) stack annealed at 900 °C for 1 h in (a) inclined cross-sectional and (b) top view. A schematic representation of the geometric relationship between the Cu_3Si and the Si crystals adapted from Ref. [22] is shown in (c).

While the localized failure of the TiN barrier by the formation of Cu_3Si is easily documented by diffraction and electron microscopy techniques, the question remains if and how diffusion becomes manifest in areas that appear intact in SEM micrographs. To this end, APT samples are prepared by a conventional FIB lift-out procedure [38] site-specifically at regions free of hillocks in the sample annealed at 700 °C for 1h. At the given measurement parameters, Cu ions appear as $^{63}Cu^+$ and $^{65}Cu^+$ in the mass spectra, while TiN is detected in the form of doubly charged molecular ions with isotopes at 30, 30.5, 31, 31.5, and 32 amu, thus avoiding a peak overlap. Because of the excellent mass resolution of APT, additionally also the peaks related to Si^{2+} and N^+ and Si^+ and N_2^+ ions can be separated, exemplarily shown in the detail of the mass spectrum in Fig. 38 (a). This allows for the accurate visualization of the Si and Cu distribution in the 3D reconstructions of the original Cu/TiN interface presented in Figs. 38 (b-e). Measured ions (Cu, molecular TiN, Si, N, and Ti) are plotted as data points in Fig. 38 (b). Fig. 38 (c) shows the same sample volume rotated 180° around the z-axis. The presence of Cu as well as Si ions inside the TiN layer is noteworthy. Isoconcentration surfaces give information about local elemental concentrations in different sample regions. Fig. 38 (d) shows the tip (orientation as in Fig. 38 (b)) with isoconcentration surfaces enclosing volumes of Cu concentrations higher than 50 at.% in orange, while Fig. 38 (e) shows volumes of Si concentrations higher than 10 at.% in violet. While the overall Si concentration in the TiN layer is below 10 at.%, the interface is enriched in Si. Furthermore, there is a pronounced and correlated accumulation of Cu and Si ions at the far right region in Figs. 38 (d,e). Several conclusions can be drawn from this measurement: *(i)* Cu diffusion preferentially occurs locally at fast diffusion paths. These could be porous grain boundaries, triple junctions or pinholes in the barrier layer. This is in good agreement with SEM results, where the sample annealed at 700 °C shows the local formation of Cu_3Si at the TiN/Si interface (Fig. 36 (c)). It is plausible that the local migration of Cu through the TiN layer captured in the APT sample shown in Fig. 38 represents an initial stage of this process. *(ii)* Si is present throughout the TiN barrier, but segregates at the Cu/TiN interface and at Cu-rich regions in the TiN film. This observation is consistent with the appearance of Cu and Si-rich discontinuous surface features on the TiN barrier as imaged by SEM in samples annealed at 800 and 900 °C (Fig. 35). Therefore, APT measurements suggest that two different diffusion processes are active in TiN barriers sputter deposited without external substrate heating. Cu is predominantly diffusing along fast diffusion paths in the TiN layer to form the Cu_3Si phase, which grows epitaxially from the TiN/Si interface into the Si substrate. *(iii)* Concurrently, small amounts of Si are also diffusing upwards through the TiN film to eventually form the Cu_3Si compound on the sample surface. In this case, APT measurements point towards a lattice diffusion mechanism, as Si is found to be distributed throughout the TiN layer.

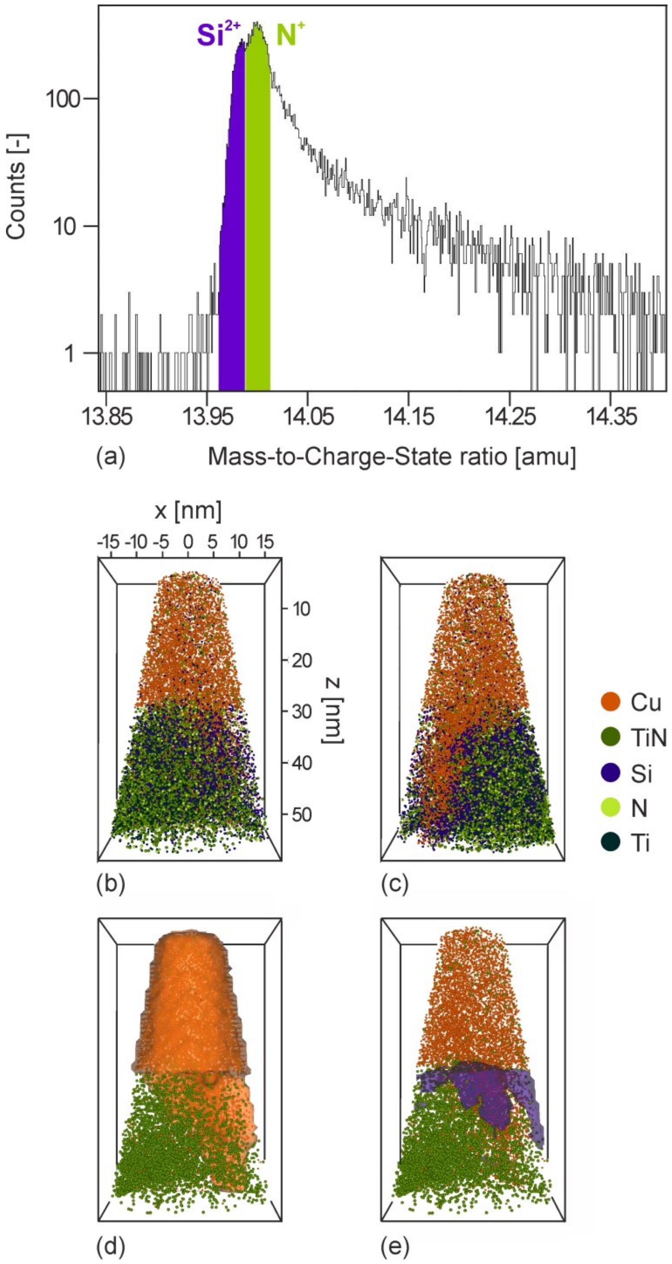

Figure 38: (a) Detail of a mass spectrum depicting the separate Si^{2+} and N^{+} peaks after measuring the Cu/TiN/Si stack annealed at 700 °C for 1 h. The 3D reconstruction of the accordingly evaluated sample is shown in (b) and rotated 180° around the z-axis in (c). An isoconcentration surface enclosing the sample volume with a Cu concentration higher than 50 at.% is colored orange in (d), while the isoconcentration surface enclosing the sample volume with a Si concentration higher than 10 at.% is displayed in violet in (e).

5.4 CLOSING REMARKS

A systematic investigation of diffusion barrier failure in a model Cu/TiN/Si(001) stack is presented. Combining results obtained by XRD, FPP sheet resistivity measurements, SEM, EDX profiling, and APT, two mechanisms leading to barrier breakdown are identified. On the one hand, diffusion of Cu along fast diffusion paths such as grain boundaries, triple junctions or pinholes results in the formation of the η''-Cu_3Si phase. This phase nucleates at the TiN/Si interface, incorporating diffused Cu atoms and Si atoms from the substrate, and subsequently grows under volume expansion. The original barrier layer is thus locally lifted from the substrate, leading to the appearance of hillocks on the surface of the sample annealed at 700 °C for 1 h. At higher annealing temperatures of 800 and 900 °C, the Cu_3Si compound proceeds to grow in a characteristic epitaxial fashion along the close-packed <101> directions onto {111} facets into the single-crystal Si(001) substrate, regardless of the presence of the TiN barrier layer. The present atom probe analyses further reveal the diffusion of Si through the TiN barrier towards the Cu top layer already active in the sample annealed at 700 °C. Since Si is found distributed throughout the TiN film, a lattice diffusion mechanism is inferred. Subsequent segregation of Si to Cu-rich regions such as the Cu/TiN interface, but also to preferred Cu diffusion paths in the TiN layer, explains the presence of the Cu_3Si phase on top of the barrier after annealing at 800 and 900 °C. Thus, the failure of polycrystalline TiN diffusion barriers deposited without external substrate heating not only occurs by the local formation of Cu_3Si at the barrier/substrate interface, but also by lattice diffusion of Si atoms from the substrate, resulting in the replacement of the original Cu top layer by a discontinuous film composed of Cu and Si.

References

[1] A.E. Kaloyeros, E. Eisenbraun, Ultrathin diffusion barriers/liners for gigascale copper metallization, Annu. Rev. Mater. Sci. 30 (2000) 363–385.

[2] R.A. Araujo, X. Zhang, H. Wang, Epitaxial cubic HfN diffusion barriers deposited on Si (001) by using a TiN buffer layer, J. Vac. Sci. Technol. B 26 (2008) 1871.

[3] C. Lee, Y.-L. Kuo, The evolution of diffusion barriers in copper metallization, JOM 59 (2007) 44–49.

[4] Y. Meng, Z.X. Song, J.H. Chen, F. Ma, Y.H. Li, J.F. Wang, C.C. Wang, K.W. Xu, Ultrathin ZrB_xO_y films as diffusion barriers in Cu interconnects, Vacuum 119 (2015) 1–6.

[5] S.H. Hsieh, C.M. Chien, W.L. Liu, W.J. Chen, Failure behavior of ITO diffusion barrier between electroplating Cu and Si substrate annealed in a low vacuum, Appl. Surf. Sci. 255 (2009) 7357–7360.

[6] J. Sommer, C. Herzig, Direct determination of grain-boundary and dislocation self-diffusion coefficients in silver from experiments in type-C kinetics, J. Appl. Phys. 72 (1992) 2758.

[7] Q. Lin, W. Jing, S. Yang, Z. Jiang, C. Wang, Agglomeration and dendritic growth of Cu/Ti/Si thin film, J. Nanomater. 2014 (2014) 1–8.

[8] L.C. Yang, C.S. Hsu, G.S. Chen, C.C. Fu, J.M. Zuo, B.Q. Lee, Strengthening TiN diffusion barriers for Cu metallization by lightly doping Al, Appl. Phys. Lett. 87 (2005) 121911.

[9] M.H. Tsai, S.C. Sun, C.E. Tsai, S.H. Chuang, H.T. Chiu, Comparison of the diffusion barrier properties of chemical-vapor-deposited TaN and sputtered TaN between Cu and Si, J. Appl. Phys. 79 (1996) 6932–6938.

[10] T. Laurila, K. Zeng, J.K. Kivilahti, J. Molarius, I. Suni, Failure mechanism of Ta diffusion barrier between Cu and Si, J. Appl. Phys. 88 (2000) 3377.

[11] S.-H. Kim, K.T. Nam, A. Datta, K. Kim, Failure mechanism of a multilayer (TiN/Al/TiN) diffusion barrier between copper and silicon, J. Appl. Phys. 92 (2002) 5512.

[12] Y.M. Zhou, M.Z. He, Z. Xie, Diffusion barrier performance of novel Ti/TaN double layers for Cu metallization, Appl. Surf. Sci. 315 (2014) 353–359.

[13] J. Baumann, T. Werner, M. Rennau, C. Kaufmann, T. Gessner, TiN diffusion barriers for copper metallization, Microelectron. Eng. 37/38 (1997) 221–228.

[14] J.T. No, J.H. O, C. Lee, Evaluation of Ti-Si-N as a diffusion barrier between copper and silicon, Mater. Chem. Phys. 63 (2000) 44–49.

[15] Y. Wang, C. Zhao, Z. Song, F. Cao, D. Yang, Effect of substrate bias voltages on the diffusion barrier properties of Zr-N films in Cu metallization, Appl. Surf. Sci. 253 (2007) 8858–8862.

[16] K.-L. Ou, M.-H. Tsai, H.-M. Huang, S.-Y. Chiou, C.-T. Lin, S.-Y. Lee, Interfacial reactions and electrical properties of hafnium-based thin films in Cu/barrier/n^+–p junction diodes, Microelectron. Eng. 77 (2005) 184–192.

[17] M. Moriyama, T. Kawazoe, M. Tanaka, M. Murakami, Correlation between microstructure and barrier properties of TiN thin films used Cu interconnects, Thin Solid Films 416 (2002) 136–144.

[18] W.-H. Lee, Y.-L. Kuo, H.-J. Huang, C. Lee, Effect of density on the diffusion barrier property of TiN_x films between Cu and Si, Mater. Chem. Phys. 85 (2004) 444–449.

[19] Y.-L. Kuo, J.-J. Huang, S.-T. Lin, C. Lee, W.-H. Lee, Diffusion barrier properties of sputtered TaN_x between Cu and Si using TaN as the target, Mater. Chem. Phys. 80 (2003) 690–695.

[20] Z. Zhang, L.M. Wong, H.G. Ong, X.J. Wang, J.L. Wang, S.J. Wang, H. Chen, T. Wu, Self-assembled shape- and orientation-controlled synthesis of nanoscale Cu_3Si triangles, squares, and wires, Nano Lett. 8 (2008) 3205–10.

[21] J.K. Solberg, The crystal structure of η-Cu_3Si precipitates in silicon, Acta Crystallogr. Sect. A 34 (1978) 684–698.

[22] G. Weber, B. Gillot, P. Barret, Interfaces structure in relation with the mechanisms in the reaction copper-silicon, Phys. Status Solidi 75 (1983) 567–576.

[23] J. Echigoya, H. Enoki, T. Satoh, T. Waki, T. Ohmi, M. Otsuki, T. Shibata, Thin film reaction and interface structure of Cu on Si, Appl. Surf. Sci. 56-58 (1992) 463–468.

[24] S.-Y. Chang, D.-S. Chen, 10-nm-thick quinary (AlCrTaTiZr)N film as effective diffusion barrier for Cu interconnects at 900 °C, Appl. Phys. Lett. 94 (2009) 231909.

[25] S.-K. Rha, W.-J. Lee, S.-Y. Lee, D.-W. Kim, C.-O. Park, S.-S. Chun, Interdiffusions and reactions in Cu/TiN/Ti/Si and Cu/TiN/Ti/SiO_2/Si multilayer structures, J. Mater. Res. 12 (2011) 3367–3372.

[26] K. Thompson, D. Lawrence, D.J. Larson, J.D. Olson, T.F. Kelly, B. Gorman, *In situ* site-specific specimen preparation for atom probe tomography, Ultramicroscopy 107 (2007) 131–139.

[27] International Centre for Diffraction Data, Powder Diffraction File 00-004-0836, 2007.

[28] International Centre for Diffraction Data, Powder Diffraction File 00-038-1420, 2007.

[29] International Centre for Diffraction Data, Powder Diffraction File 00-051-0916, 2007.

[30] M. Birkholz, Thin Film Analysis by X-Ray Scattering, WILEY-VCH Verlag GmbH & Co. KGaA, Weinheim, 2006.

[31] W. Martienssen, H. Warlimont, eds., Springer Handbook of Condensed Matter and Materials Data, Springer Berlin Heidelberg, 2005.

[32] J. Yu, J. Bian, L. Jiang, Y. Qiu, W. Duan, F. Meng, Z. Liu, Tungsten-doped indium oxide thin film as an effective high-temperature copper diffusion barrier, ECS Solid State Lett. 3 (2014) N15–N17.

[33] N. Benouattas, A. Mosser, D. Raiser, J. Faerber, A. Bouabellou, Behaviour of copper atoms in annealed Cu/SiO_x/Si systems, Appl. Surf. Sci. 153 (2000) 79–84.

[34] N. Floquet, S. Yilmaz, J.L. Falconer, Interaction of copper catalysts and Si(100) for the direct synthesis of methylchlorosilanes, J. Catal. 148 (1994) 348–368.

[35] P. Majumder, C.G. Takoudis, Investigation on the diffusion barrier properties of sputtered Mo/W–N thin films in Cu interconnects, Appl. Phys. Lett. 91 (2007) 162108.

[36] C.V. Thompson, Solid-state dewetting of thin films, Annu. Rev. Mater. Res. 42 (2012) 399–434.

[37] A.A. Istratov, E.R. Weber, Physics of copper in silicon, J. Electrochem. Soc. 149 (2002) G21.

[38] B. Gault, M.P. Moody, J.M. Cairney, S.P. Ringer, Atom probe microscopy, Springer Science+Business Media, New York, 2012.

CHAPTER 6

IMPROVEMENT OF TiN DIFFUSION BARRIERS BY BOMBARDMENT WITH Ta IONS

6.1 FUNDAMENTALS

Diffusion barriers are a vital component in integrated circuits (ICs), where they separate the Cu metallization from the adjacent SiO_2 dielectrics and the Si substrate [1,2]. Barrier failure and the diffusion of Cu leads to the formation of Cu-silicides, which severely impair device performance and lifetime [1,3,4]. Since diffusion is a thermally activated process, a thermally stable microstructure is of vital interest for efficient diffusion barrier layers. Their electrical conductivity ideally should be similar to the one of Cu (1.74 μΩ cm for bulk Cu [5]) to optimize device functionality [6]. Transition metal nitrides are a material group fulfilling these requirements. In particular, TiN is a well-suited barrier material, since its excellent structural and thermal stability is combined with an electrical resistivity as low as 20-25 μΩ cm for the pure polycrystalline film [7].

However, the challenge lies in producing dense and defect-free TiN films, so as not to provide fast diffusion paths for the Cu atoms. Sputter-deposited TiN grows with a columnar morphology on Si and its native oxide, with grain boundaries as direct diffusion pathways running from the metallization to the underlying substrate [7,8]. In Al-metallization schemes, effective stuffing of these grain boundaries by exposure to oxygen and the subsequent formation of Al-oxides at the boundary region has been achieved [9–12]. Yet, a major drawback of this approach is the accompanying resistivity increase in the TiN layer [6].

Chapter 4 of this thesis demonstrates sputter deposition of a dense columnar TiN barrier on Si at a substrate temperature of 700 °C and a bias voltage of -100 V, resulting in sufficient ad-atom mobility to maintain a microstructure devoid of intercrystalline porosity. This barrier shows only limited Cu diffusion after annealing at 900 °C for 1 h [13]. However, manufacturers in semiconductor industry are often restricted to low-temperature processing routes. A recent innovation by Greczynski *et al.* is a hybrid high-power impulse/direct current magnetron sputter (HIPIMS/DCMS) process capable of producing dense $Ti_{1-x}Ta_xN$ films with Ta contents of $x = 0.08\text{-}0.16$ without external substrate heating [14]. Densification is achieved by bombardment of the growing film with energetic, heavy Ta ions sputter-ejected from a Ta target operated in HIPIMS mode. In addition, a pulsed substrate bias is applied synchronously with the HIPIMS pulses. This results in the growth of dense, dilute $Ti_{1-x}Ta_xN$ coatings. The solid solution with rock salt structure is stable up to $x = 0.75$ [15]. This new process could be the missing link between the low-temperature processing needs of IC manufacturers and the requirement of a dense microstructure in diffusion barriers.

In this chapter, a comparative study of the diffusion barrier performance of a conventional DCMS TiN film (subsequently referred to as TiN-DC) and a hybrid HIPIMS/DCMS $Ti_{0.84}Ta_{0.16}N$ film (subsequently referred to as $Ti_{0.84}Ta_{0.16}N$-HIP) deposited on Si substrates without external substrate heating is presented. A combination of SEM, XRD, and FPP sheet resistivity measurements is employed to study the topographical and microstructural evolution of the barriers after annealing treatments in a temperature range of 700-900 °C. The interdiffusion damage in the Cu metallization/barrier layer stacks is investigated by TEM in conjunction with EDX.

6.2 TOPOGRAPHICAL AND MICROSTRUCTURAL EVOLUTION

Fig. 39 displays plan-view SEM images of the Cu/TiN-DC and Cu/$Ti_{0.84}Ta_{0.16}N$-HIP layer stacks in pristine state and after 1 h annealing treatments at 700 and 900 °C. The topography of both as-deposited samples is similar and shows the continuous Cu top layers with an average roughness R_a of 6.38 nm on TiN-DC and 6.08 nm on $Ti_{0.84}Ta_{0.16}N$-HIP. After annealing at 700 °C, the Cu film grown on TiN-DC is already cracked due to hillocks penetrating the film from beneath. In contrast, the Cu layer deposited on $Ti_{0.84}Ta_{0.16}N$-HIP is intact, but exhibits abnormal grain growth as a result of the anisotropy of surface energies and

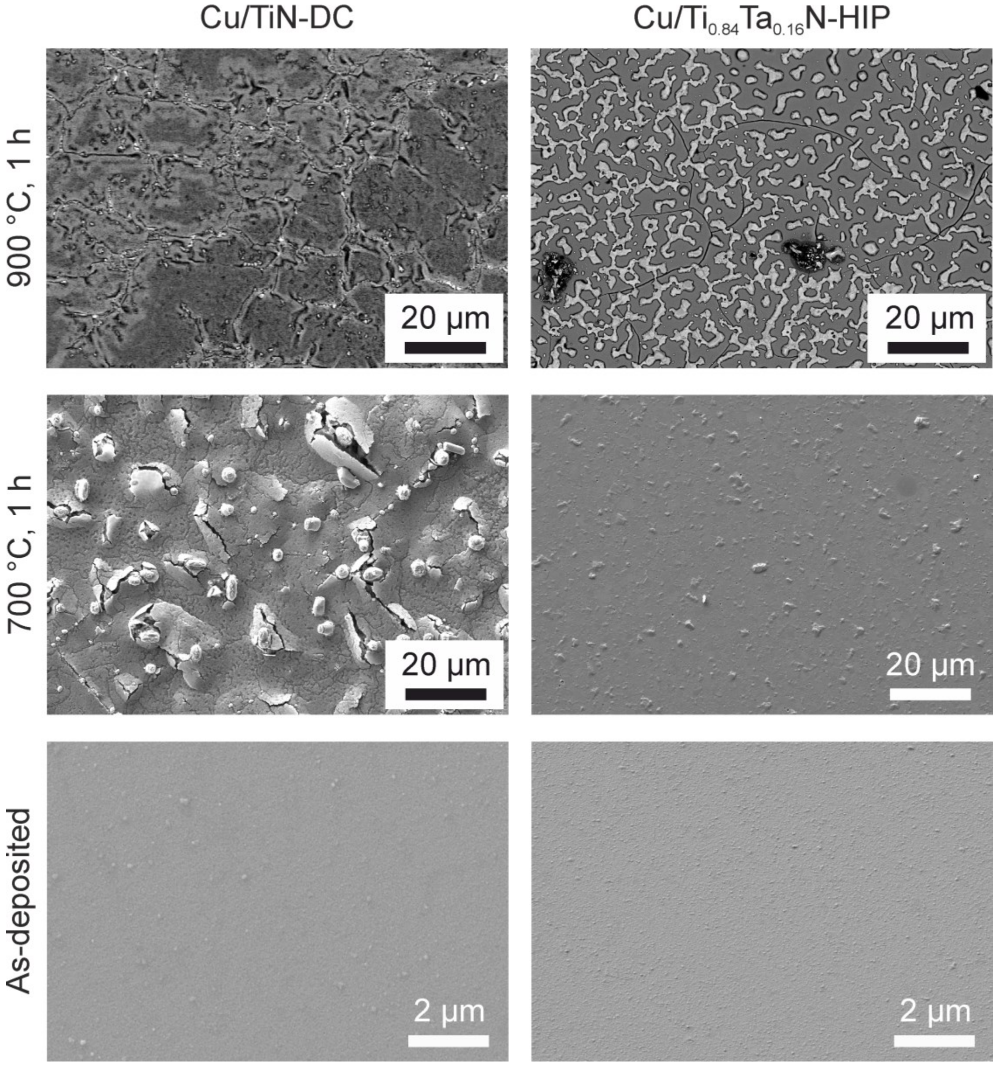

Figure 39: Plan-view SEM micrographs of the pristine and annealed Cu/TiN-DC and Cu/$Ti_{0.84}Ta_{0.16}N$-HIP bilayer stacks illustrating their topographical evolution. Images of as-deposited and 700 °C annealed samples are obtained with a secondary electron detector, images of the 900 °C annealed samples with a backscattered electron detector.

elastic constants in Cu [16]. This anisotropy is also responsible for the subsequent development of Cu islands by solid-state de-wetting as observed in the Cu/$Ti_{0.84}Ta_{0.16}$N-HIP sample annealed at 900 °C, where a Cu island network is visible on the $Ti_{0.84}Ta_{0.16}$N-HIP surface [17]. Furthermore, cracks and isolated defects with a darker contrast are evident in the 900 °C annealed $Ti_{0.84}Ta_{0.16}$N-HIP film. The same applies for the 900 °C annealed TiN-DC sample, but in this case the cracks in the TiN layer are more pronounced and partially filled with a phase yielding brighter contrast, presumably Cu in metallic or compound form.

XRD investigations summarized in Fig. 40 provide more information about the interdiffusion damage in the film stacks. Cu- and TiN-reflections [18,19] are observable in the pristine Cu/TiN-DC sample (Fig. 40 (a)), indicating a polycrystalline nature of both films. However, already after the annealing treatment at 700 °C additional peaks appear in the diffractogram. These can be related to the Cu_3Si phase [20], a compound often found as a reaction product due to interdiffusion in Cu metallization/barrier stacks on Si substrates [1,3,4]. Formation of Cu_3Si occurs locally under volume expansion at the barrier/Si interface [1,21,22], leading to the appearance of hillocks in the 700 °C Cu/TiN-DC sample in Fig. 39. After annealing at 900 °C, Cu peaks are hardly discernible in the diffractograms anymore, while peaks identified as Cu_3Si are very pronounced. This suggests that most of the available Cu has been consumed to form the Cu_3Si compound, confirming the SEM finding of a bare TiN surface

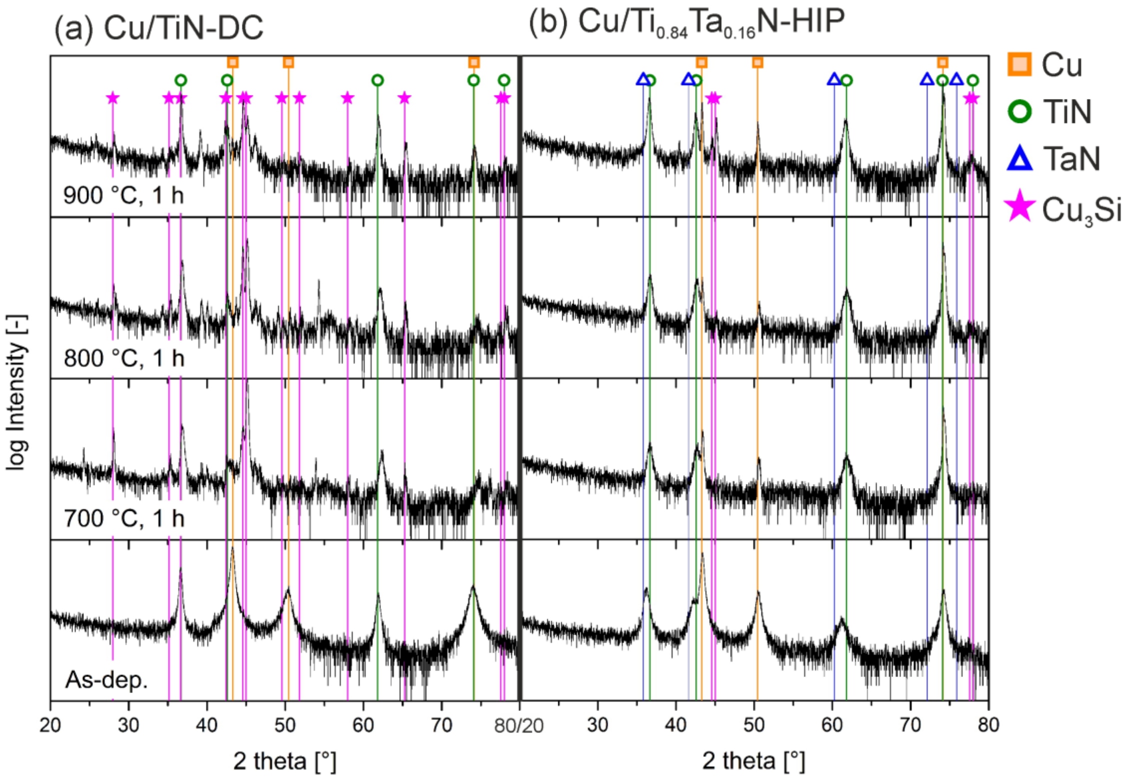

Figure 40: Evolution of XRD patterns of (a) Cu/TiN-DC and (b) Cu/$Ti_{0.84}Ta_{0.16}$N-HIP bilayers on Si(001) substrates with increasing annealing temperature measured in grazing incidence configuration.

with cracks filled with Cu_3Si as displayed in Fig. 39. Peaks related to the pristine $Ti_{0.84}Ta_{0.16}N$ layer in the diffractogram shown in Fig. 40 (b) are shifted to a position between the reflections of the binary nitrides TiN and TaN [23], indicating the formation of a solid solution with rock salt structure. Additionally, reflections from the polycrystalline Cu top layer are present in the diffraction pattern. With increasing annealing temperature, Cu peaks measured on the Cu/$Ti_{0.84}Ta_{0.16}N$-HIP samples become progressively sharper. This is consistent with the Cu grain growth observed in plan-view SEM images of these samples (Fig. 39). The $Ti_{0.84}Ta_{0.16}N$-HIP barrier is found to be stable up to 900 °C, but a peak shift towards higher 2θ values is noticeable for annealed layers. This is likely due to stress relaxation upon annealing but not further investigated within this study. The formation of Cu_3Si is retained up to 900 °C, corresponding to an improvement of 200 °C with respect to the conventional TiN-DC barrier. Presumably, the Cu diffusion originates preferentially at isolated defects such as pinholes in the $Ti_{0.84}Ta_{0.16}N$-HIP barrier and Cu then reacts with Si at the barrier/substrate interface. This explains the sporadic damage sites observed with a darker contrast in the backscattered electron SEM image of the 900 °C annealed Cu/$Ti_{0.84}Ta_{0.16}N$-HIP stack in Fig. 39.

Results of FPP sheet resistivity measurements presented in Fig. 41 are in good agreement with the preceding observations. In both pristine film stacks, the Cu top layer has an increased electrical resistivity compared to the value of 1.74 µΩ cm for bulk Cu. This is due to additional electron scattering at the film surface and interface, as well as at grain boundaries within the thin Cu film. In case of the Cu/$Ti_{0.84}Ta_{0.16}N$-HIP stacks annealed at 700 and 800 °C, Cu grain growth and defect annihilation lead to a drop in Cu sheet resistivity, which is

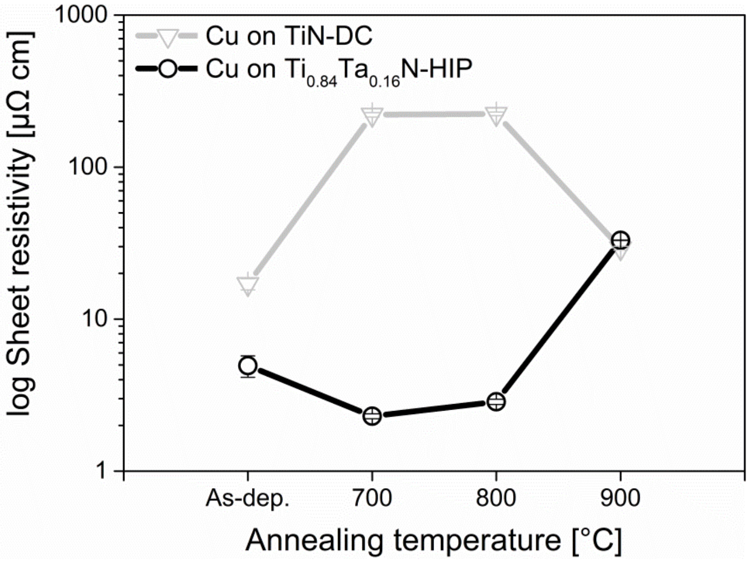

Figure 41: Evolution of the sheet resistivity of Cu on TiN-DC and $Ti_{0.84}Ta_{0.16}N$-HIP with increasing annealing temperature measured in a FPP set-up. All values are calculated under the assumption of a constant Cu film thickness of 160 nm.

approaching the bulk value. In contrast, the resistivity of Cu on TiN-DC rises above 200 µΩ cm after annealing at 700 and 800 °C, consistent with the appearance of the high-resistivity Cu_3Si phase found by SEM (Fig. 39) and XRD (Fig. 40) [24]. Sheet resistivities for both investigated layer stacks are around 30 µΩ cm after diffusion-annealing at 900 °C. This may seem puzzling at first glance, but an explanation can be given with the aid of the SEM investigations in Fig. 39. Although different mechanisms are at play, both layer stacks exhibit a mostly bare barrier surface after the 900 °C annealing treatment. The underlying reason is diffusion of Cu through the barrier in the Cu/TiN-DC stack and de-wetting of Cu in the Cu/$Ti_{0.84}Ta_{0.16}$N-HIP stack. It is apparent that instead of on the Cu top layer, the sheet resistivity is measured on the underlying barrier layers in these cases. With the barrier thicknesses instead of the Cu film thickness inserted in equation (14), sheet resistivities of 36.6 ± 1.0 and 30.9 ± 0.1 µΩ cm are obtained for the annealed and diffusion-damaged TiN-DC and the annealed $Ti_{0.84}Ta_{0.16}$N-HIP barrier, respectively.

6.3 INTERDIFFUSION DAMAGE

To further illustrate the interdiffusion damage, cross-sectional bright-field TEM and dark-field STEM images are acquired of pristine and annealed samples. Fig. 42 (a) shows the as-deposited Cu/TiN-DC bilayer arrangement on Si substrates with a native oxide layer. TiN-DC grows with a columnar microstructure, exhibiting inter- and intracolumnar voids. This is attributed to the limited surface mobility of ad-atoms during film growth at low substrate temperatures [25]. The Cu top layer initially adopts the columnar growth fashion from the TiN-DC template, but morphs into a more granular structure with larger grains after approximately 50 nm. Fig. 42 (b) displays a HAADF STEM image of the Cu/TiN-DC stack annealed at 700 °C. The TEM sample was prepared at an area free of hillocks. Image contrast between the different layers is formed because of enhanced electron scattering at heavier atoms. Therefore, going from the Si substrate over the TiN-DC barrier to the Cu metallization, the layers appear progressively brighter. The Cu top layer is thinner than in the pristine case, indicating that a significant amount of Cu has already been consumed to form Cu_3Si, which is corroborated by the SEM (Fig. 39) and XRD (Fig. 40)

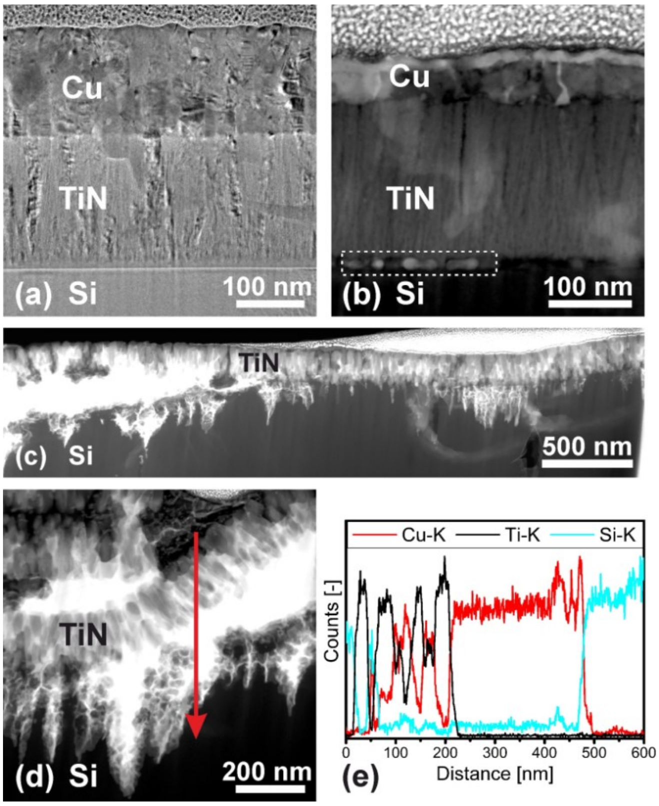

Figure 42: Cross-sectional TEM micrographs of the Cu/TiN-DC stack on Si: (a) bright-field image of the pristine stack, (b) HAADF STEM image of the stack annealed at 700 °C, (c) HAADF STEM overview of the stack annealed at 900 °C, and (d) HAADF STEM detail of the stack annealed at 900 °C with (e) the corresponding qualitative EDX line scan recorded along the arrow.

investigations. Even within the TiN-DC layer, Cu is visible as a bright phase, giving the appearance of a veil over the barrier. A contrast difference is also noticeable within the Cu layer itself. During thinning of the TEM sample in the FIB, a nano-sized pore was exposed at the Cu/TiN-DC interface. Pore walls perpendicular to the plane of the cut are thicker in the resulting sample and therefore now yield brighter thickness contrast in the dark-field image than those parallel to the plane of the cut. Presumably, these pores develop as a "by-product" when the surrounding Cu_3Si hillocks break through the Cu layer, thereby partly lifting it up (Fig. 39). Qualitative EDX mapping (not shown here) reveals the phase visible at the TiN-DC/Si interface (marked by a white rectangle in Fig. 42 (b)) to be composed of Cu and Si. It is plausible that these compounds represent an early stage of the Cu_3Si hillock formation. Fig. 42 (c) shows a STEM overview of the Cu/TiN-DC stack annealed at 900 °C. The TiN-DC layer is bent and begins to disintegrate at the column boundaries. Diffused Cu is visible as the bright phase underneath the original barrier layer. Fig. 42 (d) provides a closer look on the remains of the columnar TiN-DC barrier with a corresponding EDX line profile recorded along the arrow displayed in Fig. 42 (e). The presence of Si on top of and Cu beneath the original TiN-DC barrier is indicative of the terminal barrier failure. Signals in the 50-200 nm region of the profile in Fig. 42 (e) are related alternatingly to Ti and Cu, therefore illustrating that Cu is found preferably along the now wide-open TiN-DC column boundaries. Together with the finding of intergranular porosity in the TEM image of the pristine stack (Fig. 42 (a)), it can be assumed that these boundaries also act as the first fast diffusion paths at lower annealing temperatures. Correlated increases in the Cu and Si EDX signals point towards a Cu-silicide as the reaction product after Cu diffusion through the barrier, which is in good agreement with results discussed in the previous section of this chapter.

TEM investigations of the Cu/$Ti_{0.84}Ta_{0.16}N$-HIP stack are summarized in Fig. 43. The pristine $Ti_{0.84}Ta_{0.16}N$-HIP barrier shown in Fig. 43 (a) grows with a dense columnar structure on the Si/SiO_2 substrate. This growth mode is facilitated by the pulsed irradiation of the growth surface with heavy Ta ions, where momentum transfer leads to atomic intermixing in the near surface region of the developing film [14]. The Cu top layer exhibits larger grains and fewer voids than the Cu film deposited on TiN-DC. No changes are apparent in the bilayer stack after annealing at 700 °C (not shown here), apart from Cu grain growth and the formation of pores at the Cu/barrier interface as an early stage of solid-state de-wetting. The de-wetting of the Cu layer is even more advanced after annealing at 900 °C, leaving parts of the $Ti_{0.84}Ta_{0.16}N$-HIP surface completely bare as visible in the HAADF STEM overview in Fig. 43 (b). This has been interpreted as a sign of high diffusion barrier efficiency [26]. Indeed, the large-scale integrity of the 900 °C diffusion-annealed $Ti_{0.84}Ta_{0.16}N$-HIP film is still observable in Fig. 43 (b). Only upon closer examination of the layer stack, a roughening of the $Ti_{0.84}Ta_{0.16}N$-HIP/Si interface is noticeable (Fig. 43 (c)), indicating initial

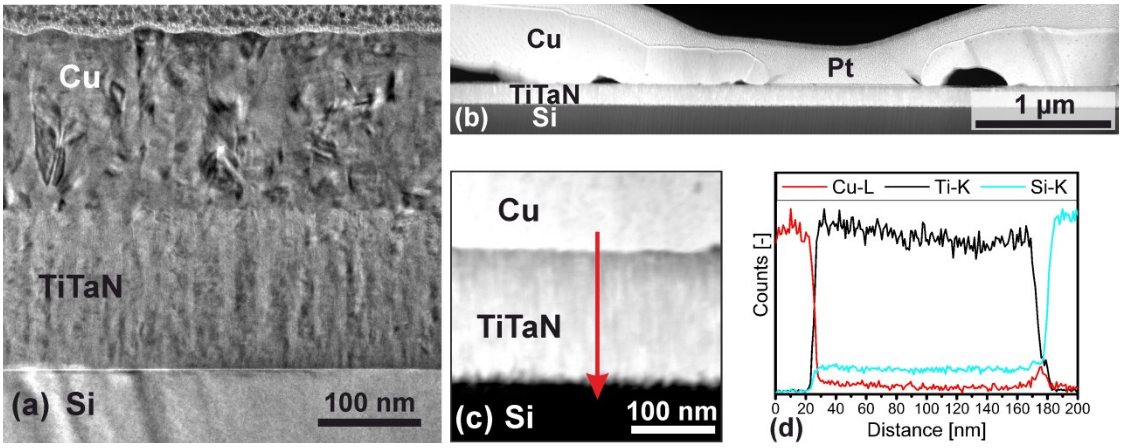

Figure 43: Cross-sectional TEM micrographs of the Cu/$Ti_{0.84}Ta_{0.16}N$-HIP stack on Si: (a) bright-field image of the pristine stack, (b) HAADF STEM overview of the stack annealed at 900 °C, and (c) HAADF STEM detail of the stack annealed at 900 °C with (d) the corresponding qualitative EDX line scan recorded along the arrow.

degradation after the annealing treatment. Apart from that, no interdiffusion zones are evident in the HAADF STEM micrograph as regions of different contrast. Fig. 43 (d) displays the EDX line profile obtained along the arrow in Fig. 43 (c). The Cu/$Ti_{0.84}Ta_{0.16}N$-HIP interface is encountered approximately 25 nm along the profile line. Signals recorded from the Cu-L edge drop rapidly, while signals associated with the Ti-K edge rise accordingly, showing a sharp interface without any indications of interdiffusion. The elevated Si contents measured in the $Ti_{0.84}Ta_{0.16}N$-HIP layer are an artefact arising from the energy overlap of the Si-K and the Ta-M edges. 175 nm along the profiling direction, the $Ti_{0.84}Ta_{0.16}N$-HIP/Si interface is reached. This interface is spread across approximately 20 nm and not as well-defined as the Cu/barrier interface. Additionally, a pronounced Cu spike is apparent at the interface, providing an explanation for the finding of Cu_3Si in XRD patterns of the 900 °C annealed Cu/$Ti_{0.84}Ta_{0.16}N$-HIP stack (Fig. 40) and for the rough appearance of the barrier/substrate interface in Fig. 43 (c). It can be interpreted that the overall amount of Cu diffusing through the $Ti_{0.84}Ta_{0.16}N$-HIP barrier during annealing at 900 °C is so low that it cannot be resolved by EDX inside the barrier, but only at the barrier/substrate interface, where it segregates to eventually form the Cu_3Si compound. Therefore, only minor Cu diffusion can be observed through the dense $Ti_{0.84}Ta_{0.16}N$-HIP barrier annealed at 900 °C, while the TiN-DC barrier already loses its integrity after an annealing treatment at 700 °C, due to pronounced Cu diffusion and the formation of large Cu_3Si hillocks.

6.4 CLOSING REMARKS

This chapter presents a comparison of the performance of a conventional DC magnetron sputtered TiN diffusion barrier (TiN-DC) and a $Ti_{0.84}Ta_{0.16}N$ diffusion barrier deposited by a novel hybrid HIPIMS/DCMS process ($Ti_{0.84}Ta_{0.16}N$-HIP). Both barrier layers are synthesized without external substrate heating in keeping with low-temperature processing restrictions in semiconductor industry. Pristine and 700-900 °C vacuum annealed Cu metallization/barrier/Si substrate stacks are investigated by SEM, XRD, FPP sheet resistivity measurements, and cross-sectional TEM in conjunction with EDX to evaluate diffusion in the stacks. The conventional TiN-DC barrier exhibits major interdiffusion damage already after annealing at 700 °C. Cu_3Si compounds nucleate at the barrier/substrate interface as interdiffusion reaction products and proceed to grow until all available Cu is consumed. This also leads to structural disintegration of the columnar TiN-DC barrier. In contrast, only minor Cu diffusion is evident in the stable $Ti_{0.84}Ta_{0.16}N$-HIP diffusion barrier even after annealing at 900 °C. Small amounts of Cu are found at the barrier/substrate interface, but the $Ti_{0.84}Ta_{0.16}N$-HIP barrier is still largely intact and effective. This improved performance can be attributed to barrier densification by the pulsed bombardment with energetic, heavy Ta ions inherent to the hybrid HIPIMS/DCMS process.

REFERENCES

[1] C. Lee, Y.-L. Kuo, The evolution of diffusion barriers in copper metallization, JOM 59 (2007) 44–49.

[2] M.-A. Nicolet, Diffusion barriers in thin films, Thin Solid Films 52 (1978) 415–443.

[3] Y.M. Zhou, M.Z. He, Z. Xie, Diffusion barrier performance of novel Ti/TaN double layers for Cu metallization, Appl. Surf. Sci. 315 (2014) 353–359.

[4] Y. Meng, Z.X. Song, J.H. Chen, F. Ma, Y.H. Li, J.F. Wang, C.C. Wang, K.W. Xu, Ultrathin ZrB_xO_y films as diffusion barriers in Cu interconnects, Vacuum 119 (2015) 1–6.

[5] W. Martienssen, H. Warlimont, eds., Springer Handbook of Condensed Matter and Materials Data, Springer Berlin Heidelberg, 2005.

[6] S.P. Murarka, Diffusion barriers in semiconductor devices/circuits, in: D. Gupta (Ed.), Diffusion Processes in Advanced Technological Materials, 1st ed., William Andrew Publishing, Norwich, NY, 2005: pp. 239–281.

[7] J.-E. Sundgren, B.-O. Johansson, S.-E. Karlsson, H.T.G. Hentzell, Mechanisms of reactive sputtering of titanium nitride and titanium carbide II: Morphology and structure, Thin Solid Films 105 (1983) 367–384.

[8] A.E. Kaloyeros, E. Eisenbraun, Ultrathin diffusion barriers/liners for gigascale copper metallization, Annu. Rev. Mater. Sci. 30 (2000) 363–385.

[9] M. Mändl, H. Hoffmann, P. Kücher, Diffusion barrier properties of Ti/TiN investigated by transmission electron microscopy, J. Appl. Phys. 68 (1990) 2127–2132.

[10] W. Sinke, G.P.A. Frijlink, F.W. Saris, Oxygen in titanium nitride diffusion barriers, Appl. Phys. Lett. 47 (1985) 471–473.

[11] J.O. Olowolafe, J. Li, J.W. Mayer, E.G. Colgan, Effects of oxygen in TiN_x on the diffusion of Cu in Cu/TiN/Al and Cu/TiN_x/Si structures, Appl. Phys. Lett. 58 (1991) 469–471.

[12] K.T. Nam, A. Datta, S.-H. Kim, K.-B. Kim, Improved diffusion barrier by stuffing the grain boundaries of TiN with a thin Al interlayer for Cu metallization, Appl. Phys. Lett. 79 (2001) 2549–2551.

[13] M. Mühlbacher, A.S. Bochkarev, F. Mendez-Martin, B. Sartory, L. Chitu, M.N. Popov, P. Puschnig, J. Spitaler, H. Ding, N. Schalk, J. Lu, L. Hultman, C. Mitterer, Cu diffusion in single-crystal and polycrystalline TiN barrier layers: A high-resolution experimental study supported by first-principles calculations, J. Appl. Phys. 118 (2015) 085307.

[14] G. Greczynski, J. Lu, S. Bolz, W. Kölker, C. Schiffers, O. Lemmer, I. Petrov, J.E. Greene, L. Hultman, Novel strategy for low-temperature, high-rate growth of dense, hard, and stress-free refractory ceramic thin films, J. Vac. Sci. Technol. A 32 (2014) 0415151–04151512.

[15] G. Abadias, L.E. Koutsokeras, S.N. Dub, G.N. Tolmachova, A. Debelle, T. Sauvage, P. Villechaise, Reactive magnetron cosputtering of hard and conductive ternary nitride thin films: Ti–Zr–N and Ti–Ta–N, J. Vac. Sci. Technol. A 28 (2010) 541.

[16] E.M. Zielinski, R.P. Vinci, J.C. Bravman, Effects of barrier layer and annealing on abnormal grain growth in copper thin films, J. Appl. Phys. 76 (1994) 4516.

[17] C.V. Thompson, Solid-state dewetting of thin films, Annu. Rev. Mater. Res. 42 (2012) 399–434.

[18] International Centre for Diffraction Data, Powder Diffraction File 00-004-0836, 2007.

[19] International Centre for Diffraction Data, Powder Diffraction File 00-038-1420, 2007.

[20] International Centre for Diffraction Data, Powder Diffraction File 00-051-0916, 2007.

[21] S.H. Hsieh, C.M. Chien, W.L. Liu, W.J. Chen, Failure behavior of ITO diffusion barrier between electroplating Cu and Si substrate annealed in a low vacuum, Appl. Surf. Sci. 255 (2009) 7357–7360.

[22] A.A. Istratov, E.R. Weber, Physics of copper in silicon, J. Electrochem. Soc. 149 (2002) G21.

[23] International Centre for Diffraction Data, Powder Diffraction File 00-049-1283, 2007.

[24] P. Majumder, C.G. Takoudis, Investigation on the diffusion barrier properties of sputtered Mo/W–N thin films in Cu interconnects, Appl. Phys. Lett. 91 (2007) 162108.

[25] I. Petrov, P.B. Barna, L. Hultman, J.E. Greene, Microstructural evolution during film growth, J. Vac. Sci. Technol. A 21 (2003) S117.

[26] J. Yu, J. Bian, L. Jiang, Y. Qiu, W. Duan, F. Meng, Z. Liu, Tungsten-doped indium oxide thin film as an effective high-temperature copper diffusion barrier, ECS Solid State Lett. 3 (2014) N15–N17.

CHAPTER 7

CONCLUSIONS AND OUTLOOK

7. CONCLUSIONS AND OUTLOOK

Within this thesis, interdiffusion characteristics in the technologically important TiN/Cu and TiTaN/Cu thin film systems have been investigated. Special emphasis is placed on the two high resolution characterization methods TEM and APT. In a nutshell, results presented in chapters 3-6 lead to two main conclusions: Firstly, the microstructure of diffusion barrier layers is a decisive factor determining the barrier efficiency and in extension the lifetime and reliability of microelectronic devices. Single-crystal TiN layers would be an ideal candidate for high-performance diffusion barriers due to their nearly defect-free film structure. However, it is not yet feasible to fabricate such single-crystal barrier layers on an industrial level, because of limitations in processing temperature and substrate materials. An alternative is to manipulate the microstructure of well-established polycrystalline TiN diffusion barriers to enhance their efficiency. This can be achieved by limiting the fraction of open, porous grain boundaries within the columnar film. Suitable deposition parameters include high substrate temperatures and moderate bias voltages to provide the necessary ad-atom mobility without damaging the growing film. Investigations of TiTaN films deposited by the hybrid high-power impulse/DC magnetron sputtering process recently developed by Greczynski *et al.* [1] show that a low-temperature deposition process meeting the needs of microchip manufacturers can be utilized to produce dense, reliable nitride barriers as well. In this case, barrier densification is accomplished by the pulsed bombardment of the film growth surface with only a few at.% of energetic, heavy Ta ions.

First-principles calculations also suggest the possibility of controlling atomic diffusion mechanisms of Cu in TiN by tuning the TiN stoichiometry, although the large-scale technological execution of this idea might turn out to be challenging. Moreover, this approach is only feasible if preferential diffusion paths such as grain boundaries or triple junctions in the film are eliminated.

From a characterization aspect, this thesis demonstrates that the still relatively new APT technique can be used to successfully visualize diffusion processes in TiN/Cu thin film stacks. The technique's strength lies in providing chemical identification on the atomic level, while only limited structural information can be gained. Therefore, the correlation of APT with a more versatile microscopy technique such as (HR)TEM is beneficial. The combination of the two methods allows not only for the comprehensive characterization of TiN/Cu bilayers, but can also be used to monitor the agreement between electron micrographs of the investigated thin films and the three-dimensional reconstruction of the APT specimen tips. Particularly when analyzing interfaces by APT, the limitations of the reconstruction algorithm related to sudden changes in the evaporation fields of layered material systems have to be considered.

The “ultimate” microscopy technique would be a hybrid TEM/APT system, able to determine the position, identity, and chemical nature of every atom in a material volume [2]. First steps in this direction are currently being made by imaging APT tips before and after evaporation in a TEM instead of preparing separate samples for both instruments. However, the fact that state-of-the-art APTs and TEMs are still seldom available in the same laboratory and very delicate sample handling is obligatory when transferring the specimens from one system to the other, makes this approach time- and cost-intensive. Once the technique is more refined and advanced and a close link to numerical models and simulations is established, it might well be the solution to the metrology needs projected by the *International Technology Roadmap for Semiconductors,* as outlined in the introductory chapter of this thesis.

References

[1] G. Greczynski, J. Lu, S. Bolz, W. Kölker, C. Schiffers, O. Lemmer, I. Petrov, J.E. Greene, L. Hultman, Novel strategy for low-temperature, high-rate growth of dense, hard, and stress-free refractory ceramic thin films, J. Vac. Sci. Technol. A 32 (2014) 0415151–04151512.

[2] T.F. Kelly, M.K. Miller, K. Rajan, S.P. Ringer, Atomic-scale tomography: A 2020 vision, Microsc. Microanal. 19 (2013) 652–664.

RELATED PUBLICATIONS

List of publications related to this thesis:

Paper I. **Copper diffusion into single-crystalline TiN studied by transmission electron microscopy and atom probe tomography.**
M. Mühlbacher, F. Mendez-Martin, B. Sartory, N. Schalk, J. Keckes, J. Lu, L. Hultman, and C. Mitterer.
Thin Solid Films ***574*** *(2015) 103–109.*

Paper II. **Cu diffusion in single-crystal and polycrystalline TiN barrier layers: A high-resolution experimental study supported by first-principles calculations.**
M. Mühlbacher, A. S. Bochkarev, F. Mendez-Martin, B. Sartory, L. Chitu, M. N. Popov, P. Puschnig, J. Spitaler, H. Ding, N. Schalk, J. Lu, L. Hultman, and C. Mitterer.
J. Appl. Phys. ***118*** *(2015) 085307.*

Paper III. **TiN diffusion barrier failure by the formation of Cu_3Si investigated by electron microscopy and atom probe tomography.**
M. Mühlbacher, G. Greczynski, B. Sartory, F. Mendez-Martin, N. Schalk, J. Lu, L. Hultman, and C. Mitterer.
Submitted for publication.

Paper IV. **Improvement of low-temperature sputter-deposited TiN diffusion barriers by bombardment with Ta ions.**
M. Mühlbacher, G. Greczynski, B. Sartory, N. Schalk, J. Lu, I. Petrov, J. Greene, L. Hultman, and C. Mitterer.
Manuscript in final preparation.

Author's contributions (supervision not included):

Paper I: I planned and performed the depositions and annealing treatments, carried out the APT and TEM investigations, and evaluated and interpreted all the data. I wrote the manuscript.

Paper II: I planned and performed the depositions and annealing treatments, carried out the XRD, APT, and TEM investigations, and evaluated and interpreted all the data. With the exception of the theoretical sections (section IV and parts of section II), I wrote the manuscript.

Paper III: I took part in planning the depositions, performed the annealing treatments, carried out the four-point-probe sheet resistivity measurements, XRD, and APT investigations, and participated in the SEM and EDX investigations. Furthermore, I evaluated and interpreted all the data and wrote the manuscript.

Paper IV: I took part in planning the depositions, performed the annealing treatments, carried out the four-point-probe sheet resistivity measurements, XRD, and TEM investigations and evaluated and interpreted all the data. I wrote the manuscript.

	Conception and planning	**Experiments**	**Analysis and interpretation**	**Manuscript preparation**
Paper I	100%	100%	100%	100%
Paper II	75%	75%	75%	75%
Paper III	80%	80%	100%	100%
Paper IV	50%	80%	100%	100%

Other publications by the author:

- **Functional thin films for display and microelectronics applications.**
  C. Mitterer, T. Jörg, R. Franz, M. Mühlbacher, B. Sartory, F. Mendez-Martin, and N. Schalk.
  BHM Berg- und Hüttenmännische Monatshefte ***160*** *(2015) 231–234.*

- **Influence of Fe impurities on structure and properties of arc-evaporated AlCrN coatings.**
  M. Mühlbacher, R. Franz, J. Paulitsch, H. Rudigier, P. Polcik, P.H. Mayrhofer, and C. Mitterer.
  Surf. Coat. Technol. ***215*** *(2013) 96–103.*

- **TiO_2(100)/Al_2O_3(0001) interface: A first-principles study supported by experiment.**
  M.N. Popov, J. Spitaler, M. Mühlbacher, C. Walter, J. Keckes, C. Mitterer, and C. Draxl.
  Phys. Rev. B ***86*** *(2012) 205309.*